EFFECTS OF AEROSOLS ON MICROPHYSICS AND ON URBAN WARM SEASON PRECIPITATION

by

Nathan Hosannah

A dissertation submitted to the Graduate Faculty in Mechanical Engineering in partial fulfillment of the requirements for the degree of Doctor of Philosophy, The City University of New York

2013

This manuscript has been read and accepted for the Graduate Faculty in Engineering in satisfaction of the dissertation requirement for the degree of Doctor of Philosophy.

Adviser [typed name] Professor Jorge González

[**required signature**]

Executive Officer [typed name] Dean Ardie Walser

[**required signature**]

[typed name] Professor Yiannis Andreopoulos

[typed name] Professor Robert Bornstein

[typed name] Professor Barry Gross

[typed name] Dr. Daniel Comarazamy

THE CITY UNIVERSITY OF NEW YORK

ABSTRACT

EFFECTS OF AEROSOLS ON MICROPHYSICS AND ON URBAN WARM SEASON PRECIPITATION

by

Nathan Hosannah

Adviser: Professor Jorge Gonzalez

Precipitation anomalies in and around major urban centers have been attributed to dynamic processes such as warm air updrafts induced by urban heat island events and to microphysical processes affected by the release of natural and anthropogenic aerosols that affect atmospheric water balance. Both factors must be analyzed in order to fully understand the role that urban environments may have on precipitation. The research presented here is directed towards improving understanding of how aerosol particle size distribution (PSD) and land cover land use (LCLU) affect cloud processes and precipitation over a complex urban environment such as New York City (NYC). While aerosols are intrinsically necessary for rainfall formation, and urban environments also influence precipitation via convection enhancement, the partial contributions of each are not yet known. The Regional Atmospheric Modeling System (RAMS) was used to simulate several NYC summer precipitation scenarios. PSD data from NASA's Aerosol Robotic Network (AERONET) complemented with National Land Cover Database (NLCD) 2006 land surface data for NYC and northern New Jersey (NJ) were processed and assimilated directly into RAMS to determine the effect of varying PSD and LCLU on simulated precipitation amounts. An ensemble of 17 numerical simulations were configured and run. The first two runs were month long runs for July 2007, the first with constant PSD values, and the second with PSD updates. The third and fourth runs mirrored the first two simulations for a "No-

City" case. A fifth month long simulation was run with average Cloud Condensation Nuclei (CCN) and Giant CCN values. Next, twelve 24 hour simulations driven with high volumes of fine mode particles and with high volumes of coarse mode particles each under "City" and "No City" conditions were compared for 1-day localized and mesoscale events. Results suggest that RAMS precipitation results are sensitive to both PSD variation and land use variations.

Acknowledgments

I want to thank my mother and father, Waveney Gouveia and Vibert Hosannah for creating me and giving me the ability to grow on this plane of existence. I also thank my mother for making me a question asking, investigating individual. I want to thank my brothers Lawrence and Aaron for always managing to increase my imaginative ability, and my brother Devon for making sure that I would always keep striving to pervade through, around, and over any obstacle set in my path. Thanks to Auntie Bernadette and Calvin for providing an undergraduate home. Uncle Acmar, you made me want to be an engineer! Thanks to my cousins Andre, Danon, and Sharif for their support, laughter, and confidence in my abilities during the most difficult portions of my scholastic career. To my nieces Caroline and Mahalia, nephews Aaron and Aiden, aunts, uncles and other family, thank you.

Dr. Brathwaite, thank you for providing the resources necessary for me to put off getting a job while creating a career for myself. Hahaha! To the LSAMP office, I send a special THANK YOU. To Professors Charles Watkins and Latif Jiji, you helped align my academic path. Without your guidance it would have been more difficult to get to my current point. To my brothers in arms, Richard Able and Rodley Ferguson: You both provided nourishment that kept me well rounded in a square room. Padene, every thought is a guide towards possibility. This I know.

I'd also like to thank Jorge Gonzalez, Barry Gross, Yiannis Andreopoulos, Bob Bornstein, Bereket Lebassi, Daniel Comarazamy, Steve Prinzivalli from Weatherbug, Larry Oolman from the University of Wyoming, NOAA CREST, ISET, and CCNY for providing the resources to make this research possible.

Table of Contents

List of Figures

List of Tables

Nomenclature

a	Droplet curvature parameter (cm)
b	Droplet solute parameter (cm^3)
c_p	Constant pressure specific heat ($J\ kg^{-1}K^{-1}$)
ε	Gas constant ratio
g	Gravitational acceleration ($m\ s^{-2}$)
K	Coefficient of thermal conductivity ($J\ m^{-1}\ s^{-1}\ K^{-1}$)
$k_{1,2,3}$	Constant in terminal velocity equation ($cm^{-1}\ s^{-1}$, $cm^{.5}\ s^{-1}$, s^{-1})
L	Latent Heat ($J\ kg^{-1}$)
M	Cloud water content ($kg\ m^{-3}$)
M_s	Molecular weight of solution constituent (kg)
m_s	Weight of the salt (kg)
η	Fine mode fraction
N_t	Total number of CCN particles
Q	Heat flux ($W\ m^{-2}$)
R	Ideal gas constant ($J\ mol^{-1}\ K^{-1}$)
R_t	Radius of larger droplet (m)
R_v	Water vapor gas constant ($J\ kg^{-1}K^{-1}$)
R_s	Solar radiation (m)
r_r	Mixing ratio
r_t	Radius of small droplet
T_o	Initial temperature (^oC)
T_∞	Ambient temperature (^oC)

T_t Drop temperature (^oC)

τ Time constant (s)

τ_a Aerosol optical depth

ρ_l Water density (kg m^{-3})

ρ_v Vapor density (kg m^{-3})

θ Potential Temperature (^oC)

σ albedo

x_o Impact parameter (m)

u velocity in the x dimension (m s^{-1})

v velocity in the y dimension (m s^{-1})

w velocity in the z dimension (m s^{-1})

Π Exner function

Acronyms

ACT	Waco, Texas
AERONET	Aerosol Robotic Network
AMO	Atlantic Multi-Decadal Oscillation
AOT	Aerosol Optical Thickness
ATL	Atlanta, Georgia
BATS	Biosphere Atmosphere Transfer System
BB	Bound Brook, New Jersey
CALIOP	Cloud Aerosol LIDAR and Orthogonal Polarization
CALIPSO	Cloud-Aerosol Lidar and Infrared Pathfinder Satellite Observation Satellite
CAPE	Convective Available Potential Energy
CB	Canoe Brook, New Jersey
CBH	Cloud Base Height
CCN	Cloud Condensation Nuclei
CCNY	City College of New York
CDC	Cloud Droplet Concentration
COD	Cloud Optical Depth
CP	Central Park, New York
CR	Cannistear Reservoir, New Jersey
DFW	Dallas, Texas
EF	Essex Fells, New Jersey
EWR	Newark Airport, New Jersey
GCCN	Giant Cloud Condensation Nuclei
GOES	Geostationary Operational Environmental Satellites
HN	Harrison, New Jersey

HVCM	High Volume Coarse Mode
HVFM	High Volume Fine Mode
IPCC	Intergovernmental Panel on Climate Change
JFK	John F. Kennedy Airport, New York
LCLU	Land Cover Land Use
LEAF-3	Land Ecosystem Atmosphere Feedback
LGA	LaGuardia Airport, New York
LIDAR	Light Detection and Radar
LWC	Liquid Water Content
LWMR	Liquid Water Mixing Ratio
NCEP	National Center for Environmental Prediction
MCC	Mesoscale Convective Complex
MGM	Montgomery, Alabama
MM5	Fifth Generation Pennsylvania State University NCAR Mesoscale Model
MN	Mineola, New York
NB	New Brunswick, New Jersey
NESDIS	National Environmental Satellite and Information Service
NLCD	National Land Cover Database
NJ	New Jersey
NM	New Milford, New Jersey
NWS	National Weather Service
NYC	New York City
OS	Oceanside, New York
PF	Plainfield, New Jersey
PSD	Particle Size Distribution

RAMS	Regional Atmospheric Modeling System
RMSE	Root Mean Square Error
SAT	San Antonio, Texas
SEC	Secaucus, New Jersey
TKE	Turbulent Kinetic Energy
UHI	Urban Heat Island
WT	Wantaugh, New York
WRF	Weather Research and Forecasting Model

Chapter 1

Introduction

Cities are complex systems where much research is still required to fully comprehend how the interplay between atmospheric dynamics, urban landscapes, and cloud microphysical processes impact precipitation. The Inter-governmental Panel of Climate Change (IPCC) suggests that extreme weather events will occur with higher frequency in cities in the near future due to warming climates (Parry et al. 2008). When combined with rising sea levels and population increases, coastal cities are vulnerable to flooding, increased loss of human life, and property damage. To better serve society, a need exists to improve understanding of variables affecting precipitation in coastal urban environments.

Many studies present clear evidence that cities influence regional weather via modification of synoptic fronts, generation of the urban heat island (UHI, shown in Fig. 1) which occurs when higher temperatures exist over an urban area than its rural surroundings (Bornstein 1968), surface-atmosphere interactions that impact surface heat and moisture fluxes (Huff and Changnon 1973; Dixon and Mote 2003), building barrier effects (Bornstein and LeRoy 1990) which can influence storm splitting and bifurcation (Fig. 2), and increased aerosol concentrations (Carrio et al. 2010).

According to Shepherd et al. (2002), UHIs have implications for local and regional environments, including increased energy demands for cooling, adjustment of local wind flows due to non uniform thermal state, air quality deterioration, and modifications to the precipitation cycle. It has been reported that the annual mean air temperature of a city with 1 million people or more can be 1–3°C warmer than its surroundings, and higher temperatures in summer increase

energy demand for cooling (Akbari 2005). Additional heat provided by the UHI leads to greater upward air motion, which can induce convective rainfall and thunderstorm activity.

During non-UHI periods, building-barrier induced difluence may occur. The upwind urban edge divides regional flows as they approach a city (Bornstein and LeRoy 1990). Difluence produces cyclonic turning over the left-hand urban edge (looking downstream) and anticyclonic turning over the right-hand urban edge. Barriers also produce confluence at both lateral urban edges, where air deflected around the city converges with the undisturbed prevailing flow, and downwind of the city where the flow re-unites.

To fully understand the nature of cloud processes and precipitation in urban environments it is important that the role of aerosols also be considered. Aerosols near the surface can be transported into the atmosphere via the UHI, enabling them to act as cloud condensation nuclei (CCN) and/or giant cloud condensation nuclei (GCCN). As an air parcel rises, vapor adheres onto CCN/GCCN, leading to the formation of droplets. The current work lends support to the argument that ingestion of aerosol particle size distribution (PSD) data in numerical models is important in climate modeling and weather prediction, and that its study can lead to advancements in the use of data from updated algorithms that run satellite weather instruments, LIDAR, and other remote sensing technology.

Aerosols can be comprised of smoke particles, dust, sea salt, and sulfates. Some may be created by natural processes, such as volcanic eruptions, dust storms, forest and grassland fires, living vegetation, and sea spray. Burning of fossil fuels and the alteration of natural land cover also generate anthropogenic aerosols. Aerosols can affect the climate both directly (through the absorption and scattering of solar and terrestrial radiation) and indirectly (by modification of

cloud properties associated with cloud radiative feedback effects), each process thereby either warms or cools the planet.

The amount of scattering and absorption of solar and terrestrial radiation depends on aerosol physical and chemical characteristics. Aerosols created by anthropogenic activities currently account for about 10% of atmospheric aerosols. Those with hygroscopic properties can act as cloud condensation nuclei/giant cloud condensation nuclei (CCN/GCCN), key sources for cloud droplet and rain development (Feingold 1999; Rosenfeld et al., 2008). Most aerosols are concentrated in the Northern Hemisphere, downwind of: industrial sites, slash-and burn agricultural regions, and overgrazed grasslands (Przyborski and Ranson 2009). They can change the frequency of cloud occurrence, cloud thickness, and rainfall amounts. With remote sensors, researchers can quantify aerosols amounts within a cloud column, but have not yet been able to determine aerosol compositions in clouds.

Microphysical processes (i.e., condensation, evaporation, collision and coalescence, and droplet break-up) take place on the scale of either CCN/GCCN and/or precipitation drops. These processes lead to the formation of rain and other types of solid precipitation, including hail, graupel, and snow. In both warm and cold rain production, droplets and ice particles, respectively, collide and coalesce over time. Some grow larger than others, and start to slowly fall, accelerating as they accumulate more and more droplets. If cloud droplets grow larger than 0.1 mm in diameter through this process, they gain enough momentum to overcome typical cloud updrafts and fall through the air below the cloud, where despite evaporation, they reach the ground as precipitation.

Of importance in the formation of heavier rain in cold clouds is the Bergeron process, which involves frozen particles. Although cloud level temperature is often below 0^{o}C, droplets

can remain in a ‘super cooled’ liquid form in the absence of freezing nuclei. In these circumstances, a small disturbance (e.g., collision with other super cooled droplets) is enough to cause them to suddenly freeze solid. As water vapor condenses onto ice particles more easily than onto liquid water droplets, these ice particles grow faster than the surrounding droplets and begin to fall sooner. They then grow further via accumulation of other droplets, and quickly become large enough to overcome cloud updrafts.

Since the ice particles encounter ever warmer layers of the atmosphere as they fall, they often melt and reach the ground as rain. If they have formed in a thick cloud however, they can become so large that they do not melt before they reach the ground, and thus they fall as granulated ice particles. Storm clouds can contain updrafts so strong that ice particles that have already melted near the surface are pulled back up into the cloud and refreeze. When they fall again, they grow more by the accumulation of other droplets, and melting again. This process can be repeated a number of times, leading to the formation of large, layered hailstones.

Cloud water budgets at small and large scales can be affected by varying CCN/GCCN concentration and PSDs, at a given constant liquid water content (LWC). The properties of clean (aerosol concentrations below 10^2 cm^{-3}) and polluted (above 10^2 cm^{-3}) clouds are displayed in Figs.3a and 3b. These figures show that as aerosol concentration increases, the amount of water available for condensation is spread over more particles, resulting in smaller water droplets. Smaller droplets in higher concentration increase cloud albedo, rates of evaporation, and absorption while precipitation is reduced. For cleaner clouds, there will be more large droplets, reduced evaporation, albedo, and rates of evaporation with enhanced precipitation.

The goal of the present research is thus to gain insights about the role of PSD variation on precipitation and cloud microphysics in urban environments and how it influences cloud physics,

precipitation patterns, rates, and accumulation totals over and near an urban area. Analysis of precipitation caused by microphysics alone in urban environments is difficult, because it is coupled to other contributions (e.g., effects of land cover and atmospheric dynamics). A better understanding of cloud microphysics may aid in the forecasting of localized precipitation events.

Although the focus herein is on the coastal urban area encompassing NYC, understanding how PSD variation affects precipitation in a city is beneficial and applicable across the country and perhaps the planet, as inland continental cities can have similar PSDs to those found in coastal urban environments (although composition may vary). Ingestion of bimodal PSD, as opposed to the normally used unimodal PSD, in atmospheric mesoscale models for complex urban regions such as NYC region is new ground in climate and weather prediction. To investigate the problem further, an in depth literature review follows in Chapter 2. Methodology will be discussed in Chapter 3, results in Chapter 4, and conclusions in Chapter 5.

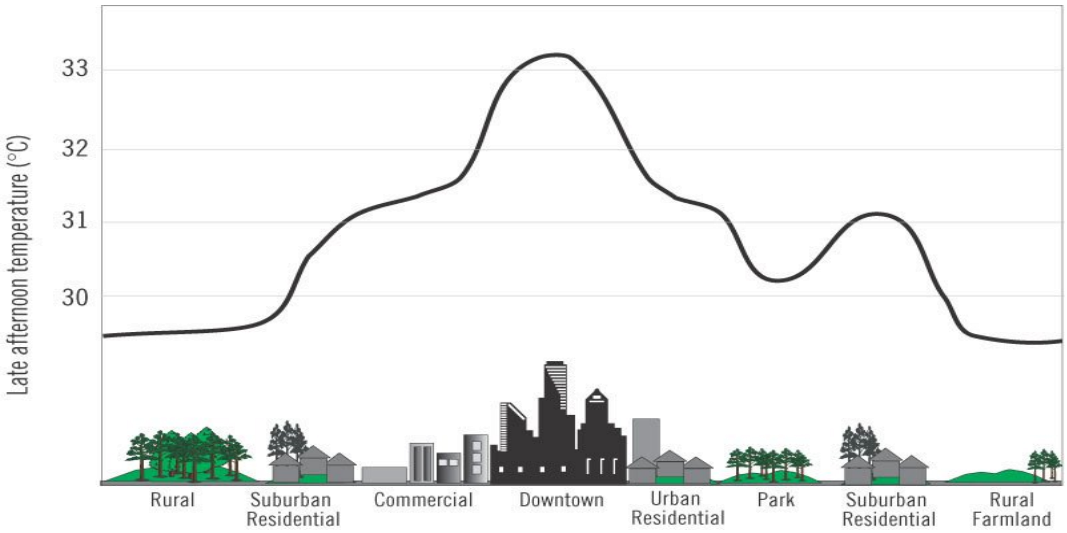

Fig. 1: Idealized urban heat island structure. Source: http://rsd.gsfc.nasa.gov

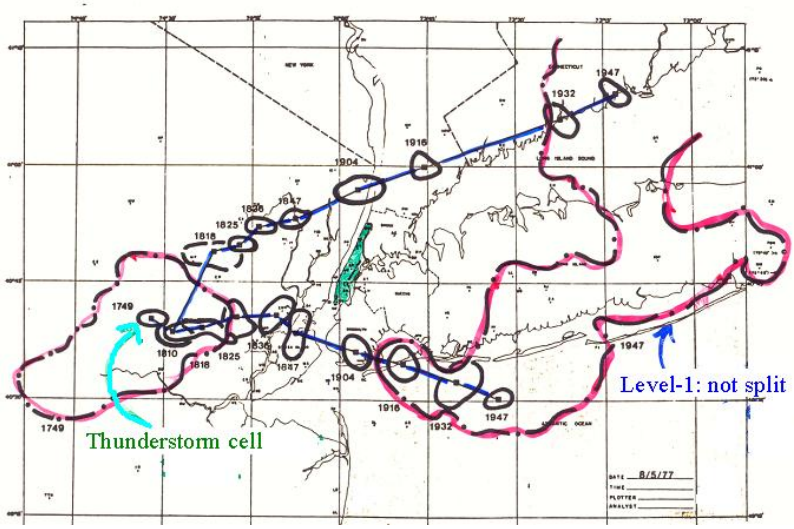

Fig. 2: Level 1 and 3 radar echoes for 5 August 1977 over NYC for a thunderstorm cell. Level 3 echoes show evidence of storm splitting while Level 1 echoes do not split.

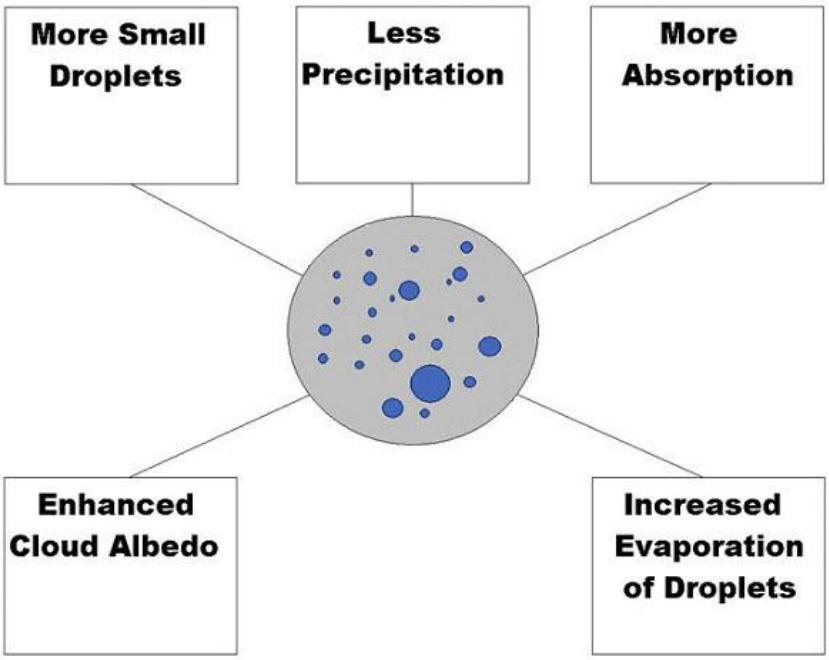

Fig. 3a: Properties of a polluted cloud

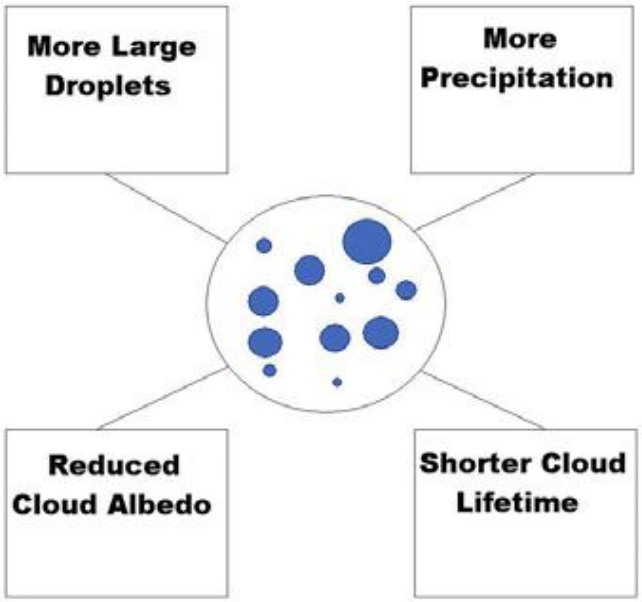

Fig. 3b: Properties of a clean cloud.

Chapter 2

Literature Review

2.1 Atmospheric Dynamics

2.1.1 Observational Studies on Atmospheric Dynamics

Climatological 100 years for the rapidly urbanizing Indian landscape shows precipitation increases in several urban locations (>70 mm/day) during the summer monsoon season (Sinha Ray and Srivastava 2000). The increase in extreme rainfall (>120 mm/day) events during the Indian monsoon has been more profound in the last 50 years (Goswami et al. 2006; Kishwatal et al. 2010) coincident with population increases and land cover land use (LCLU) changes. Analysis of the historical precipitation record of Phoenix, Arizona revealed that on active monsoon days, the low-middle tropospheric flow is southeasterly and that locations in the northeastern suburbs and exurbs of the Phoenix metropolitan area have experienced statistically significant increases in mean precipitation of 12–14% during the monsoon season from a pre-urban (1895–1949) to post-urban (1950–2003) period (Shepherd 2006). Selover (1997) showed that moving summer convective storms over Phoenix, Arizona produce a precipitation minimum over the city in conjunction with surrounding lateral and downwind maximum values.

Evidence that anthropogenic activities, e.g., urbanization, can significantly alter precipitation processes is mounting. Over the past 30 years, warm-season rainfall increases of 17% over and downwind of major urban cities have been discovered, with weekday precipitation generally more plentiful than weekend precipitation in St. Louis, Cleveland, and Chicago (Huff and Changnon 1973). This is believed to be due to greater weekday production of industrial

pollutants which act as CCN (Parry et al. 2008). Data from the Tropical Rainfall Measuring Mission (TRMM) satellite precipitation radar were employed to identify warm-season rainfall patterns around Atlanta, Montgomery, Alabama; Nashville, Tennessee; San Antonio, Waco, and Dallas from 1998-2000 (Shepherd et al. 2002). Using a 15 month analysis of mean rainfall rates, researchers found precipitation increases of up to 51% in these locations over their rural surrounding areas. The 5 cities that experienced significant urban-impacted rainfall (shaded cross region) in warm-season months include Atlanta (ATL), Montgomery (MGM), Dallas (DFW), Waco (ACT), and San Antonio (SAT). Figure 4 shows the locations of the rainfall in relation to the city. The arrows represent the mean prevailing wind direction.

Analysis of Mexico City's historical records showed that the frequency of intense rain showers has increased in recent decades in correlation with its population growth (Jauregui and Romales 1996). Investigation in Ankara, Turkey showed that the urban influence on heavy showers is strongest in June. The METROMEX project showed that the number of days with showers in the summer months increases by 45% due to urban effects. Showers are concentrated at the center and downwind of cities (Kessler 1994). Similar results have been found for convective storms over Phoenix (Diem and Brown 2003). Enhanced lightning activity over and downwind of Houston has been detected. Lightning is evidence of enhanced convection in the atmosphere (due to charged aerosols), and thunderstorm activity is intensified with its presence (Shepherd and Burian 2003).

Researchers have also analyzed the patterns of cloud-to-ground (CG) lightning flashes around Atlanta, a region that has undergone an intense conversion from natural to anthropogenic land uses. For the time period between 1992 and 2003, annual average CG flash density values 50 to 75% higher than in the surrounding rural areas were observed (Dixon and Mote 2003).

Temperature records suggest that Riyadh, Saudi Arabia has experienced an adjustment in mean temperature in response to the alteration of urban surfaces. Precipitation records also indicate an upward trend in mean and total precipitation in and around Riyadh in the last 10–15 years, but it is difficult to attribute the increase to urbanization, since other less urbanized stations in Saudi Arabia also exhibit a similar increase (Shepherd 2006). A possible cause of these shifts is global climate change.

Ground and satellite observations provide large amounts of information about climate and the effects of aerosols on weather. A number of passive satellite instruments have been used to develop global climatologies of terrestrial tropospheric aerosols by analysis of the properties of sunlight reflected by the atmosphere–surface system. These efforts have produced several climatologies which represent the same aerosol characteristics, such as aerosol optical thickness (AOT) and size.

Stegmann (2004) used a data set of AOT and Angstrom exponent to study regional variability of aerosol properties in the North Atlantic basin. Results show seasonal dynamics in both aerosol activity and in aerosol size structure. All sites adjacent to the US east coast exhibited high Angstrom values, owing to the strong influence of a variety of small-sized urban aerosols. Large particles with low Angstrom exponents are associated with higher aerosol load while smaller particles with high Angstrom exponents generally correspond to lower AOT levels. High-resolution and high-quality MODIS aerosol and TRMM precipitation datasets have been used to investigate the observed inverse relationship between aerosol and precipitation in West Africa (Huang et al. 2009), where precipitation was reduced for high aerosol concentrations of dust and smoke for convective, stratiform, and shallow precipitation types.

Baumer (2007) revealed that the weekly cycle of anthropogenic gaseous and particulate emissions leads to weekly AOT patterns. Since these patterns are derived from the reduction of direct sun radiation by columnar atmospheric aerosol, these results represent strong evidence for an anthropogenic direct aerosol effect on shortwave radiation. Large concentrations of aerosols have been reported to both decrease and increase rainfall as a result of their radiative properties and CCN activities (Mischenko 2007).

Climatological studies, unless segmented by wind direction can produce confusing results, as "downwind" depends on wind direction. Locations of precipitation minimums and maximums dependent on wind direction can provide important information about the role of the urban environment on precipitation. Case studies investigating urban weather dynamics can provide more information about the initiation, development, and completion of land based and atmospheric phenomena.

Bornstein (1968) investigated UHI effects in NYC by analyzing differences in temperature fields for 42 mornings between July 1964 and December 1966. Results show urban surface temperature inversions to be less intense and frequent than those in surrounding non-urban regions. The average UHI intensity was maximum at the surface, and zero at 300 m. On mornings with strong urban inversion layers, the UHI extended to 500 m.

Research on urban barrier effects Bornstein and LeRoy (1990) on a storm approaching NYC shows evidence of storm spitting. Level 1 and 3 radar echoes over the NYC region (Fig. 2) show that level 3 radar echoes, which represent precipitated water, split and travel around the city, while the level 1 echoes, which represent water vapor, do not split.

2.1.2 Modeling Studies on Atmospheric Dynamics

Niyogi et al. (2011) examined 91 unique summertime (May 2000–August 2009) thunderstorm cases over the Indianapolis, Indiana, urban area and found that urban regions altered the intensity and composition/structure of approaching thunderstorms because of land surface heterogeneity. Over 60% of storms changed structure over the Indianapolis area compared with only 25% over rural areas. Study results show that the urban area has a strong climatological influence on regional thunderstorms. In addition to the climatological study, researchers also investigated a typical storm on 13 June 2005 using available observations and the fifth-generation Pennsylvania State University–NCAR Mesoscale Model (MM5), version 3.7.2. Two simulations were performed with and without the urban LCLU/Indianapolis region. Removing the Indianapolis urban region caused distinct differences in the regional convergence and convection as well as in simulated base reflectivity, surface energy balance, and boundary layer structure.

The UHI effect on precipitation has been investigated using numerical climate models. Baik et al. (2000) showed that the time required for the first cloud water (or rainwater) formation decreases and its horizontal location is closer to the heating center of the city as UHI intensity increases. For the same basic-state wind speed and heat island intensity, a stronger downwind updraft is needed to trigger moist convection in less favorable basic-state thermodynamic conditions. Aside from the effect on temperature, UHIs can produce secondary effects on local meteorology, including alteration of local wind patterns, development of clouds and fog, humidity, and rates of precipitation. The extra heat provided by the UHI leads to greater upward motion, which can induce additional shower and thunderstorm activity near major urban centers.

2.2 Aerosols

2.2.1 Aerosol Observational Studies

Recent research shows that anthropogenic aerosols generated in urban and industrial sites can act to alter precipitation patterns in many different cloud systems, including South Asian atmospheric brown clouds (Ramanathan et al. 2001), smoke clouds over the island of Borneo (Rosenfeld 1999), warm and cold weather clouds (Rosenfeld 2000), cold clouds over mountains (Borys et al. 2000; 2003), shallow orographic clouds (Givati and Rosenfeld 2004), clouds near the front range of the Rocky Mountains (Jirak and Cotton 2006) and convective clouds over and downwind of St. Louis, Missouri (van den Heever and Cotton 2006). In urban environments, where fine mode anthropogenic aerosols from pollution are abundant, cloud microphysical processes are modified, impacting regional precipitation.

As stated in Chapter 1, cloud microphysical processes are affected by changes in the aerosol concentration and PSD. Aerosols serve as CCN and thus have a substantial effect on cloud properties and the initiation of precipitation. Cloud seeding, a form of intentional weather modification (Hill and Ming 2012), attempts to change the amount or type of precipitation by use of aircraft or ground generators to disperse aerosols into the air that serve as CCN/GCCN. The usual intent is to increase precipitation (rain or snow), but hail and fog suppression are also widely practiced at airports. The most common chemicals used for cloud seeding include silver iodide and dry ice (solid carbon dioxide). Liquid propane, which expands into a gas, has also been used. This can produce ice crystals at higher temperatures than silver iodide. Hygroscopic materials, such as salt, have also been used. Seeding of clouds requires the presence of super

cooled liquid water, and ingestion of a substance such as silver iodide, which has a crystalline structure similar to that of ice, will induce freezing nucleation.

Difficult to pin down, the effects of aerosol presence range from enhancement to suppression. High aerosol concentrations in winter orographic clouds (polluted) have been found to yield more cloud water, but less rainwater than the same type of clouds with low aerosol concentrations (Rosenfeld 2008). Studies in Israel suggest that the indirect effects of anthropogenic sulfates may have contributed to the Sahelian drying trend, which is the observed decline in rainfall over the ecoclimatic and biogeographic zone of transition between the Sahara desert in the north and the Sudanian savannas in the south. It stretches across the north of the African continent between the Atlantic Ocean and the Red Sea and has a semi-arid climate.

Spatially varying aerosol-related forcing (both direct and indirect) has been shown to substantially alter low-latitude circulation and rainfall (Lensky and Rosenfeld 1996). Urban and industrial air pollution has also been shown to suppress rain and snow, as precipitation losses over topographical barriers downwind of major coastal urban areas in California and Israel are up to 15 – 25% of the region's annual precipitation (Rotstayn and Lohmann 2002). It is theorized that air pollution aerosols ingested into cold weather orographic clouds increase the concentration of small droplets and slow down cloud-drop coalescence and riming on ice precipitation, delaying the conversion of cloud water into precipitation.

Due to their size, small droplets have a lower probability of becoming precipitable water. Sunlight is Mie (i.e., all wavelengths are equally scattered) scattered from the droplets so that the emergent clouds appear white. The best example of this are 'fair weather' cumulus clouds, while those with higher buoyancy (i.e., cumulonimbus) climb higher, form thicker clouds, and thus

produce heavier rainfall. Cloud droplets are typically 0.01 mm in diameter or smaller, they are light, and effectively float freely in the air.

According to Kirshen (2007), approximately 37% of the energy input into the atmosphere occurs by the release of latent heat from vapor condensation into cloud drops and sublimation into ice crystals. Re-evaporation of clouds consumes the released heat. This heat of condensation and sublimation is available to energize convection and larger-scale atmospheric systems. Other studies showed that cloud microphysics affects surface processes by modification of surface sensible and latent heat fluxes (Lau and Kim 2006; Rosenfeld 2008).

2.2.2 Aerosol Modeling Studies

A large part of the present research will be conducted using a numerical cloud-resolving model. Therefore, it is important to investigate how modelers have attempted to solve problems involving precipitation and aerosols. In one of the first attempts at analyzing cloud physics, Bowen (1950) developed a theory to account for the initial growth of droplets by condensation, followed by the growth of a small fraction of droplets by collision and coalescence. The theory posits that droplets grow during their ascent through the cloud until they are large enough to remain in suspension in the upward air current, after which they fall as rain.

Takeda (1971) advanced numerical efforts by including investigation of a 2-D precipitating convective cloud via integration of the hydrodynamic and thermodynamic equations. Calculation of cloud water content and other variables became possible with this approach. More advanced models have been used to study the evolution of raindrop size spectra.

After 1980, researchers began to include lognormal size distributions to represent droplet spectra in multi-dimensional cloud models (Yau 1980; Clark 1983). Post 1990, cloud modeling progress included alterations to the collection growth equation, and more practical 3-D models (Verlinde 1990; Kogan 1990; Williams 1995).

Investigation of the effects of aerosols on precipitation showed that accounting for CCN spectra improves the estimate of cloud droplet number concentration (Cohard 1998). Analysis of the effect of isobaric mixing of saturated and dry volumes with different temperatures suggests that this mixing may lead to high supersaturation values, enhancing precipitation (Korelev and Isaac 1999). Over multiple supersaturation events, a small proportion of cloud droplets may reach sizes large enough for them to grow effectively through collision and coalescence.

Grabowski (1999) established that aerosols have minor effects on the large-scale flow and on temperature/moisture profiles for the case of large-scale flows driven by sea surface temperature (SST) gradients and prescribed radiative cooling in tropical climates. Grabowski et al. (1999) found that smaller cloud drops and slower rates of autoconversion often results in enhanced cloud mass fluxes, a colder and drier boundary layer, larger surface energy fluxes, a warmer and more humid free-atmosphere, and lower convective available potential energy (CAPE) rates. Small droplets have a lower probability of becoming precipitable water than large droplets because it is difficult for them to grow to a size that allows collision and coalescence to take place.

Simulations by Feingold et al. (1999) in the tropics illuminated the effects of cloud microphysics on the mean state of the tropical atmosphere and on the tropical climate. Inclusion of CCN and GCCN in varying concentrations allowed for determination of optimal concentrations for transformation of a non-precipitating stratocumulus into a precipitating state.

Higher concentrations of GCCN were required at higher CCN concentrations to form precipitation; however, at lower CCN concentrations, drizzle was often active and the addition of GCCN had little impact. In agreement with the previously mentioned study, other studies suggest that the aerosol effect on precipitation is secondary to the effects of atmospheric dynamics, (Hu et al. 1998; Atlas and Ulbrich 2000) and surface to atmosphere interactions such as UHI induced storms. Feingold et al. (2009) suggests that aerosol composition affects water budgets markedly less than do concentration and particle size.

Liu et al. (1997) and Wang (2002) also showed that cloud structures in large scale storms are sensitive to changes in cloud microphysics, although rain intensity may not be greatly affected. Idealized simulations in tropical climates with a cloud-resolving model showed that aerosols and cloud microphysics have minor effects on the large-scale flows, as well as on temperature and moisture profiles (Grabowski 2000; 2003).

Despite significant advances in cloud physics, many problems still exist in state-of-the-art microphysical cloud modeling. Progress is hampered by many remaining gaps and uncertainties in current knowledge of cloud microphysics and by limitations of numerical approaches in representing some known microphysical processes (Khain et al. 2000).

Many modeling scenarios have been attempted, including the effect of turbulence and quasi-equilibrium convective radiation on the mesoscale and microscale (Blei 2002; Wang et al. 2002; Grabowski 2003). Saleeby and Cotton (2004; 2008) conceptualized a microphysical module within the Regional Atmospheric Modeling System (RAMS) in which air parcel growth over time can be tracked. CCN activation is parameterized through the use of a bin emulating model that considers ambient cloud conditions for the nucleation of cloud droplets on aerosols. Using this module, researchers investigated aerosol impacts on Florida storms, and demonstrated

that variations in aerosol concentrations have a significant impact on both microphysical and dynamical characteristics of convective storms over the peninsula, as well as on accumulated surface precipitation (van den Heever et al. 2006). Investigations of the impacts of urban-enhanced aerosol concentrations on convective storm development and precipitation over and downwind of St. Louis by van den Heever and Cotton (2007) showed that urban-forced convergence downwind of the city, rather than the presence of greater aerosol concentrations, determines whether storms actually develop in the downwind region. Once convection is initiated, urban aerosols modify the dynamics and microphysics, thereby altering precipitation totals, patterns and rates. Work by Fan et al. (2012) showed that changes in aerosol concentration taken from ground based remote sensors with arbitrary PSD (since this data was not available) changes the timing of storms and temporal distributions of precipitation in China.

Studies over Houston showed that high aerosol concentrations can result in non-monotonic accumulated precipitation behavior. Increases of up to 26%, when compared to low aerosol concentration runs were found (Carrio et al. 2010). Increasing CCN concentration in cloud-resolving models has been shown to reduce cloud droplet particle size while increasing the probability of liquid becoming super-cooled without experiencing collision and coalescence (Carrio and Cotton 2007; Cheng 2009). Changes in cloud type and the vertical distribution of clouds can have a profound impact on the earth's climate through subtle feedbacks in the thermodynamics/dynamics of the cloud system.

Ntelekos et al. (2009) used a fully coupled meteorology-chemistry-aerosol mesoscale model (WRF-Chem) to assess aerosols effects on intense convective precipitation over the northeastern US. Results show that increasing aerosol concentration can lead to both enhancement and suppression of precipitation. Storms developing over areas with medium to

low aerosol concentrations showed a suppression effect on rainfall independent of meteorological environment, while storms developing in areas of relatively high particulate concentrations showed enhancement of rainfall when there were simultaneous high values of CAPE, relative humidity and wind shear. In these cases, elevated aerosol concentrations resulted in stronger updrafts and downdrafts and in more coherent organization of convection. These results suggest that areas of the northeastern US urban corridor which includes NYC, close to or downwind of intense sources of aerosols, could be more favorable for rainfall enhancement due to aerosol types and concentrations typical of the region.

Table 1 provides a summary of microphysical modeling efforts discussed above that are relevant to the present research. The previous numerical attempts could greatly benefit from implementation of actual observed PSD data. PSD and concentration can vary from day to day, as shown in Fig. 5. These data are based on measurements taken on the northern coast of Puerto Rico with six-channel handheld radiometers (Comarazamy et al. 2006). Radiometer readings were converted into PSDs through the use of an inversion algorithm (Dubovik and King, 2000; Otero, 2003). Results using RAMS with the data from Fig. 5b are presented in Fig. 5c and 6. Figure 5c compares a simulation in which PSD taken from the Arecibo Observatory (AO) is ingested into RAMS with cases in which the concentration of small aerosols or CCN is increased, the concentration of GCCN is increased, and both CCN and GCCN are increased. Results show that PSD and CCN/GCCN particle concentration are both important in cloud and precipitation processes via both modification of cloud radiative properties and nonlinear interactions.

Enhanced GCCN concentration increased total accumulated precipitation, while enhancement of both CCN and GCCN concentrations suppressed rainfall, as surrounding water

vapor must be shared amongst more particles with increased aerosol concentrations. As a result, individual droplets take longer to grow to sizes that allow collision and coalescence to occur, slowing autoconversion rates. Although increasing the GCCN concentration acts to increase precipitation, the inclusion of more CCN means that all cloud particles will have to compete for the water vapor in the atmosphere. As a result, cloud droplets will not easily grow to rainfall size.

Figure 6 shows precipitation in polluted and non-polluted air. Total precipitation in polluted air is less than a third of that in clear air. These results give further support that aerosols impact precipitation in coastal Puerto Rico, and have implications for the present research goals, directed towards determining the effect of aerosols on precipitation in a complex coastal urban environment.

In summary, urbanprecipitation processes involve contributions from large scale forcing and from local urban effects, such as UHI induced convection and modification of cloud microphysics due to aerosol ingestion into the atmosphere from urban sources. Urban effects on precipitation may be synthesized as pointed out by Fig. 7. Wind, UHI, convergence/divergence and aerosols all impact precipitation in the urban environment. Where wind, UHI, and convergence/divergence primarily affect storms, aerosols seem to affect storms after initial formation due to the other three parameters, based on the ideas of Bornstein (2011) but created by Grimmond (2011) and Shepherd (2011).

When calm conditions combine with a strong UHI and convergence into the city, a precipitation maximum will occur over the urban center because convection will be highest where temperature is warmest. When strong winds combine with divergence upwind of the city and convergence downwind, precipitation will be diverted around the city; with maximum precipitation amounts resident in lateral and downwind convergence zones (This was shown in

Fig. 4) When weak regional winds are present during a UHI and flow converges downwind of the urban boundary, the maximum precipitation will be advected to the downwind urban edge.

Where previous studies have shown the importance of aerosol concentration and urban effects on rainfall over cities, the present study aims to go further in depth by investigating variation of observed PSD and LCLU in localized and mesoscale events at high horizontal resolutions (e.g., on the order of 1km) in New York City (NYC). Advancing the present state of weather prediction and analysis requires the ingestion of updated observed aerosol information. The present research aims to improve forecasting accuracy by investigating experiments with and without ingestion of aerosol data from the Aerosol Robotic Network (AERONET), which will be explained in the next Chapter.

Table 1 Summary of numerical cloud microphysics studies.

Author, Year	Modeling Component	Features	Observations
Bowen, 1950	Condensation, Collision & Coalescence	Accounts for the initial growth of droplets by condensation then by coalescence. These grow in their ascent through the cloud until they are large enough to fall as rain.	Maximum height reached by the drops increases with increasing vertical air velocity Size of the drops emerging from the cloud base is nearly a linear function of the height. The time for the precipitation to appear is an inverse function of the upward air velocity.
Takeda, 1970	Hydrodynamic, Thermodynamic Equations	Precipitating convective cloud is simulated in a two dimensional model Size distribution is described in terms of seven discrete radii. Cloud and rain water contents, rainfall intensity and radar reflectivity are computed directly from the size distributions.	If the atmosphere is sufficiently unstable and vertical shear in the ambient wind is very weak, new convective clouds form on both sides of the initial cloud. Vertical wind shear is not intensified by the initial cloud. If the height of a jet of air is too low or too high, it has little effect on the convection of the cloud. Long lasting convective cloud has a greater chance to develop severely than a short-lived cloud.
Rogers & Yau, 1989	Condensation, Collision & Coalescence	Text that explains cloud microphysics and various types of precipitation. Cloud properties, types of clouds, precipitation processes, weather modification and more. Precipitation due to convection.	Simplified model of droplet and population growth. Outlines the methodology for determining the droplet population evolution. Discusses and compares many numerical models.
Verlinde et al , 1990	Collection Growth	Closed form solution for the collection growth equation as used in bulk microphysical parameterizations is derived. Solution is used to evaluate two commonly used approximations.	Results suggest that careful consideration to allowable hydrometeor characteristic diameter should be given since these approximations can under or over estimate the collection process by several orders of magnitude.
Hu et al, 1997	Collision, van der Waals forces	The stochastic growth of cloud droplet distributions due to collection processes is studied using a detailed	The van der Waals forces are effective in enhancing droplet collision when the droplets are small and the

		microphysical parcel model. The evolution of rainwater content (*LR*) and the radar reflectivity factor (*Z*) are plotted in order to trace the progress of transfer of cloud water into rainwater and determine the importance of droplet collection in different size ranges.	distributions are narrow. Wake capture is negligible for clouds forming in a continental air mass with low liquid water contents. However, it is effective when coalescence becomes the dominant growth process and rainwater content has reached high values. When non unity coalescence efficiencies are used, the drop growth and cloud water to rainwater conversion is reduced compared to the traditional unity coalescence efficiencies used in previous modeling studies. The major difference between the results using non unity and unity coalescence efficiencies is due to the extrapolation of coalescence efficiencies measured in laboratory to size domains outside the domain of the measurements.
Khairoutdinov & Kogan 1999	Condensation, Collision & Coalescence, Autoconversion	Bulk microphysical approach applied to the marine boundary layer clouds. CCN count is a separate prognostic variable. This allows one to predict the cloud drop concentration based on supersaturation in a manner similar to the explicit microphysical model. Couples detailed representation of turbulence in the LES model with cloud microphysics. Prediction of the drop concentration together with the cloud water content provides an opportunity to determine the characteristic cloud drop size, which is important for drizzle initiation. Two key drizzle parameters are predicted: drizzle water content and drizzle drop concentration. Comparisons of LES simulations using the new bulk microphysics with the simulations using the explicit microphysics for two cases representing a non-drizzling and a heavy	The results from the non-drizzling case that the bulk model was able to predict the cloud drop concentration profiles as well as the drop spectrum relative dispersion reasonably close to the prediction of the much more sophisticated explicit microphysical model. For the heavy drizzling case, evolution of the STBL simulated by the bulk microphysical model was in close agreement with the explicit model. The use of the bulk microphysical parameterization in LES models of STBLs enables one to simulate phenomena in larger spatial domains and for longer simulation times than is currently possible with an explicit microphysical model.

		drizzling scenario.	
Grabowski , 1999	Condensation, Collision & Coalescence, Convection, Radiative Cooling	Discusses the role that cloud microphysics play in the tropical climate. Two sets of highly idealized cloud-resolving simulations are discussed. In each set, the simulations differ only in the parameters applied in the representation of cloud microphysics. The simulations are run until quasi-equilibrium between sinks and sources of moisture and energy is achieved. The comparisons between simulations applying dramatically different parameters exposes the effects of cloud microphysics on the mean state of the tropical atmosphere and on the tropical climate. The first set considers large-scale flow driven by sea surface temperature gradients and prescribed radiative cooling. The second set considers tropical convection over a shallow isothermal layer of water (‘‘swamp ocean’’) applying an interactive radiation transfer model.	The cloud microphysics appears to have minor effects on the large-scale flow as well as temperature and moisture profiles within ascending branches featuring deep convection. The sea surface temperature beneath each column of the atmospheric model changes according to the local budget of surface heat and radiative fluxes. For simplicity, equatorial equinox conditions, no diurnal cycle, and a zero zenith angle are assumed. Changes in parameters in cloud microphysics appear to have a dramatic impact on the quasi-equilibrium ocean temperature that ranges from about 378–388C in the simulation assuming large cloud and precipitation particles to 328–358C in the simulation assuming small particles. Results suggest that the main effect of cloud microphysics is not on atmospheric processes and dynamics but rather on the ocean surface. If this suggestion is realistic, effects of cloud microphysics will be very difficult to quantify in the ocean–atmosphere system because of the much longer timescales associated with ocean dynamics.
Khain et al, 2000	Condensation, Collision & Coalescence	Review article about the state-of-the-art numerical modeling approaches for cloud microphysics. An assessment of several important problems of warm and ice microphysics and model limitations. Identification of areas where improvements are most urgently needed.	Despite significant advances in cloud physics, many problems exist in the state-of-the-art microphysical cloud modeling. The progress is hampered by many remaining gaps and uncertainties in our knowledge of cloud microphysics and limitations of numerical approaches in representing some of known microphysical processes. Of greatest concern is the spectral microphysical approach, which does not restrict the particle size spectra to any particular shape and, therefore, claims to reproduce formation of size spectra of cloud particles.
Wang et al,	Condensation,	Aims at understanding this dynamical–microphysical	Results show that the turbulence contribution to the mean

2002	Turbulence	interaction and providing information necessary for parameterizations of the ensemble mean condensation rate and turbulent fluxes of liquid water variables in a coupled turbulence–microphysics model. Simulates non-precipitating stratocumulus clouds with a coupled large eddy simulation and an explicit bin microphysical model, and performs a budget analysis for four liquid water variables: mean liquid water content, turbulent liquid water flux, mean cloud droplet number concentration, and the number density flux.	condensation rate comes from covariance of the integral cloud droplet radius and supersaturation, which enhances condensation in turbulent updrafts and reduces evaporation in the downdrafts. Condensation timescale regulates the turbulence fields, as does the number concentration, because it affects the condensation fluctuation, which is highly correlated with the turbulence vertical motion. A saturation adjustment cloud model, which diagnoses liquid water content at its equilibrium level, instantly condenses (evaporates) all available water vapor (liquid water) surplus. Consequently, there is likely to be a systematic difference between the turbulence field resolved with this type of model and that with a supersaturation based cloud scheme for which a finite condensation timescale applies.
Sommerfeld, 2002	Collision & Coalescence	Stochastic droplet collision model based on the creation of a fictitious collision particle taking impact efficiencies into account. O'Rourke's model is considered to predict the outcome of water-droplet collisions (being grazing or coalescing) and to predict post-collision velocities. The relevance of impact efficiencies is discussed for water droplet collisions on the basis of the inertial parameter. Normalized critical displacements and collision frequencies are compared.	The effect of impact efficiency has a significant influence on collision frequencies and therefore on coalescence rates if the small droplet`s Stokes number is smaller than 10. A step function (like the Schuch and Löffler model) does not effectively describe the distribution of the number-impact efficiency for turbulent flows across the injection plane located normal to the relative flow direction. The distribution of the impact efficiency depends on the turbulence intensity, the droplet-Stokes number, the diameter ratio of small and large droplets and the larger droplet's Reynolds number. Gaussian distribution functions are more appropriate to describe the impact efficiency in turbulent flows. Numerical calculations based on the Lagrangian approach revealed the proper implementation of the model and the importance of considering interception effects in modeling collision efficiency.

Grabowski , 2003	Condensation, Collision & Coalescence, Convection, Radiative Cooling	Investigates how cloud microphysics impact global convective–radiative quasi equilibrium on a constant-SST aquaplanet. The approach resolves both global dynamics and cloud-scale dynamics, as well as smallscale coupling among convective, radiative, and surface processes, within a single computational framework.	The results suggest that cloud microphysics impact quasi-equilibrium temperature and moisture profiles substantially, but the relative humidity is only weakly affected. Small cloud and precipitation particles result in a climate that is warmer and moister. This is explained by the impact of cloud microphysics on the coupling between convection and surface exchange during the approach to quasi equilibrium. With interactive radiation, this effect is supplemented by gradual evolution of mean cloud fraction profiles and the mean radiative cooling. The mean quasi-equilibrium radiative cooling is weaker in the simulation featuring small cloud and precipitation particles. Cloud–radiation interactions, explicitly treated in CRCP, play a significant role in setting up the quasi equilibrium cloudiness. These simulations support the theory that the main impact of cloud microphysics in the Tropics is on the net energy budget at the ocean surface.
Saleeby & Cotton, 2004	Condensation, Collision & Coalescence	Large droplet mode, prognostic number concentration	Cloud2 mode slows reduces rain production Increasing concentration of CCN reduces the surface accumulation of rain. Increasing the number concentration of GCCN produces an increase in the surface accumulation of rain.
Grabowski, 2005	Condensation, Collision & Coalescence	Cloud-resolving modeling study concerning the impact of warm-rain microphysics on convective–radiative quasi equilibrium with fixed surface characteristics and prescribed solar input, both mimicking the mean conditions on earth. Two concentrations of cloud droplets, either 100 cm_3	The assumed concentration of cloud droplets affects the local value of the effective radius of cloud droplets and the transfer of cloud water into drizzle and rain. Cloudiness is dominated by shallow convection.

		(referred to as “pristine”) or 1000 cm_3 (referred to as “polluted”), are considered. Three formulations of the effective radius of water droplets in diluted cloudy volumes are used, corresponding to the homogeneous, intermediate, and extremely inhomogeneous mixing scenarios.	The impact of warm microphysics is dominated by the first indirect effect, whereas the second indirect effect has a smaller impact. The second indirect effect highlights the difference between the impact of cloud microphysics on a single cloud and the impact on an ensemble of clouds, with only the latter including the feedbacks between clouds and their environment. The formulation of the effective radius in the diluted cloudy volumes is of great importance, with the amount of solar energy reaching the surface being the same in the pristine case assuming the homogeneous mixing scenario and in the polluted case with the extremely inhomogeneous mixing.
Wang et al, 2005	Coalescence & Turbulence	Attempts to explain how rain forms in warm cumulus as rapidly as it has sometimes been observed. Three aspects related to the air turbulence and stochastic coalescence are considered here in an attempt to resolve this open question. The first is the enhanced geometric collision rates caused by air turbulence. The second is the effect of air turbulence on collision efficiencies. The third is stochastic fluctuations and correlations in the collision–coalescence process.	Preliminary results indicate that turbulence could shorten the time for drizzle formation to about a half of the time needed for the same growth process based on hydrodynamic–gravitational mechanism alone (enhanced geometric collision rates by air turbulence may reduce the time for drizzle formation due to coalescence by about 40%).

Comarazamy et al, 2006	Condensation, Collision & Coalescence	New cloud microphysics module incorporated in a regional atmospheric model Atmospheric particle (AP) observations performed at the Arecibo Observatory were used to simulate two short precipitation events observed in the area of the observatory, and to investigate the possible effects of AP on cloud formation and rain development. Runs were performed with and without the new cloud module, initialized with the new AP dataset and the previous cloud spectrum available.	The combination of the new cloud module and the Arecibo observations produced the most satisfactory results and significant improvements in total precipitation modeled; 70mm vs. 80mm observed. The improvement results in 15% more precipitation predicted when compared with the old cloud information, and more than 50% with respect to simulations without cloud condensation nuclei activation. Idealized runs showed that cloud droplet production is significantly larger in polluted air than in clear skies and that rainwater in polluted air is less than that in unpolluted air.
Grabowski, 2007	Condensation, Collision & Coalescence	Two-moment warm rain bulk microphysics scheme to determine the effect of atmospheric aerosols on ice-free clouds in large-eddy simulation (LES) models. Emphasis is on prediction of supersaturation, activation of cloud droplets, and the representation of microphysical transformations during parameterized turbulent mixing. Simulates droplet activation at the cloud base, in the cloud interior due to increasing updraft strength, and at the lateral edges due to entrainment. An approach for predicting the supersaturation field is proposed, with an emphasis on its application in an Eulerian framework. This scheme is designed to be as flexible as possible, allowing for the entire range of mixing scenarios from homogeneous to extremely inhomogeneous.	Extremely inhomogeneous mixing results in substantially smaller mean droplet number concentration, larger effective radius, and smaller cloud optical depth compared to the run with homogeneous mixing. The subgrid mixing of cloud condensation nuclei (CCN) and formation of CCN from evaporated droplets during extremely inhomogeneous mixing are relatively less important for this case.

Cheng et al, 2009	Condensation, Collision & Coalescennce	RAMS was used in Large Eddy Simulation (LES) mode, two moment bin-emulating microphysics with new features of explicit nucleation of small cloud droplets. CCN & GCCN are ammonium sulfate.	High CCN Low GCCN- lowest precipitation rate High CCN High GCCN- highest precipitation rate. If CCN concentration is fixed, potential temperature decreases.
Ntelekos et al, 2009	Condensation, Collision & Coalescennce	(WRF-Chem) has been used to assess the effects of aerosols on intense convective precipitation over the northeastern US.	Results suggest that increasing concentrations of aerosols can lead to both enhancement and suppression of precipitation. Storms developing over areas with medium to low aerosol concentrations showed a suppression effect on rainfall independent of the meteorological environment, while storms developing in areas of relatively high particulate concentrations showed enhancement of rainfall when there were simultaneous high values of CAPE, relative humidity and wind shear. In these cases, elevated aerosol concentrations resulted in stronger updrafts and downdrafts and in more coherent organization of convection.
Carrio et al, 2010	Condensation, Collision & Coalescennce	(RAMS) has been used to assess the effects of LCLU and aerosols on convective cells triggered by sea breeze circulation over Houston.	The intensification of sea breeze circulation increased with urbanization. Due to increased exposure to aerosols, the upper levels of the convective cells downwind of the city were invigorated by greater latent heat release linked to higher amounts of liquid water transported to super-cooled levels. Precipitation did not show sole suppression or enhancement with varying aerosol intensity.

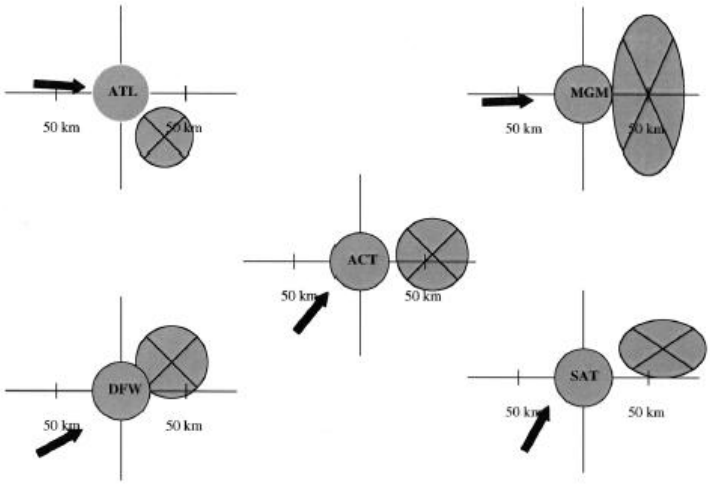

Fig. 4: Summary of the downwind locations for 5 cities experiencing significant urban-impacted rainfall (shaded cross region) in warm-season months. This analysis is based on the 3 year, warm-season rainfall rate analysis provided by TRMM precipitation radar. The arrows represent the mean prevailing wind direction (from Shepherd et al. 2002).

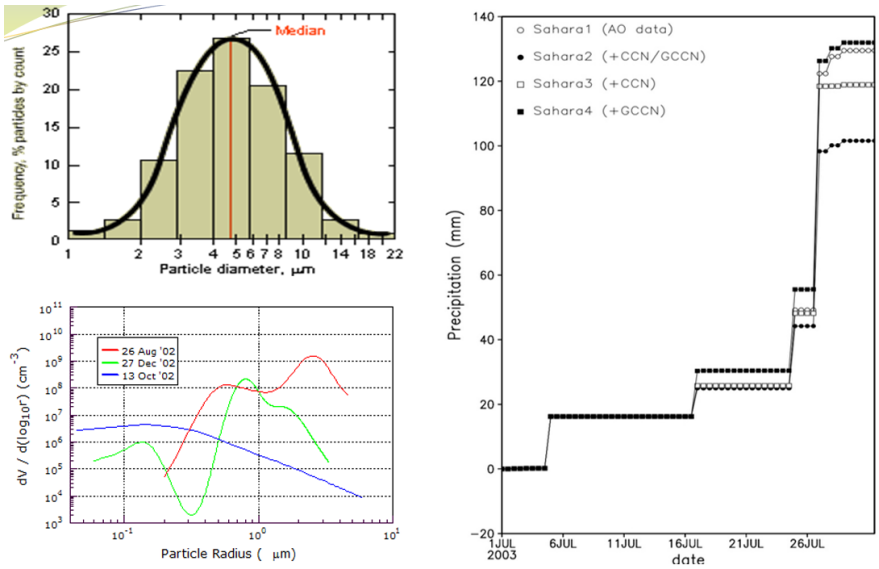

Fig. 5: Variation of particle size distribution for the coastal urban environment of Puerto Rico (Comarazamy et al. 2006). Right panel- Surface precipitation totals for observed data (°), increases in both CCN and GCCN (•), increases in only CCN (□) and increases in only GCCN(■) (Comarazamy et al. 2006).

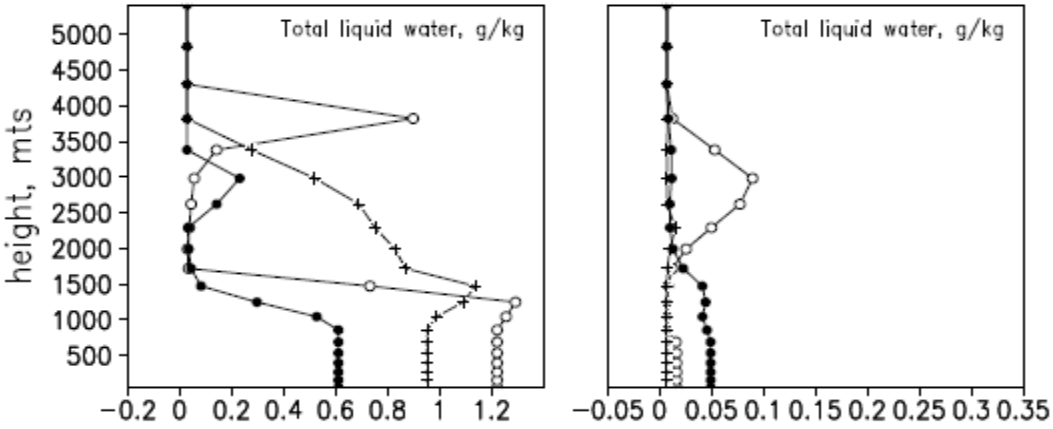

Fig. 6: Simulation of PCP in non polluted (right) and polluted air (left) (Comarazamy et al. 2006).

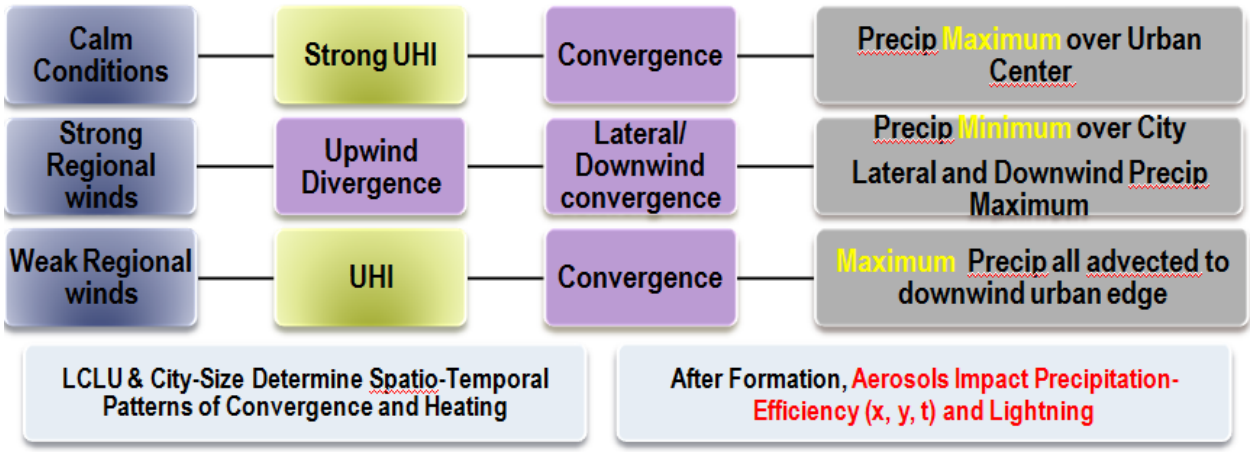

Fig. 7: Synthesis of urban effects on precipitation. After the dynamics (wind, UHI, and convergence/divergence) create the conditions for rainfall, aerosol modification can occur. Based on the ideas of Bornstein (2011) but created by Grimmond (2011) and Shepherd (2011).

Chapter 3

Fundamental Research Questions and Methodology

3.1 Questions and Impacts

Whereas previous observational and modeling studies have shown that variation of aerosol concentration may either increase or decrease warm-season urban precipitation amounts, and variation of LCLU may also impacts warm-season urban precipitation totals, the present research proposes to determine the coupled interaction effects of observed PSD and high resolution LCLU on precipitation for localized and MCC events in a complex coastal-urban environment. In the following sections, the pertinent questions and impacts of this research will be listed.

3.1.1 Science Questions

Based on the analysis of past research, the specific scientific questions posed by the current research include:

Major Question:

How do aerosols affect precipitation in an urban environment?

Sub Questions:

(a) How does variation of aerosol PSD affect total precipitation?

(b) How does the combination of land cover, land use (LCLU) and PSD affect precipitation totals and amounts?

(c) Can urban precipitation forecasts be improved?

The research plan is to first describe cloud microphysical processes using a Lagrangian model to approximate cloud droplet growth rates for NYC under idealized conditions. This study will be further extended by utilizing a mesoscale modeling approach with ingested/assimilated observations which include input data for aerosol PSDs and LCLU. Precipitation data from National Weather Service (NWS) surface stations around the city will be compared against experimental results. RAMS will be validated with observations and will be used to run numerical experiments with and without observed PSD and LCLU. The following sections of this chapter will describe the modeling approach and availability of data.

The author hypothesizes that varying the observed PSD influences cloud physics and will thereby impact precipitation patterns, rates, and totals over and near an urban area. Ingestion of observed bimodal PSD in atmospheric mesoscale models for complex urban regions such as NYC is new ground in climate and weather prediction. Where previous numerical studies have shown the importance of aerosol concentration and urban effects on rainfall over NYC (Ntelekos et al. 2009), this study aims to go further in depth by investigating variation of observed PSD in localized and mesoscale events at high resolution horizontal grid spacing on the order of 1 km. Through this research, the author hopes to gain insight about the role of PSD variation on

precipitation and cloud microphysics in urban environments, and to determine how aerosols and microphysics may contribute to warm-season rainfall.

NYC was chosen for the study because of its position at the meeting of the Hudson River and the Atlantic Ocean (which subjects it to large hygroscopic GCCN ingestion from evaporation of sea salt), and the fact that it is highly urbanized (leading to the ingestion of smaller anthropogenic CCN). NYC is also rich in data relevant for the research. The high concentration of tall buildings in NYC contributes to making it the densest city in the US with 26,924 per km². Its environmental issues are chiefly concerned with managing this density, which also explains why NYC is among the most energy efficient and least automobile-dependent cities in the US (Riley 2007). Its regional climate is largely affected by its proximity to the Atlantic Ocean, and its climate patterns are affected by the Atlantic Multidecadal Oscillation (AMO, Fig. 8), a 70-year-long warming and cooling cycle in the Atlantic that influences the frequency and severity of hurricanes and of coastal storms. When the AMO is positive (warm Atlantic) there is less rainfall over most of the United States and northeastern South America, and more rainfall in southern Alaska, northern Europe, west Africa, and Florida. The AMO is currently positive.

Summers in NYC are hot and humid, with temperatures commonly exceeding 32°C. On average (based on NYC weather records from 1895 to 2012), July is the hottest and wettest month (Figs. 9 - 11). Summer temperatures above 38°C are as rare as subzero lows in winter, although a maximum temperature of 41°C has been recorded on 9 July 1936, while the minimum recorded temperature was -26°C on 9 February 1934. Humidity levels are usually quite high in July and August. Thunderstorms are common in the summer, although severe weather is more common west of the city in New Jersey (NJ) because intense storms are normally killed by the

sea breeze before reaching NYC. Hurricanes are a major threat to the area; especially in the suburbs of Long Island. While relatively infrequent compared to areas south and east, a direct hit, as in the case of Hurricane Sandy in 2012, causes loss of life and property damage due to the high population in coastal areas. As forecasting super storms like Hurricane Sandy is of paramount importance, this work will determine whether ingestion of observed PSD improves storm forecasts over no ingestion scenarios. The current research will include a series of experiments that will allow the author to investigate how PSD and LCLU impact precipitation in a coastal urban environment.

3.1.2 Expected Impacts of Research

The impacts of this research could be broad. They will improve understanding of the effects of aerosols on precipitation processes in urban environments for both mesoscale and localized precipitations events. Precipitation prediction from numerical models incorporating observed data such as aerosol PSD will allow for improved algorithms, thereby increasing the accuracy of instrument measurements. Examples of the types of instruments that may benefit are the Cloud-Aerosol Light Detection and Ranging (LIDAR) Infrared Pathfinder Satellite Observation (CALIPSO) satellite, and the Geostationary Observational Environmental Satellites (GOES).

This research also aims to clarify the impact of aerosols on precipitation in complex urban environments. Previous research suggests that aerosol concentration, size, (and

composition to a lesser extent) determine whether they will enhance, inhibit, or not affect precipitation at all (Kessler 1994; Jauregui and Romales 1996; Shepherd et al. 2002; Diem and Brown 2003; and Ntelekos et al. 2009). Although many studies have been conducted for major cities, at the present time no clear cut suggestion as to the percent contribution of observed PSD ingestion on localized precipitation in NYC. This research aims to determine this contribution.

3.1.3 Observed Data and Event Descriptions

Figure 12 shows NWS precipitation data for the NYC/New Jersey (NJ) region during July 2007. Precipitation events took place on 5, 11, 18, 23, and 29 of July 2007. Both 11 and 18 and July 2007 were selected as specific case studies because the rainfall variability across the region is much higher in these cases than for the rest of the events (and b/c of the availability of AERONET data). This rainfall variability suggests that the urban environment may have impacted precipitation patterns here. Although five sites are shown in Fig. 12, over 60 sites are available from NWS and WeatherBug (www.weatherbug.com). For the purposes of this research, all analyses were performed on 16 sites (Table 2). Figure 13 shows the locations of the 16 NWS sites, the Upton, NY radiosonde site, and the CCNY AERONET site over topography of the region.

On 11 July 2007, total precipitation across the 16 sites range from 0-50 mm and individual storms did not move very far from their original commencement points. Investigation of weather maps in Chapter 4 will uncover the cause of this event. On the morning of 18 July 2007 a regional storm traveled across Long Island, causing massive flooding and crippling the

morning rush hour (Wyllie 2008). Regional storms that form due to strong warm air advection into the environment by a southerly low-level jet stream, strong moisture advection which increases the relative humidity of the environment, convergence of air near the surface, and divergence of air high above the surface are known as Mesoscale Convective Complexes (MCCs). MCCs producing large rainfall amounts and spawning tornadoes do not usually occur in NYC, however, nearly 25 mm of rain fell on Central Park in less than an hour, and almost 50 mm fell on LaGuardia. Total precipitation across the 16 sites range from 0-97 mm. The intense rain led to widespread urban and small stream flooding, causing an array of power outages, airport and mass transit delays, and traffic backups.

3.2 Cloud Microphysics

Cloud microphysics models enable researchers to determine the optimal conditions for rainfall to occur. These models also allow for ingestion of cloud data such as PSD and aerosol concentration obtained from satellite and ground observations for real case analysis. In this section, the basic microphysical equations for warm season precipitation are presented. These equations are an integral part of the Saleeby and Cotton (2004; 2008) microphysics module in RAMS, and allow for prediction and analysis of precipitation events. The algorithm provides a detailed description of the initial stages of parcel growth and evolution. The basis for the present research approach is also presented by Rogers and Yau (1989). Setting up these equations in a programming language such as MatLab™ allows for simulation of rain droplet growth by

condensation for varying atmospheric conditions; availing the researcher to attain a better understanding of cloud microphysics.

Steady state diffusional growth of a single droplet at rest in a vapor field are based on the conservation laws for mass and energy. The molecular diffusion coefficient can be expressed by the following term:

$$D_t = 211 \times \left(\frac{T_t}{T_o} \right)^{1.94} \times 10^{-4}, \quad (1)$$

where T_t is the temperature at time *t* at the surface of the droplet, and T_o is the initial droplet temperature. The conservation of mass is given by:

$$\frac{dm}{dt} = 4\pi r_t D_t (\rho_v - \rho_{vr}), \quad (2)$$

where r_t is the droplet radius at time *t*, and ρ_v and ρ_{vr} are the ambient vapor density and droplet vapor density, respectively. Conservation of thermal energy is given by the following equation:

$$\frac{dQ}{dt} = 4\pi r_t K (T_t - T_\infty), \quad (3)$$

where T_∞ is ambient temperature, and *K* is the coefficient of thermal conductivity of air. In a field of saturated vapor, changes in vapor density are related to changes in temperature by

$$\frac{d\rho_v}{\rho_v} = \frac{L}{R_v} \frac{dT}{T^2} - \frac{dT}{T}. \quad (4)$$

Where *L* is the latent heat, and R_v is the water vapor gas constant. Integrating this equation from temperature T_t to temperature T_∞, and assuming $\frac{T_\infty}{T_t} \approx 1$, gives

$$\ln \frac{\rho_{vs}}{\rho_{vrs}} = (T_\infty - T_t)\left(\frac{L}{R_v T_t T_\infty} - \frac{1}{T_t} \right), \tag{5}$$

where the subscripts *s* indicate saturation vapor densities. Since $\frac{\rho_{vs}}{\rho_{vrs}}$ is close to unity, the equation is simplified to:

$$\frac{\rho_{vs} - \rho_{vrs}}{\rho_{vrs}} = \left(\frac{T_\infty - T_t}{T_\infty} \right)\left(\frac{L}{R_v T_\infty} - 1 \right), \tag{6}$$

where the approximation has also been employed that $T_t T_\infty \approx T_t^{\,2}$. Substituting from Eq. (3) for $(T_\infty - T_t)$ gives:

$$\frac{\rho_{vs} - \rho_{vrs}}{\rho_{vrs}} = \left(\frac{L}{4\pi r K T} \right)\left(1 - \frac{L}{R_v T_\infty} \right)\frac{dm}{dt}. \tag{7}$$

From Eq. (2)

$$\frac{\rho_v - \rho_{vr}}{\rho_{vr}} = \left(4\pi r D \rho_{vr} \right)^{-1} \frac{dm}{dt}. \tag{8}$$

To compensate for the droplet curvature and solute effects, two terms from the Kohler theory are implemented. Droplet curvature *a* is given by:

$$a = \frac{(3.3\times10^{-7})}{T_t}. \tag{9}$$

For the solute term *b*:

$$b = 2 \times \frac{M_s}{m_s} \times 4.3\times10^{-6}, \tag{10}$$

where M_s and m_s are the molecular weights of the solute constituent and the particle, respectively.

The Kohler curve in Fig. 14 shows the supersaturation of a vapor (which occurs when the vapor pressure exceeds the normal saturation vapor pressure) at a given temperature. The exact shape of the curve is dependent upon particle mass and composition of the solute (Low 1969). The supersaturation level at which the drop will grow without bound is called the critical supersaturation. The radius at which the curve peaks is called the critical radius.

Ambient vapor pressure, E_t, is

$$E_t = \frac{\rho_v \times R_v \times T_t}{100}, \tag{11}$$

and saturation vapor pressure, E_{st}, is:

$$E_{st} = \left(\frac{6.112}{1013.25}\right) \times \exp\left(\frac{\left(17.67 \times \left(T_t - 273\right)\right)}{\left(T_t - 273 + 243.5\right)}\right) . \tag{12}$$

Saturation is defined as the ratio of the two previous pressure terms:

$$S_t = \frac{E_t}{E_{st}}. \tag{13}$$

Growth of a droplet by diffusion depends on both thermal and mass vapor diffusion. Coefficient terms for F_{kt} and F_{dt} result from conservation of energy and mass using the droplet as control volume, respectively:

$$F_{kt} = \left(\frac{L}{R_v * T_t} - 1\right) \times \left(\frac{L \times \rho_l}{K \times T_t}\right), \tag{14}$$

and

$$F_{dt} = \left(\frac{\rho_l \times R_v \times T_t}{D_t * E_{st}} \right) . \quad (15)$$

Finally, the growth of a CCN particle may be tracked by using the following equation.

$$r_t \times \frac{dr_t}{dt} = \frac{\left(S_t - 1 - \frac{a}{r_t} + \frac{b}{r_t^3} \right)}{F_{kt} + F_{dt}} . \quad (16)$$

When studying droplet populations in a rising parcel, it is necessary to incorporate the rate of change of saturation for a droplet population:

$$\frac{ds}{dt} = \left(\frac{1}{T_t} \times \frac{\varepsilon \times L \times g}{R * Tt} - \frac{g}{R}\right) \times \frac{dz}{dt} - \rho_l \times \left(\frac{R \times T_t}{\varepsilon \times E_{st}} + \frac{\varepsilon \times L^2}{p \times Tt \times c_p}\right) \times \frac{dX}{dt} , \quad (17)$$

where ε the gas constant ratio, z is the vertical distance from ground level, X is the liquid water mixing ratio, g is the gravitational acceleration, c_p is the constant pressure specific heat, and ρ_l is the density of liquid water. The particle distribution function is given by:

$$N(r) = \frac{N_t}{r_t \times \sqrt{2\pi} \times \ln \sigma} \times exp\left\{ \frac{-\left(\ln\left(\frac{r_t}{r_g}\right)\right)^2}{2 \times (\ln \sigma)^2} \right\} . \quad (18)$$

When droplets are growing by condensation under conditions of steady supersaturation, it is possible to solve for the distribution at any time given its form at an earlier time. Equations (8-18) describe particle growth by condensation only. To have a more complete understanding of warm season precipitation formation, the following set of equations which model collision and coalescence, must also be included. Terminal velocity of a particle, u_T, is dependent on its size, and may be determined by the following three equations, based on conservation of momentum and mass:

$$u_T = k_1 \times r_t^2 \quad (19)$$

when $r_t < 30\mu m$,

$$u_T = k_2 \times r_t^{0.5} \tag{20}$$

when 0.6mm < r_t < 2mm, and

$$u_T = k_3 \times r_t \tag{21}$$

when 40μm < r_t < 0.6mm.

Collision efficiency between two droplets is given by:

$$E = \frac{x_o^2}{(R_t + r_t)^2}. \tag{22}$$

Where x_o is the impact parameter, and R_t is the large droplet. The rate of change of the large droplet with regards to time is:

$$\frac{dR_t}{dt} = \frac{\overline{E} \times M}{4 \times \rho_l} \times u_T, \tag{23}$$

Where $\bar{E}$ is an effective average value of collection efficiency for a droplet population, and M is the cloud liquid water content. For a small updraft, the rate of change of particle radius with respect to altitude is:

$$\frac{dR_t}{dz} = \frac{\overline{E} \times M}{4 \times \rho_l}. \tag{24}$$

3.3 Methodology

Now that the basic warm microphysical processes have been explained in the preceding section, it is now possible to look into the more advanced numerical setup for RAMS, which will be the main research tool. In addition, the PSD/LCLU and pressure boundary condition data which will be ingested/assimilated into the model will also be described.

3.3.1 RAMS Model Information and Setup

RAMS is a numerical model developed at Colorado State University (CSU) for simulating and forecasting meteorological phenomena. Its major components include:

1. An atmospheric model, which performs the actual simulations.
2. A data analysis package, which prepares initial data for the atmospheric model from observed meteorological data.
3. A post-processing visualization and analysis package, which interfaces atmospheric model output with a variety of visualization software utilities.

The model is constructed around the dynamical equations that govern atmospheric motions:

$$\frac{\partial u}{\partial t} = -u\frac{\partial u}{\partial x} - v\frac{\partial u}{\partial y} - w\frac{\partial u}{\partial z} - \theta\frac{\partial \pi'}{\partial x} + fv + \frac{\partial}{\partial x}\left(K_m\frac{\partial u}{\partial x}\right) + \frac{\partial}{\partial y}\left(K_m\frac{\partial u}{\partial y}\right) + \frac{\partial}{\partial z}\left(K_m\frac{\partial u}{\partial z}\right) \quad (25)$$

$$\frac{\partial v}{\partial t} = -u\frac{\partial v}{\partial x} - v\frac{\partial v}{\partial y} - w\frac{\partial v}{\partial z} - \theta\frac{\partial \pi'}{\partial y} - fu + \frac{\partial}{\partial x}\left(K_m\frac{\partial v}{\partial x}\right) + \frac{\partial}{\partial y}\left(K_m\frac{\partial v}{\partial y}\right) + \frac{\partial}{\partial z}\left(K_m\frac{\partial v}{\partial z}\right) \quad (26)$$

$$\frac{\partial w}{\partial t} = -u\frac{\partial w}{\partial x} - v\frac{\partial w}{\partial y} - w\frac{\partial w}{\partial z} - \theta\frac{\partial \pi'}{\partial z} - \frac{g\theta_v'}{\theta_0} + \frac{\partial}{\partial x}\left(K_m\frac{\partial w}{\partial x}\right) + \frac{\partial}{\partial y}\left(K_m\frac{\partial w}{\partial y}\right) + \frac{\partial}{\partial z}\left(K_m\frac{\partial w}{\partial z}\right) \quad (27)$$

$$\frac{\partial \theta_{il}}{\partial t} = -u\frac{\partial \theta_{il}}{\partial x} - v\frac{\partial \theta_{il}}{\partial y} - w\frac{\partial \theta_{il}}{\partial x} + \frac{\partial}{\partial x}\left(K_h\frac{\partial \theta_{il}}{\partial x}\right) + \frac{\partial}{\partial y}\left(K_h\frac{\partial \theta_{il}}{\partial y}\right) + \frac{\partial}{\partial z}\left(K_h\frac{\partial \theta_{il}}{\partial z}\right) + \emptyset_\theta \quad (28)$$

$$\frac{\partial r_n}{\partial t} = -u\frac{\partial r_n}{\partial x} - v\frac{\partial r_n}{\partial y} - w\frac{\partial r_n}{\partial x} + \frac{\partial}{\partial x}\left(K_h\frac{\partial r_n}{\partial x}\right) + \frac{\partial}{\partial y}\left(K_h\frac{\partial r_n}{\partial y}\right) + \frac{\partial}{\partial z}\left(K_h\frac{\partial r_n}{\partial z}\right) + \emptyset_r \quad (29)$$

$$\frac{\partial \pi'}{\partial t} = -\frac{R\pi_0}{c_v\rho_0\theta_0}\left(\frac{\partial \rho_0\theta_0 u}{\partial x} + \frac{\partial \rho_0\theta_0 v}{\partial y} + \frac{\partial \rho_0\theta_0 w}{\partial z}\right) \quad (30)$$

Where u, v, and w are velocities in the x, y, and z dimensions, θ is potential temperature, π is the total Exner function, and r_r is the water mixing ratio. Equations (25-27) are the Navier-Stokes equations of motion in three spatial dimensions. Equation (28) is the thermodynamic equation. Equation (29) is the water species mixing ratio continuity equation (eight such equations, one for each hydrometeor type: cloud droplets, rain, ice, snow, aggregates, graupel, hail, and drizzle). Lastly, Equation (30) is the mass continuity equation. RAMS supplements these equations with parameterizations for turbulent diffusion, solar and terrestrial radiation, moist processes (including the formation and interaction of clouds and precipitating liquid and ice hydrometeors, sensible and latent heat exchange between the atmosphere), multiple soil layer, vegetation canopy, surface water, kinematic effects of terrain, and cumulus convection (Peilke 1992).

RAMS is fundamentally a limited-area model, but may be configured to cover an area as large as a planetary hemisphere for simulating mesoscale and large scale atmospheric systems. No lower limit exists to the domain size or to the mesh cell size of the model's finite difference grid, as microscale phenomena, such as tornadoes and boundary layer eddies, as well as sub-microscale turbulent flow over buildings and in a wind tunnel, have been simulated (http://rams.atmos.colostate.edu/rams-description.html). The schemes used for the present research follow this paragraph. The Mahrer and Pielke (1997) scheme was used for radiation. The Mahrer and Pielke scheme is the simplest and by far the least expensive computationally; accounting for water vapor. The Chen and Cotton (1983) scheme account for condensate in the atmosphere, but not whether it is cloud water, rain, or ice. This is a major limitation. The Harrington (1997) parameterization accounts for each form of condensate (cloud water, rain, pristine ice, snow, aggregates, graupel, and hail) as well as water vapor, and even utilizes information on ice crystal habit. In addition, the scheme adds upper atmospheric levels for

radiation computation for cases where the model domain does not extend up to at least 25 km (roughly the height of the ionosphere). This is the most sophisticated parameterization and is the most computationally expensive scheme, although work is planned to improve its performance. The Mahrer Pielke scheme was used here since it is the least computationally expensive, and because simulations are performed on warm precipitation in which ice is not be a major factor.

Sea surface temperature (SST) is derived from the Smith and Reynolds Extended Reconstruction Sea Surface Temperature (ERSST v3b, Smith and Reynolds 2003; Smith et al. 2008). These data contain SST information defined on each model grid, for multiple times and are defined globally on a latitude-longitude grid with climatological values for each month of the year at 2^{o} resolution. SST values for the simulations in this study were constant, since all experiments were performed during July 2007.

The convective parameterization is used to vertically redistribute heat and moisture in a grid column when the model generates a region which is superadiabatic or convectively unstable and when the horizontal grid resolution is too coarse for the model to develop its own convective circulation. Ideally, resolving a convective circulation would require at least a few grid cells to horizontally span an updraft, which for deep convection would normally require the horizontal cell size to be less than 1 or 2 km. Coarser resolution than this would make realization of sufficiently strong vertical motion difficult or impossible to adequately bring about the required vertical exchange of heat and moisture so as to convert the convective available potential energy into other forms. Thus, it is on coarser grids where a parameterized convective adjustment becomes necessary. Unfortunately, the convective parameterization schemes currently available assume the horizontal grid spacing be 20 km or greater. This means that a convective

parameterization may be activated on any grid of this resolution, but that at resolutions between about 2 and 20 km no adequate convective adjustment scheme exists. Here, the Kuo (1975) parameterization is used in Grid 1 for all experiments.

For grid 3, an explicit cloud microphysics scheme is used. The microphysics moisture complexity was set to the highest level. This level incorporates all categories of water in the atmosphere (cloud water, rain water, pristine ice crystals, snow, aggregates, graupel and hail); the module includes the precipitation process (Walko et al., 1995). An analysis "nudging" type of four-dimensional data assimilation (4DDA) scheme in which the model fields can be nudged toward pressure reanalysis data attained from The National Center for Environmental Prediction (NCEP) is used in RAMS. The 4DDA scheme, as mentioned, is a simple nudging-type scheme where an additional term is added to the model prognostic equations. This term can be written as:

$$\frac{\partial \emptyset}{\partial t} = \frac{(\emptyset_{obs} - \emptyset_{m)}}{\tau}, \tag{31}$$

where ϕ represents the prognostic variables of u, v,θ, π, and r_r. τ is a timescale which controls the strength of the nudging term and varies in three dimensions. In RAMS, the timescale structure can be broken into the lateral boundary, the top boundary, and the domain interior. The final timescale for any grid point is the minimum of the three timescales.

The lateral boundaries use a parabolic function defined as:

$$\tau_{lat} = \tau_B \left[\left(\frac{(x-x_i)^2}{(x_I - x_B)^2}\right)\right] \tag{32}$$

where τ_{lat} is the nudging timescale for the lateral boundary regions, τ_B is the timescale specified for the actual boundary point, x_B is the x coordinate of the boundary point, and x_I is the x coordinate of the interior point where the lateral boundary timescale goes to infinity.

The top boundary condition is patterned after the Rayleigh friction absorbing layer (Tripoli and Cotton 1982; Durran 1983) in which a layer below the model top is forced back to an initially horizontally-homogeneous state in order to damp vertically-propagating gravity waves, reducing reflections from the model top. When the model is initialized with observational data, the absorbing layer is nudged to an inhomogeneous observed state. The associated timescale is a function of height:

$$\tau_{top} = \tau_T \left[\frac{(z - z_I)}{(z_T - z_I)}\right] \tag{33}$$

where τ_{top} is the nudging scale for the top boundary, τ_T is the timescale specified for the actual top boundary point, z_T is the height of the top boundary, and z_I is the height of the base of the nudging layer. In order for a simulation to be numerically stable, it is important to maintain a smooth transition of the nudging timescales across the nested grid boundaries. To ensure that this always occurs, the timescales are defined on the coarsest grid and interpolated to each of the nested grids.

Two different LCLU scenarios are configured for NYC based on land data from the National Land Cover Database (NLCD) for the year 2006 and used in the Land Ecosystem–Atmosphere Feedback (LEAF-3, Walko and Tremback 2005). The first configuration represents the LCLU specification in an urbanized NYC (City). This represents the present urban extension and land characteristics of NYC as observed by NLCD (Appendix Table App1). For the No City

LCLU, LEAF-3 is modified such that all urban grid cells are transformed into deciduous broadleaf forest grid cells. In order to match the location of each of the urban cells from NLCD data with the atmospheric model grid, a natural landmark was identified and specified in RAMS (i.e., Staten Island in this case); then the rest of the dataset is fitted to the surface configuration. This methodology results in a present LCLU configuration that closely resembles the current land development, land use, and urban sprawl mapping in NYC as shown in Fig. 15. The No-City case is presented in Fig. 16.

LEAF-3 is a sub model of RAMS that evaluates energy and water budgets at the surface of the Earth and between land atmosphere interactions for various land types. There are 30 different land and surface precipitation types, most of which are defined in the Biosphere Atmosphere Transfer Scheme (BATS) described by Dickinson et al. (1986). Multiple vegetation patches may be activated within each grid to represent the variation in surface vegetation. For urban regions, the leaf-area index and vegetation fractional coverage are minimized while the roughness length is increased, thereby representing the effects of the rough city surface. LEAF-3 is a representation of surface features including vegetation, soil, lakes and oceans, and snow cover and their influence on each other and on the atmosphere. LEAF-3 includes prognostic equations for soil temperature and moisture for multiple layers, vegetation temperature and surface water including dew and intercepted rainfall, snow cover mass and thermal energy for multiple layers, and temperature and water vapor mixing ratio of canopy air. Exchange terms in these equations include turbulent exchange, heat conduction, water diffusion, percolation in the snow cover and soil, longwave and shortwave radiative transfer, transpiration, and precipitation. The properties of LEAF-3 land classes are shown in the Appendix (Table App2).

From land data canopy net all-wave radiation balance (W m^{-2}), temperature (˚C), and albedo can be determined following Oke (1987). A brief description of the formulation to calculate the surface albedo is given.

The net solar radiation, R_s, at the given wavelength is given by

$$R_s = (1 - \sigma)(R_s\downarrow), \tag{34}$$

where σ is site albedo and $R_s\downarrow$ is the incoming solar radiation.

The albedo is defined as

$$\sigma = R_s\uparrow / R_s\downarrow, \tag{35}$$

where $R_s\uparrow$ is the reflected solar radiation.

A two-way interactive grid nesting capability in RAMS allows local fine mesh grids to resolve compact atmospheric systems, such as thunderstorms, while simultaneously modeling the large scale environment on a coarser grid. The present set of simulations contain three nested grids, one at 16 km, the second at 4 km , and the finest grid at 1 km horizontal grid spacing (Fig. 17). All three grids are centered at 40.8N/73.9W. Grid 1 covers a 500 km by 150 km area, grid 2 covers a 200 km by 100 km area, and grid 3 covers a 60 km by 60 km area. This includes NYC, and a large portion of Long Island. The eastern seaboard is also included in the grid. Grids 2 and 3 allow for high-resolution analysis of the NYC area. NYC land use data for the year 2006 is taken from the NLCD and ingested into the model grid. The 30 m resolution NLCD data represents the city with multiple land classes.

At time zero, NCEP reanalysis pressure-level data at 2.5^{o} x 2.5^{o} resolution is assimilated to initiate the simulation, and updated every 6 hours to provide boundary conditions for grid 1. The data includes boundary information for air temperature, geopotential height, relative humidity, specific humidity, and three components of velocity (u, v, and w) at 16 pressure levels ([1000, 925, 850, 700, 600, 500, 400, 300, 250, 150, 100, 70, 50, 30, 20, and 10 hPa] Kalnay et al. 1996). Dynamical downscaling is used here to provide smaller-scale information for grids 2 and 3 given the coarse resolution of the NCEP data. There are 35 vertical levels with variable grid spacing in each simulation, and the model top extended to approximately 26 km above ground level. The long time step is 30 s. The complete data ingestion/assimilation plan is shown in Fig. 18.

In order to determine the effect of PSD and LCLU on model results, 17 simulations were configured (Table 3). Five of the simulations are month long runs for July 2007. The first three simulations were all City cases; one with constant PSD values in which CCN was assigned an initial concentration of 200 cm^{-3} and GCCN were assigned an initial concentration of 20 cm^{-3} (NA1, This represents a "clean cloud" scenario), the second with PSD updates as they are available in the AERONET dataset (A1), and the third with constant CCN concentration of 3000 cm^{-3} and GCCN concentration of 20 cm^{-3},(NA1-high). The fourth and fifth simulations mirrored the first two for a No City LCLU (NA2) and (A2).

The next six simulations address a one day localized precipitation event (11 July 2007) under varying PSD and LCLU conditions, and six more simulations addressed a one day regional event (18 July 2007) under varying PSD and LCLU conditions. Each daily run endured for 24 hours. For these short runs, 12 hours of spin up is added. Test runs showed that spin up beyond

12 hours had no noticeable impact on model results. In summation, each localized and mesoscale event is tested under City and No City LCLU and is ingested with the following PSD scenarios: (a) the use of PSD data derived from radiation measurements from the CCNY based AERONET sunphotometer for the day of the event, (b) PSD ingestion for a day other than that of the event, also from the AERONET CCNY site, (c) the use of PSD data for the day of the event minus the coarse mode, and (d) the use of PSD data for the day of the event minus the coarse mode. This approach allows for analysis of the effect of varying the aerosol PSD and LCLU on the cloud-resolving model's simulated precipitation results. For daily events, total accumulated precipitation, instantaneous (from the previous time step) precipitation rate, cloud droplet concentration (CDC), and temperature results will be presented.

3.3.2 Input Data from AERONET

Observations show that aerosols may reduce and or enhance precipitation in cities (Kessler 1994; Jauregui and Romales 1996; Shepherd et al. 2002; Diem and Brown 2003; Ntelekos et al. 2009). Aerosol PSD can vary from day to day, exhibiting different profiles for clear and cloudy days. The next step in this research is to describe the PSD observations that will be ingested into RAMS. AERONET is a network of ground-based sunphotometer instruments (Fig. 19) that measure the intensity of sunlight and properties of atmospheric aerosols (http://aeronet.gsfc.nasa.gov). Any aerosols or gases between the sun and the photometer tend to decrease the solar intensity and the sunphotometer is capable of measuring these differences.

AERONET provides continuous cloud-screened observations resulting in the acquisition of spectral aerosol optical depth (AOD), precipitable water, and inversion aerosol products. Inversion products are retrieved from almucantar scans of radiance as a function of scattering angle, and include parameters such as aerosol volume size distribution, aerosol complex refractive index, single scattering albedo, and aerosol scattering phase function. Due to the passive nature of these radiometric measurements, all these products represent an average of the total aerosol column within the atmosphere.

Aerosol properties, including PSD, are retrieved via an automated inversion algorithm (Dubovik and King 2000; Otero 2003). AERONET PSD data for July 2007 was collected for the current research. During intense precipitation events, the sunphotometers are not usually running. This is why there are only 11 PSDs for July 2007 (Fig. 20). Since it did rain on 11 and 18 July 2007 (the dates of interest for this study) each case PSD data was retrieved for the latest times possible on 10 and 17 July 2007, respectively. AERONET PSDs are given as volume size distributions. These were converted to number concentrations for use in RAMS via the following equation:

$$\frac{dV}{d(\log r)} = V(r) * \frac{dN}{d(\log r)} \tag{36}$$

Where:

$$\frac{dN}{d(\log r)}$$

is the density number log-normal distribution needed in RAMS, and,

$$\frac{dV}{d(\log r)}$$

is the volume distribution obtained from AERONET for each radii (r). The volume of each CCN/GCCN (assumed spherical) is:

$$V(r) = \frac{4\pi}{3} * r^3 \tag{37}$$

Such that:

$$\frac{dN}{d(\log r)} = \frac{3}{4\pi r^3} * \frac{dV}{d(\log r)} \tag{38}$$

PSD retrievals are quality assured (version 2 and level 2 type) as specified by Holben et al. (2006). The version 2 AERONET algorithm determines the percentage of spherical particles required to give the best fit to the measured spectral sky radiance angular distribution (Eck et al. 2012). Comparisons of size distributions between in-flight and AERONET retrievals for smoke in South America, Southern Africa, and North America showed that the volume median diameters of the in situ versus the AERONET retrievals were often within ~0.01 μm of each other for all three regions (Reid et al. 2005).

For this research, PSD will be classified as *High Volume Fine Mode* (HVFM) or *High Volume Coarse Mode* (HVCM). The PSD for three sites is shown in Fig. 21. PSDs obtained for 10 July 2007 (HVFM) and 17 July 2007 (HVCM) over NYC, Cartel (45N/71W), and the Maryland Science Center (39N/76W) vary only in concentration. Particle concentration over Cartel is less than half the concentration over CCNY for both days. This is theorized to be an impact of the urban aerosols from NYC. For this study, only PSD data from the CCNY site was used for ingestion in RAMS. Although there is a decrease in aerosol concentration moving outward from the center of NYC, this is not a major issue for the current research because analyses are performed on small domains. Number concentrations and mean radii for fine and coarse modes for July 2007 are shown in Fig. 22 and Table 4. To run RAMS with updates, the following sequence was followed:

1) Put in the date and time duration between the aerosol updates.
2) Put in aerosol information, set RAMSIN to “MAKEVFILE” and run the executable.
3) Set RAMSIN to “INITIAL” and run executable.
4) When the run is completed, input the time info for the present aerosol update, and the run time duration until the next update.
5) Set RAMSIN to “HISTORY” and run executable.
6) Repeat steps 4 and 5 until all updates are completed.

Aerosol optical depth processing within AERONET includes the spectral de-convolution algorithm (SDA) described in O'Neill et al. (2003). This algorithm yields fine and coarse aerosol optical depths at a standard wavelength of 500 nm (from which FMF, the fine mode fraction to total aerosol optical depth can be computed). The advantage of the SDA is that it produces useful indicators of aerosol size discrimination at the frequency of extinction measurements. The key output products of the SDA are all computed at a reference wavelength of $\lambda = 500$ nm. These products include the AOD (τ_a, using the nomenclature of O'Neill et al. 2003), the spectral derivative of the AOD (α_{sd}), and the spectral derivative of α_{sd} (α_{sd}'). These parameters are employed in the SDA to compute the fine mode aerosol optical depth (τ_f), the spectral derivative of the fine mode aerosol optical depth (α_f), the spectral derivative of α_f (α'_f), the fine mode fraction ($\eta = \tau_f / \tau_a$) and the coarse mode optical depth ($\tau_c = \tau_a - \tau_f$).

The spectral derivatives α and α_f represent, respectively, (i) a generic Angstrom exponent containing information on the combined size contributions of fine and coarse mode aerosols and (ii) size information specific to the fine mode size distribution. Figure 23 shows the SDA products for 10 and 17 July 2007 (just prior to the extreme localized and mesoscale precipitation events of 11 and 18 July 2007 respectively). Prior to 11 July 2007, the fine mode fraction is 95%

which means that the coarse mode fraction is 5%. Preceding the 18 July 2007 event, the fine mode fraction was 79% and the coarse mode fraction was 21%.

3.3.3 Input data from NLCD

LCLU data is taken from NLCD for the year 2006. Shown in Fig. 24, NLCD is a multi-class land cover classification scheme that has been applied consistently across the conterminous US at a spatial resolution of 30 m. NLCD 2006 is based primarily on the classification of Landsat Enhanced Thematic Mapper+ (ETM+) circa 2006 satellite data (Fry et al. 2011) and serves as the definitive land cover database for the nation. There are 20 land classes, including three for the urban environment. Each land class contains information about its albedo, surface roughness, percent impervious surface, and percent tree canopy cover.

3.3.4 Satellite Data for Comparison

The Cloud-Aerosol Lidar and Infrared Pathfinder Satellite Observations (CALIPSO) satellite was launched on 28 April 2006 to study the impact of clouds and aerosols on the Earth's radiation budget and climate. It flies in formation with five other satellites in the international "A-Train" constellation for coincident Earth observations. CALIPSO comprises three instruments: the Cloud-Aerosol LIdar with Orthogonal Polarization (CALIOP), the Imaging

Infrared Radiometer (IIR), and the Wide Field Camera (WFC). CALIPSO is a joint satellite mission between NASA and the French Agency, CNES.

NASA's Geostationary Operational Environmental Satellites (GOES) circle the Earth in geosynchronous orbit. From 35,800 km above the earth, GOES satellites provide half-hourly observations of earth-emitted and reflected radiation from which atmospheric temperature, winds, moisture and cloud cover can be derived. GOES data is distributed by the National Environmental Satellite and Information Service (NESDIS) to a variety of operational and research centers including NWS, the Department of Defense, and the global research community. Since they stay above a fixed spot on the Earth's surface, they provide constant watch over atmospheric triggers for severe weather conditions such as tornadoes, flash floods, and hurricanes.

CALIPSO provides insight into the role that clouds and atmospheric aerosols play in regulating weather, climate, and air quality of the earth. CALIPSO combines active LIDAR with passive infrared and visible imagers to probe the vertical structure and properties of thin clouds and aerosols over the globe. CALIPSO and CloudSat (a satellite that uses radar to measure the vertical structure of clouds) are highly complementary and together provide 3D perspectives of how clouds and aerosols form, evolve, and affect weather and climate. GOES satellites provide continuous monitoring necessary for intensive data analysis. Data from CALIPSO and GOES-12 will be used to determine if the model is capturing features of the precipitation events mentioned previously.

Table 2: NWS Surface Weather Stations for investigation.

Station	LAT	LON
Mineola	40.75	-73.64
Oceanside	40.64	-73.64
Wantaugh	40.68	-73.51
Bound Brook	40.57	-74.54
Canistear RSVR	41.12	-74.47
Canoe Brook	40.78	-74.31
Essex Fells	40.82	-74.28
Harrison	40.75	-74.16
New Brunswick	40.49	-74.45
New Milford	40.94	-74.02
Plainfield	40.63	-74.41
JFK	40.64	-73.78
Central Park	40.77	-73.97
EWR	40.69	-74.18
LGA	40.77	-73.87
Secaucus	40.79	-74.06

Table 3: Experimental matrix for daily runs.

Run	LCLU	Aerosol	Storm Dynamics	Research Questions
A1	City	11 Updates	----------	a,c
NA1	City	300 CCN 20 GCCN	----------	a,c
NA1-High	City	3000 CCN 20 GCCN	----------	a,c
A2	No City	11 Updates	----------	b,c
NA2	No City	300 CCN 20 GCCN	----------	b,c
1	City	HVFM (11 July 2007)	Localized (11 July)	a,c
2	City	HVFM (11 July 2007)	Mesoscale (18 July)	a
3	City	HVCM (18 July 2007)	Mesoscale (18 July)	a,c
4	City	HVCM (18 July 2007)	Localized (11 July)	a
5	No City	HVFM (11 July 2007)	Localized (11 July)	b,c
6	No City	HVCM (18 July 2007)	Localized (11 July)	b,c
7	City	11 July minus coarse mode	Localized (11 July)	a,c
8	City	11 July minus fine mode	Localized (11 July)	a
9	No City	HVCM (18 July 2007)	Mesoscale (18 July)	b,c
10	No City	HVCM (18 July 2007)	Mesoscale (18 July)	b,c
11	City	18 July minus fine mode	Mesoscale (18 July)	b,c
12	City	18 July minus coarse mode	Mesoscale (18 July)	b,c

Table 4: Aerosol PSD updates in RAMS. Star (*) denotes that AERONET PSD data corresponds to the latest reading for these dates.

Date	Fine Mode Modal Radius (e-6)	Fine Mode (dN/(dlogr))	Fine Mode (#/cm^{-3})	Coarse Mode Modal Radius (e-6)	Coarse Mode (dN/(dlogr))	Coarse Mode (#/cm^{-3})	Time of Update
7/1	.148240	.62719	62.7	1.30150	1.04895	104.9	0
7/2	.1944922	.27771	27.8	5.05963	.04012	4	24hrs
7/6	.148240	2.90104	290	2.24034	1.16398	116.4	120hrs
7/7	.148240	3.41406	341.4	2.93934	.53605	53.6	144hrs
7/9	.1129879	13.786	1378.6	5.05963	.75814	75.8	192hrs
7/10	.1944922	5.23792	523.8	2.93934	2.5169	251.7	216hrs
7/10*	.255174	3.785	378.5	3.85642	2.23181	223.2	240hrs
7/12	.148240	.43911	439.1	2.93934	.36800	36.8	264hrs
7/17*	.148240	.417153	417.2	6.63825	.82380	82.4	408hrs
7/26	.148240	4.66479	466.5	5.05963	.29726	29.7	600hrs
7/28	.148240	2.90119	290.1	5.05963	.28848	28.8	648hrs

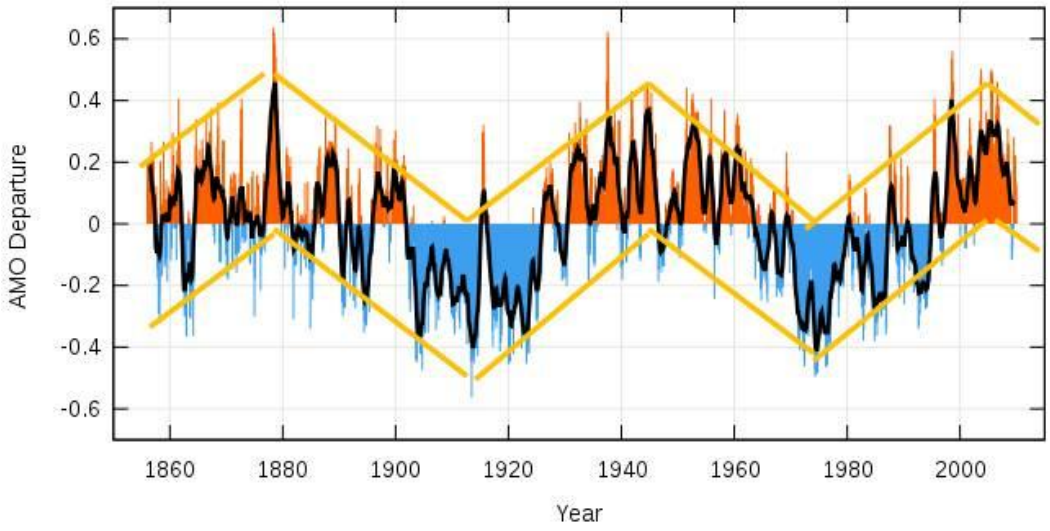

Fig. 8: AMO anomalies from 1850 to 2009. The cycle length is approximately 62 years with maxima around 1878, 1943 and 2004, and minima around 1912 and 1974.

Source: http://www.appinsys.com/GlobalWarming

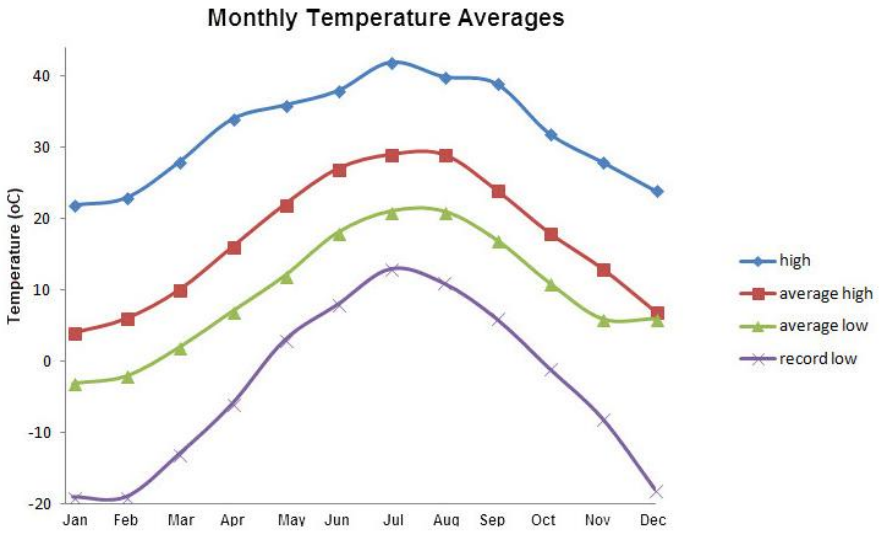

Fig. 9: Monthly temperature averages for NYC based on data spanning from 1895 to 2012. maximum temperature of 41°C has been recorded in July, while the minimum recorded temperature was -26 °C found in February. Source: www.weather.com

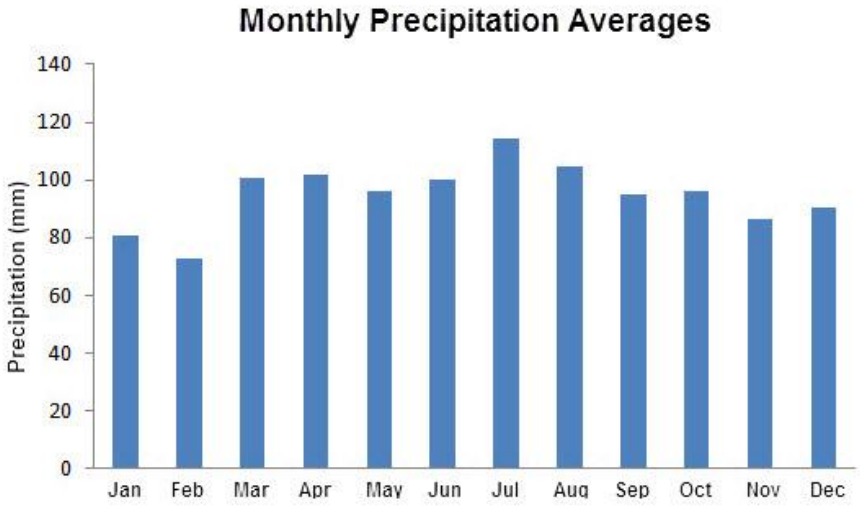

Fig. 10: Monthly precipitation averages for NYC based on data spanning from 1895 to 2012.

Source: www.weather.com

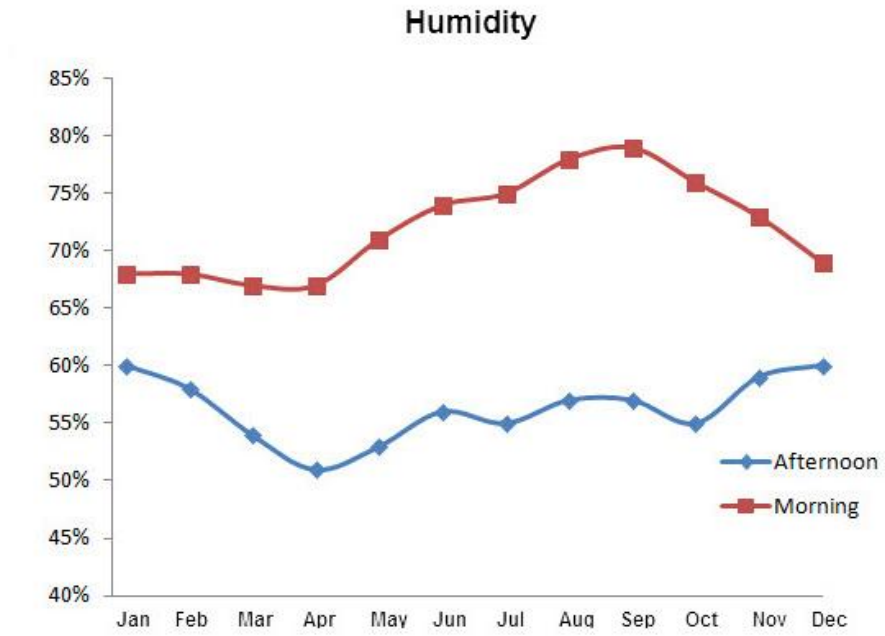

Fig. 11: Monthly humidity averages for NYC based on data spanning from 1895 to 2012.

Source: www.noaa.gov

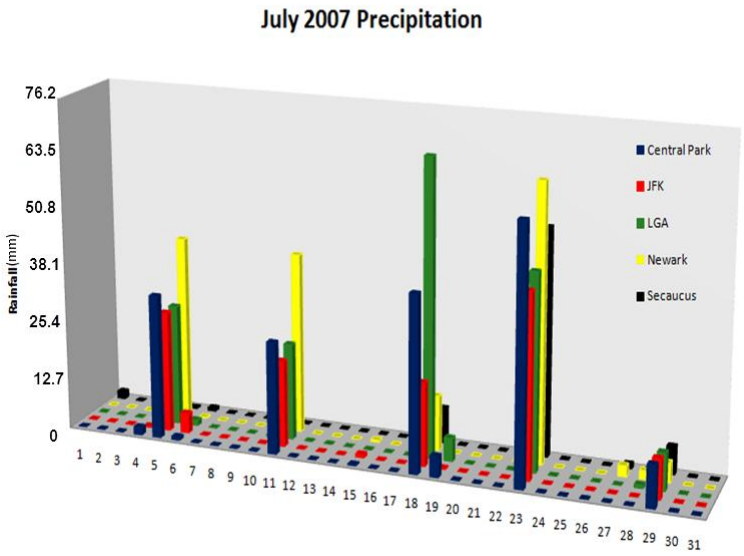

Fig. 12: Precipitation over the NYC/NJ region for the month of July 2007 from NWS Stations.

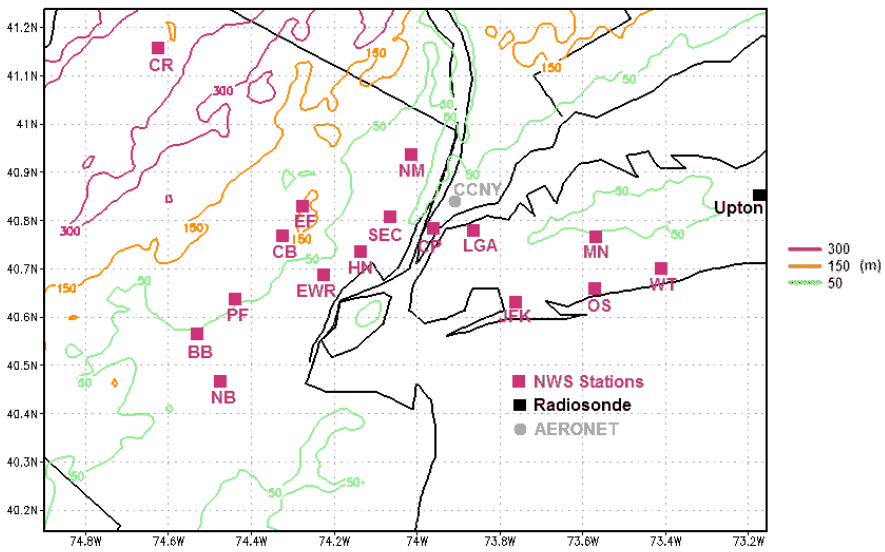

Fig. 13: Data sites over topography. NWS surface stations are shown as purple squares, the Upton radiosonde site is shown as a black square, and the CCNY AERONET site is shown as a grey circle.

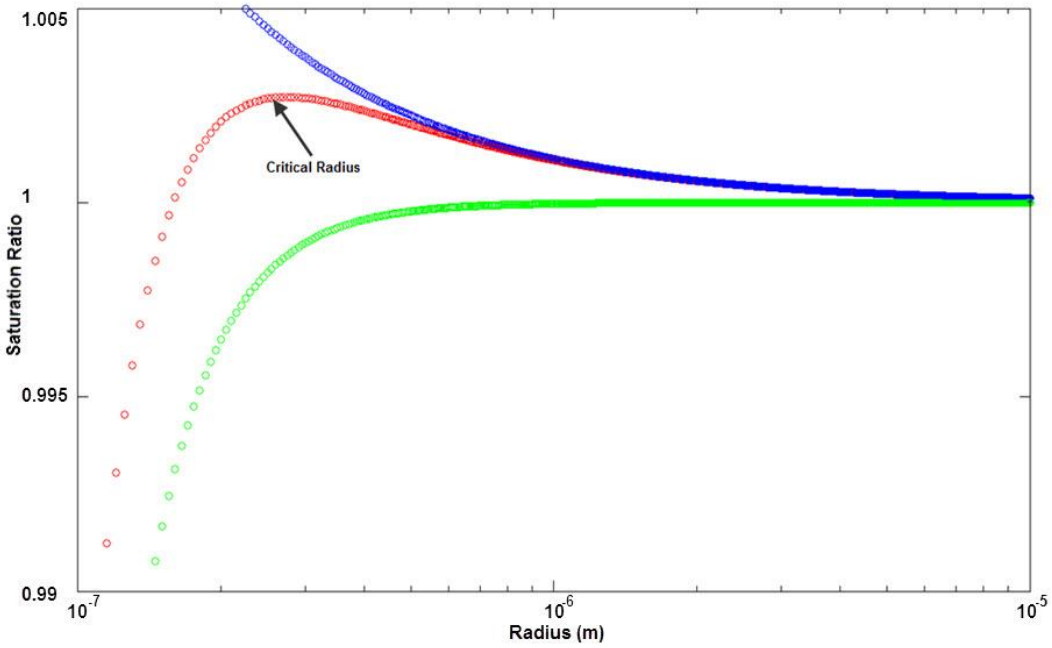

Fig. 14: Kohler effect for a water droplet.

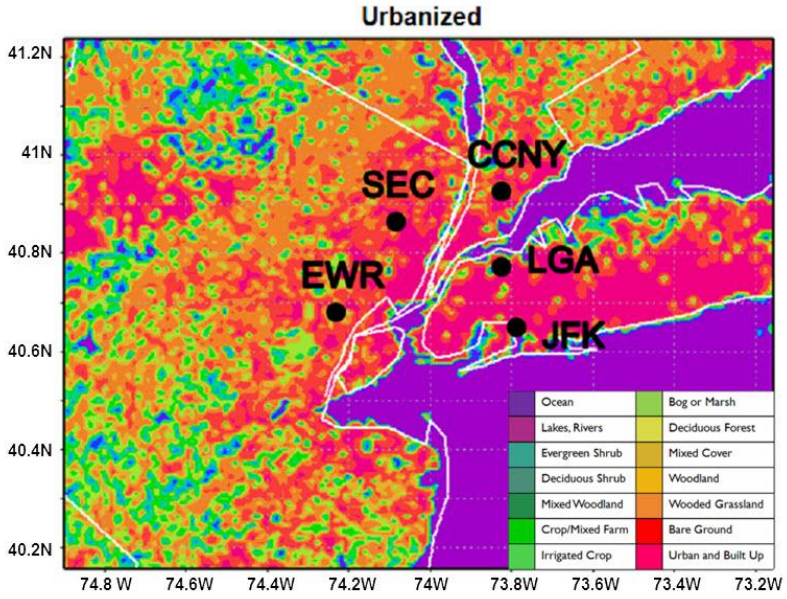

Fig. 15: LCLU for the "City" representation, including 14 classes transformed from NLCD to RAMS.

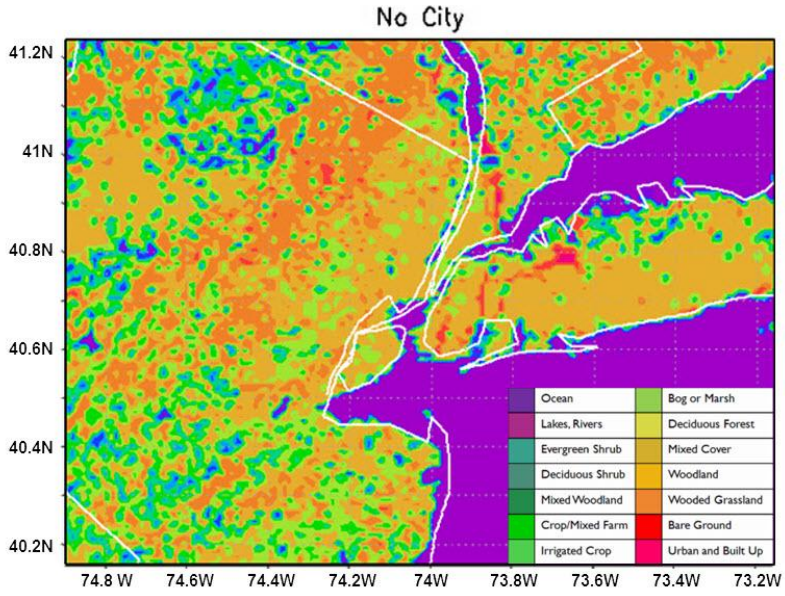

Fig. 16: LCLU for the "No City" representation in RAMS, in which all urban grid cells are replaced by the deciduous broadleaf land type.

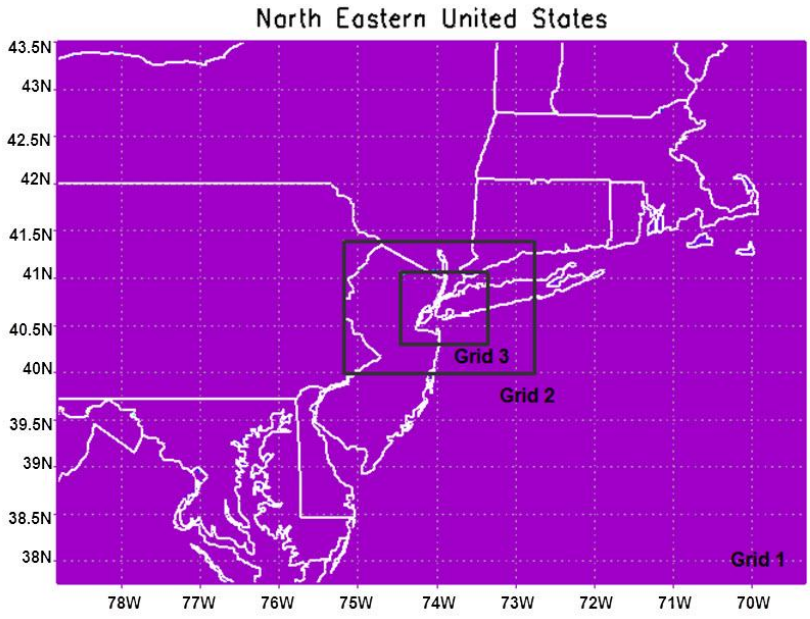

Fig. 17: RAMS grid setup.

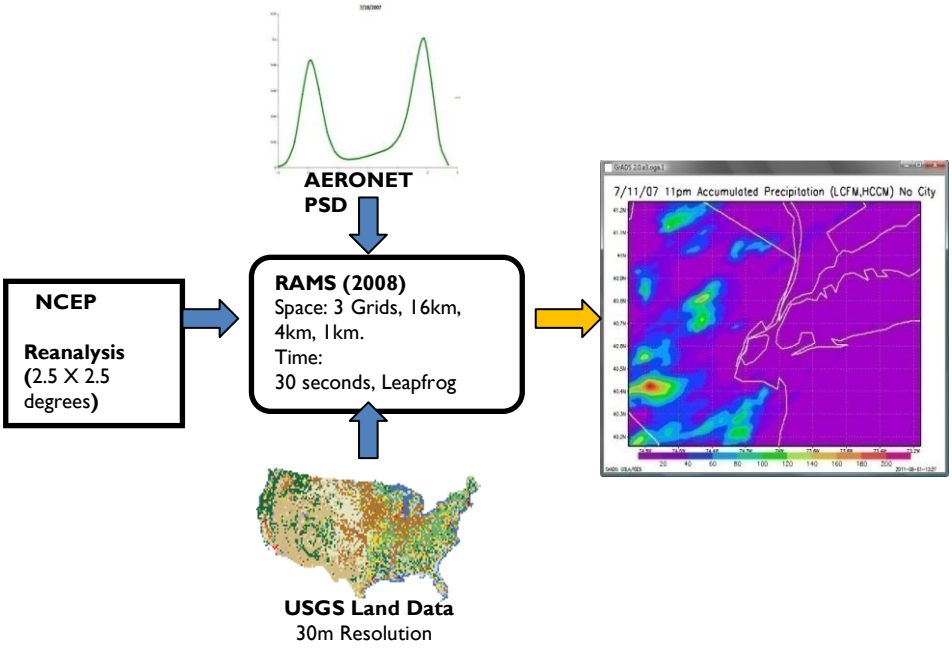

Fig. 18: Experimental setup. Data acquisition, assimilation, and results.

Fig. 19: A sunphotomer used to obtain aerosol particle size distribution.

(Source:http://www.nasa.gov/vision/earth/everydaylife/aeronet.html)

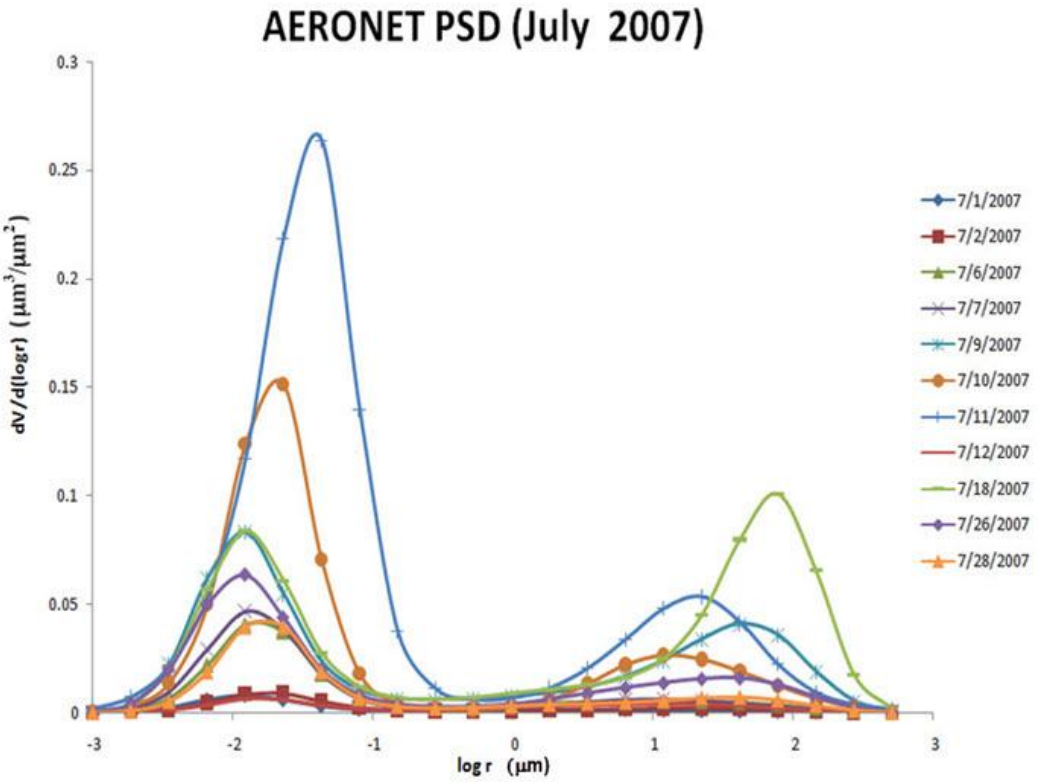

Fig. 20: PSD over CCNY AERONET station (40.83N,73.94W) for July 2007.

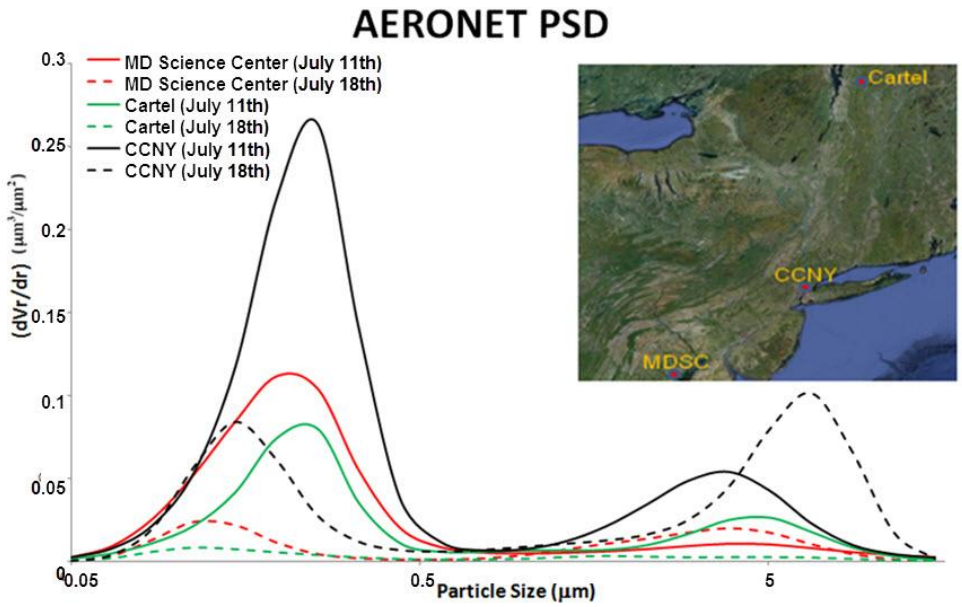

Fig. 21: PSD for three sites for 10 July 2007 (HVFM) and 17 July 2007 (HVCM) over NYC, Cartel (45N/71W) and the Maryland Science Center (39N/76W).

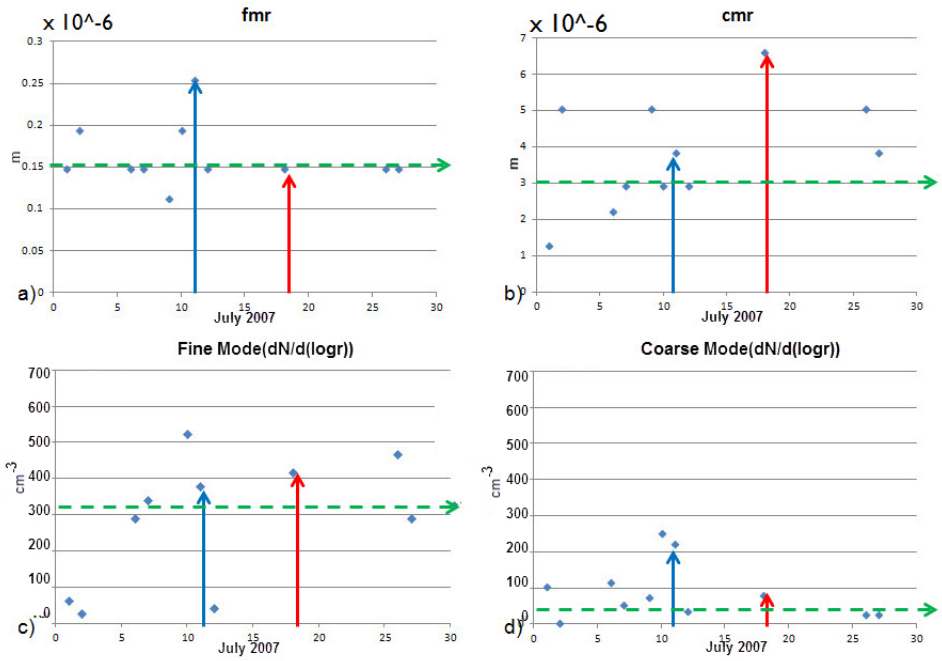

Fig. 22: Graphical representation of Table 5. Blue arrows highlight 10 July 2007 data, red arrows highlight 17 July 2007 data. The dashed green arrows represent the average used for cases in which PSD was not updated. a) Fine mode modal radius. b) Coarse mode modal radius. c) Fine mode number concentration. d) Coarse mode number concentration.

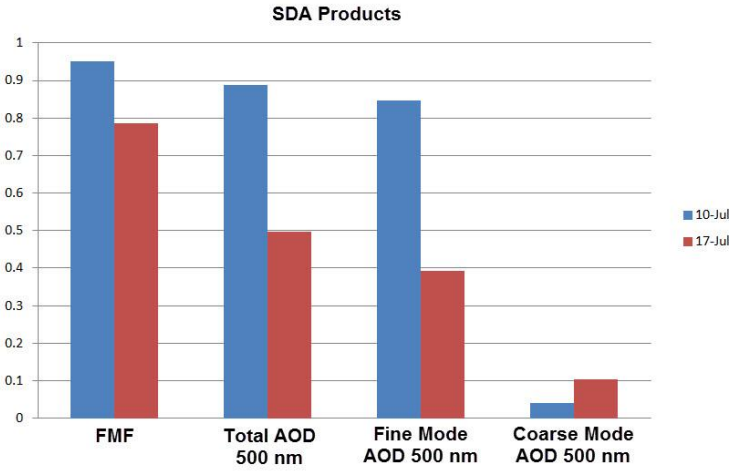

Fig. 23: SDA products for 10 July 2007 and 17 July 2007. Data attained from the CCNY AERONET site.

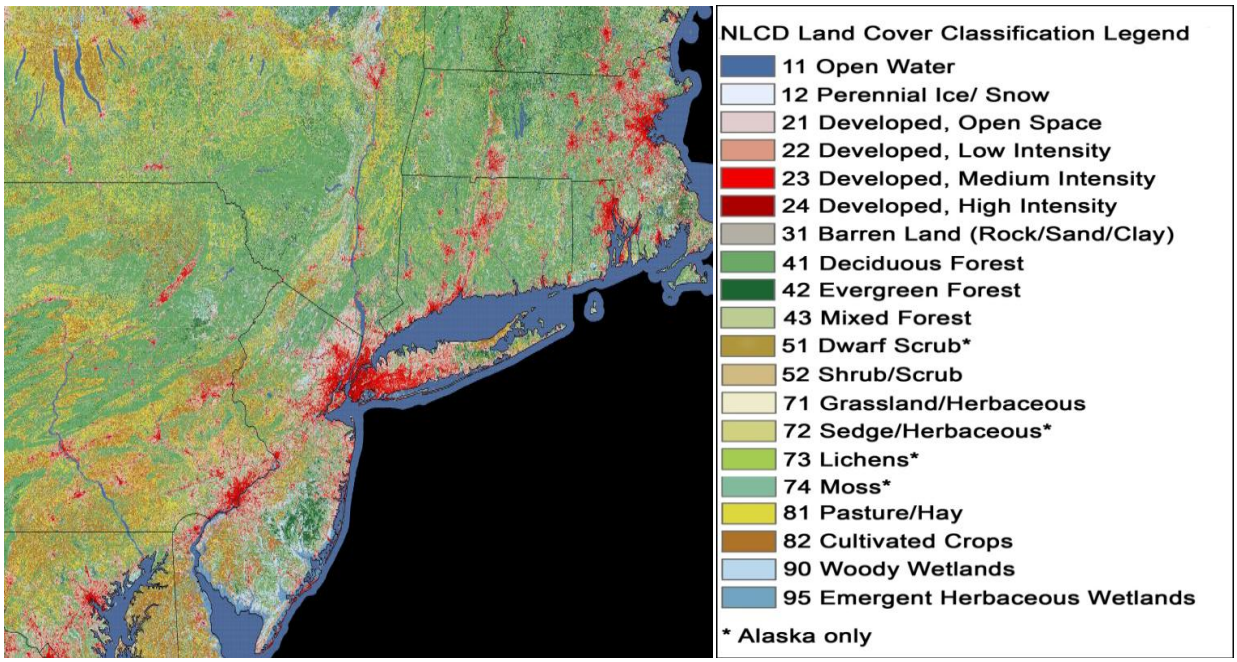

Fig. 24: LCLU over the North East Region.

Chapter 4

Impacts of Aerosol PSD, LCLU Changes, and Storm Dynamics on Precipitation in NYC

4.1 Idealized Microphysics Results

A numerical code was written to solve the droplet growth equations described in Chapter 3 using a finite differencing method. Ambient conditions were assumed as follows. Temperature was 10°C, and atmospheric pressure was 1000 hPa, with a constant updraft of 1 m s^{-1}. Figure 25 shows results for predicting droplet growth by condensation alone. When the saturation ratio is held at unity, water droplet size remains constant. Increased saturation ratio increases the rate of condensation growth. It is noteworthy that for each value of the saturation ratio from 1 to 1.10, particle sizes exceed the critical Aitkens radius for growth by collision and coalescence $\left(r* = \right.$ *3ba.* Aerosols smaller will grow only by condensation. Smaller particles do not coalesce as effectively as larger particles and thus do not reach rain drop size, suppressing precipitation as a result. As is the case in nature, growth contributions from collision and coalescence must be included to account for droplets that reach rain drop size of 2 mm in 20 min or less.

PSD evolution for both idealized unimodal and bimodal distributions are shown in Fig 26. These plots show how groups of droplets grow in relation to one another. Droplet growth by collision and coalescence over time for varying collection efficiency generated through numerical simulation of Eqs. (19-24) is displayed in Fig. 27. As *E* increases, droplet growth rate increases substantially. Figure 28 is attained by modeling condensation along with collision and

coalescence. Four parameters were varied, including updraft velocity (when set to zero, this is considered the no convection case), supersaturation level, time at which collision and coalescence begins, and collection efficiency. Although 16 such simulations were run, the results for the four runs with collision and coalescence beginning five min after condensation growth begins are shown here. Droplets grow faster with higher supersaturation level and collection efficiency.

Condensation alone requires long periods of time for droplets to develop into rainfall. With collision and coalescence added, the time for droplets to reach raindrop size decreases. Results from this study show that a droplet with initial radius 0.1 micron, supersaturation of 1.01, updraft velocity of 1 m s^{-1} and collection efficiency of 0.2 will reach rain drop size of 2 mm in approximately 16 min. Observations have shown that droplets may grow from 0.1 micron to rain drop size in 20 to 25 min (Rogers and Yau 1989) with 2 m s^{-1} updraft velocity, standard atmospheric pressure, and 5^{o}C air temperature.

This simplified parametric study shows how important it is for droplets to be large enough to efficiently coalesce. GCCN have the propensity to rain out of a cloud quicker than the smaller CCN. This suggests that PSDs with a dominant fine mode (11 July 2007) will delay the initiation of precipitation, whereas PSDs with a dominate coarse mode (18 July 2007) will hasten the initiation of precipitation. In order to attain a better understanding of the effects of aerosols on microphysics and precipitation in NYC, it will be necessary to ingest observed AERONET PSD into RAMS simulations.

4.2 Synoptic Overview for Daily Events

Surface pressure maps over the region show that rainfall on 11 July 2007 was not due to frontal movement (Fig. 29), and is considered localized because of this fact. High pressure southeast of NYC and a north to south low pressure trough through the city (dashed line) produces an observed southeasterly onshore flow. The 18 July 2007 storm forms in a different way. Surface pressure maps indicate that a warm front traveled northward from southern NJ to NYC amidst overall weak pressure gradients, and became a stationary front over the city, remaining over for six hours and producing southeasterly flow over the area. Regional storms require a warm moist layer that extends up from the surface through a deep atmospheric layer (Fig. 30). A stationary front is a non-moving boundary between two different air masses. Long periods of localized torrential rainfall are common. The 11 and 18 July 2007 upper air plots at 700 hPa both show southwesterly flow over NYC (Fig. 31 and 32).

The CAPE is the positive buoyancy of an air parcel and is an indicator of atmospheric instability, which makes it very valuable in predicting severe weather. A CAPE value greater than zero indicates instability and the possibility of localized thunderstorms. The CAPE values on 11 and 18 July 2007 were 890 and 132.1 J kg^{-1}, respectively (Figs. 33 and 34). The closest radiosonde site to NYC is located 90 km away at Upton, New York (40.87N/72.89W). These CAPE values suggest that the effect of the local environment on precipitation was greater on 11 July 2007 than it was for 18 July 2007. Skew-T plots (also in Figs. 33 and 34) show a warm atmosphere from 1000 to 150 hPa for both 11 and 18 July 2007. In the dry layer from 900 to 300 hPa (above the surface saturated layer), dew point temps are significantly lower than air

temperature values. The (warmer) moister atmosphere on 18 July 2007 (up to 150 hPa) indicates higher available precipitable water content.

4.3 RAMS Validation

Before running detailed sensitivity studies based on variation of PSD, the author must first determine if incorporation of PSD data from AERONET into RAMS yields improvement in total accumulated precipitation prediction. Following the approach of Comarazamy et al. (2006), this set of experiments involves ingestion of PSD data for month long July 2007 simulations. Two month long simulations for July 2007 were run using RAMS. The first simulation was run with zero PSD updates, using a constant value of 300 cm^{-3} for CCN and 20 cm^{-3} GCCN throughout (simulation NA1), for the second simulation PSD was updated every time new AERONET data was available during the month, amounting to 11 updates (simulation A1). Each PSD update required the simulation be stopped at the time of ingestion. Modal values for CCN and GCCN concentrations and particle radii were then amended in the microphysics module, and the simulation was continued via history restart.

Results presented in Table 5 show improved prediction for simulation A1 at 12 of 16 sites. Over NYC (CP 40.80N/73.90W) and the four closest sites (JFK 40.65N/73.78W, LGA 40.78N/73.87W, SEC 40.78N/74.07N, and EWR 40.73N/74.18W), monthly precipitation errors range from 0.03-3.1% compared to 2.5-21.7% for simulation A1. Positive/negative biases are indicated by +/- signs. In general, the model has a tendency to over predict precipitation totals. For 10 of 16 sites, modeled totals are greater than observed totals. Specific to each of the

simulations, NA1 over predicts total accumulated precipitation for eight of 16 sites, while A1 over predicts at five of 16 sites. NA1 produces more rainfall than A1 for 10 of 16 sites.

Root Mean Square Error (RMSE) plots in Fig. 35 show that simulation A1 is a better predictor of total accumulated precipitation than simulation NA1. These results are statistically significant to a 99.7% confidence level (See Appendix for more information). Both runs capture the five precipitation events of July 2007 within 12 hours of their occurrences, consistent with findings by Comarazamy et al. (2006) in which results for a seven day simulation show that RAMS exhibits rain events lagging six to 12 hours after having occurred in observations, mostly due to the assimilation of large scale boundary conditions from NCEP. Figures 36 and 37 show total accumulated precipitation evolution at the CP site for 4-6 and 18 July 2007, respectively. Observations (solid lines) compared with RAMS results (dotted lines) show that while RAMS results lag observations by six to 12 hours, accumulated precipitation totals have errors less than 20% in each case. Figures 38 and 39 show that the model captures minimum and maximum temperatures to within 1^{o}C for CP for 11 and 18 July 2007. Results for daily events (presented in Section 4.4) will also show that the model shows agreement with observed wind directions from previously discussed surface pressure maps and radiosonde Skew-T plots.

In general, after the validation was performed and analyzed for the A1 and NA1 results and acknowledging that there are slight tendencies for over prediction of maximum temperatures, it is considered that RAMS complemented with observed PSD data and digital LCLU maps is an adequate tool to perform the proposed study on PSD and LCLU changes in NYC. A simulation with PSD ingestion (A1) leads to better matches with observations for 12 of 16 sites over the NYC/NJ region than the constant value case (NA1). A third month long simulation (NA1-high) with the constant fine mode number concentration of 3000 cm^{-3}, and

constant coarse mode number concentration of 20 cm^{-3} was run. Results show that precipitation totals were reduced over the region for NA1-high, evidence that high concentrations of fine mode aerosols can suppress precipitation.

4.4 Aerosol PSD

The effect of ingesting observed AERONET PSD on month-long RAMS simulations was presented in the previous section. From here, the focus will be on the effects of PSD on the 11 and 18 July 2007 daily precipitation events. Runs 1 and 3 are used to determine how well the model captures the NWS observed precipitation totals, winds, and spatial orientation of the two events. Runs 2 and 4-12 are used to determine deviation from Runs 1 and 3, thus determining the effects of ingesting/ assimilating different PSDs/LCLU on the storms (Runs 5, 6, 11, and 12 are No City runs, and will be discussed in section 4.5).

4.4.1 11 July 2007 City

The weak UHI shown in the temperature plots of Fig. 40 will not initiate storms over NYC, but warmer NJ does experience precipitation in higher-elevation locations. The falling rain cools surface temps. Precipitation rate by hour for Run 1 in Fig. 41 shows that simulated southerly synoptic flows turn into a southeasterly sea breeze over coastal NJ. The 50 m hill in that area triggers moderate precipitation, with an area of precipitation at a similar rate on the

western boundary in the 300 m height area. By 11 am EDT, southerly flow from the seabreeze shifts to an organized southeasterly flow over eastern NJ, and isolated regions of light convective precipitation formed over the region, with moderate precipitation occurring in NJ. By 12 pm, the southeasterly flow has extended westward over NJ, and precipitation areas have slightly strengthened. By 4 pm, flow diverges around NYC and half a cyclonic-vortex forms downwind over NJ. Southeasterly winds prevail for Runs 1 and 4. The most intense precipitation occurs west of 74W, in northern and southern NJ. The centers of the two major storm cells do not move far from their origins. Results for total accumulated precipitation (Fig. 42) show that maximum precipitation occurs downwind of NYC, which research by Huff and Changnon (1973) and Bornstein and Lin (2000) suggests is an effect of enhanced convection downwind of the city. Also noted here is that intense precipitation initiates in locations with topographical heights of 50 m and over (Northern NJ). Land heights range from 0 m above sea level near the shores to 400 m above sea level in northern NJ. In Manhattan, Staten Island, Brooklyn, Queens, and the Bronx, heights range from 0 m to 150 m.

CALIPSO data for 11 July 2007 shows type of aerosol, cloud base heights, droplet phase, and type of atmospheric particle (Fig. 43). Over NYC, fine mode (pollution) aerosols dominate, but there are also clean-marine and dust aerosols present, supporting the theory that local storms over urban regions can be affected by ingestion of mass amounts of fine mode aerosols. There is large ice content in clouds over 12 km height. Plots show high pollution presence in low level clouds. Comparison of Run 1 precipitation rate with cloud optical depth (COD), and long-wave (LW) flux (both from the GOES-12 satellite) are compared in Fig. 44. From 1 pm through 4 pm, there is correlation between the locations of the highest RAMS precipitation rates and the highest GOES-12 LW fluxes. It is more difficult to relate the RAMS precipitation rate to GOES-12

COD, as the signal is lost over much of the region (denoted by the color black). This lost signal could be due to the fact that rain is falling over these locations during these times, making COD measurement impossible. Early on, (1 and 2 pm) the black pattern tends to the western part of the region, which would be in agreement with the location of highest precipitation rates and accumulated precipitation totals.

Figure 45 shows total accumulated precipitation for Runs 1 and 4. Plots for Run 1 minus Run 4 by hour (Fig. 46) show precipitation enhancement (denoted by negative values) due to the presence of bigger GCCN particles over most of the region, including the northwestern storm (41N/74.6W). There is some suppression (denoted by positive values) at the center of the southwestern storm (40.25N/74.15W). The outer perimeter of both storms experience suppression, attributed to the fact that GCCN particles rain out faster and require more time for newly activated particles to grow after the initial rain out while CCN delay rain due to their smaller size. Higher regions experience enhancement because they are closer to atmospheric conditions favorable for precipitation to occur. The cooler air at heights above 300 m may accelerate droplet growth, which leads to enhancement.

Analysis of cloud base height (CBH) differences for CCNY, the northern NJ storm, and the southern NJ storm (Fig. 47) show that CBH does not differ for the first 12 hours of simulation. In each of the three cases, there is initial positive difference, which means that Run 1 exhibited higher CBH than did Run 4. During the most intense rainfall, 11 am – 1 pm there is a negative difference for each of the three sites, indicating that Run 4 exhibited higher CBH than Run 1. These results suggest that HVFM PSD delays the occurrence of the intense precipitation, and that the HVCM PSD causes the cloud to rain out early, allowing for newly activated CCN to

rise higher in Run 4 before they grow to overcome cloud updrafts. This pushes CBH higher between 1100 and 1300 EDT.

In order to further zoom in on PSD impacts on precipitation, an experiment in which the coarse mode was removed from the 11 July PSD (Run 7) and one with the fine mode removed from the 11 July PSD (Run 8) were simulated. Results in Fig. 48 show that inclusion of both the fine and coarse mode (Fig.48a) leads to the highest precipitation totals. When one mode is subtracted, there is increased total precipitation with the presence of only coarse mode aerosols (Fig. 48d) and reduced precipitation with the presence of only fine mode aerosols (Fig. 48c).

The vertical wind for each of these cases is plotted in Fig. 49. Extreme vertical wind speeds are shown to occur west of 74W, coincident with the locations of the most intense and highest accumulations of rainfall. Also noted is the presence of more intense downdrafts at 4pm with the presence of coarse particles (Runs 1, 4, and 8). Vertical temperature/wind plots along the 40.85N latitude at the start of the intense rainfall (11 am) for this sensitivity study are shown in Fig. 50. Plots in Figures 50a,b, and d show evidence of a warming trend going from east to west (UHI), with reduced temperatures near the Hudson and East Rivers. There is high convection between 75W and 74.5W. Figure 50c, which shows the result for Run 7, shows more uniform heating (except near 74.2W), high convection 75W and 74.5W, and added convection at 73.4W.

4.4.2 18 July 2007 City

High precipitation rates are shown at various locations around region (Fig. 51). A sea breeze front moves inland at 0900 EDT. By 1200 EDT, upslope flow towards the top of the high topography in the NW intensifies its local precipitation rates. Winds begin to become less organized by 1300 EDT as an UHI induces convergence over NYC and initiates a storm. Temperature plots at 2 m above the surface (Fig. 52) show development of the UHI forms between 1100 and 1200 EDT. By 1400 EDT, the storm has passed the city and split into two parts; one section over the LI Sound and the other over NJ.

Total accumulated precipitation plots in Fig. 53 show high totals both north of NYC and in NJ (west of 74W). There is light precipitation over the region until 1000 EDT, when flow coming from a seabreeze onto the land shifts to an organized easterly flow over eastern NJ, and isolated regions of convective precipitation formed over NJ. By 1300 EDT, the easterly flow is less organized over NJ, and heavy precipitation forms along the 41N latitude, and over eastern NJ below the 40.4N latitude. There is less rain over NYC than in other areas.

Satellite data for 18 July 2007 shows that clean marine aerosols dominate, while pollution and dust are less evident. This is consistent with the idea that larger scale storms will be less affected by anthropogenic aerosols than localized storms. At lower levels (1 km and below), water phase clouds are shown. From 6-10 km, mixed phase clouds are shown (Fig. 54). Above 12 km, there are clouds in the ice phase shown. Comparison of Run 3 precipitation rate with COD and LW flux is presented in Fig. 55. At 1300 EDT, there is some correlation between the locations of the highest RAMS precipitation rates and the highest GOES-12 LW fluxes but it is

more difficult to match features at later times. COD plots have a high amount of lost signal for all times except 1600 EDT (when the precipitation rate reduces). This could be because 18 July 2007 was a larger scale storm, and thus less organized on the local level.

The total accumulated precipitation for Runs 3 and 2 are shown in Fig. 56. Precipitation difference by hour for Run 3 minus Run 2 in (Fig. 57) shows suppression with the presence of HVFM PSD south of the 40.6N latitude (low topography) denoted here by red (although there is a substantial enhancement pocket at 74.8W). Along 40.9N from 74.8W to 73.2W, there is both suppression and enhancement, with Precipitation clearly decreased due to HVFM over Manhattan (40.8N/73.9W), but increased over the Hudson and East Rivers. Western LI (Brooklyn and Queens) also experience suppression, while eastern Long Island experiences enhancement. While topography may play a role here, it is less evident than in the 11 July 2007 storm.

Results for18 July 2007 PSD sensitivity cases in Fig. 58 show that inclusion of both the fine and coarse mode (Fig. 58a) yields the highest precipitation totals while there is enhanced total precipitation with the presence of only GCCN (Fig. 58d), and reduced precipitation with only CCN (Fig. 58c). Vertical wind is plotted in Fig. 59. Lower vertical wind speeds are found for these cases than for11 July 2007 cases. Vertical temperature/wind plots along the 40.85N latitude at the beginning of the high intensity rainfall (1100 EDT) are shown in Fig. 60. Results for Fig. 60a,b, and d show evidence of reduced low level temperature between 74.2W and 73.8W. There is high convection between 75W and 74.6W, and between 73.8W and 73.6W. Figure 60c shows a warmer low level between 74.2W and 73.8W and more intense convection between the 73.8W and 73.6W longitudes in Run 9.

Vertical liquid water mixing ratio (LWMR) plots through the 40.9N latitude (chosen because this latitude exhibited high storm activity for both 11 and 18 July 2007) show the effect of the city on the convection. Of interest in Runs 1 and 4 (Figs. 61a and 61b) is the steady increase of convective activity occurring west of NYC (73.9W). HVFM of Run 1 (Fig. 61a) enhances LWMR from 3-6 km in comparison to HVCM of Run 4 (Fig. 61b), as evidenced by LWMR difference plot of Fig. 61c. Below the 3 km mark the LWMR is higher in Run 4. LWMR plots for Run 3 and Run 2 (Figs. 61d-61f) show evidence of HVCM in Run 3 dominating from ground level up to 6 km. This is further evidence that smaller particles travel higher before growing to a size where they can overcome updrafts and rain out of the cloud. For large scale storms, PSD variation has a smaller effect on LWMR.

Comparison of total precipitation for NWS observations and City simulation results are shown in Table 6. For both Run 1 and Run 3, total precipitation matches observations well in most areas, particularly over NYC, LGA, EWR, SEC, and JFK. Run 4 predicts well along Long Island, but does not capture amounts over Manhattan and NJ. Run 2 over predicts total precipitation for all monitored sites except Mineola (MN) and LGA. These misses for Runs 2 and 4 are attributed to idealized PSD ingestion.

It is now possible to answer the major research question and two of three sub research questions:

How do aerosols affect precipitation in an urban environment?

According to research conducted in Atlanta, Phoenix, Mexico City, Puerto Rico, and NYC, (Shepherd et al. 2002; Jauregui and Romales 1996; Kessler 1994; Diem and Brown 2003; Comarazamy et al 2006; and Ntelekos et al. 2009) aerosols can increase or decrease precipitation in urban environments. In agreement with the studies mentioned above, the current work shows

that precipitation increases are likely to be caused by the presence of GCCN while reduction is caused by the presence of a high concentration of CCN.

(a) How does variation of aerosol particle size distribution affect total precipitation?

Results from studies over Puerto Rico (Comarazamy et al. 2006) suggest that variation of PSD affects total precipitation in urban environments. RAMS results for NYC (in the present study) show that precipitation forecasting is improved when observed PSDs are ingested over the region. For 12 of 16 sites, runs with ingested PSDs show reduced error. Over NYC (CP) and the four closest sites (JFK, LGA, SEC, and EWR), errors range from 0.03-3.1% compared with a 2.5-21.7% error range for the no ingestion case.

RMSE plots for accumulated precipitation show that simulations with PSD ingestion predict more accurately than simulations with no PSD ingestion. Further, two different daily precipitation events were investigated via RAMS to study aerosol effects in local and mesoscale precipitation events. For both storms, HVFM and HVCM PSDs were ingested into RAMS. Results show suppression of precipitation over NYC. HVCM acted to enhance accumulated precipitation totals over the area for the localized and mesoscale cases. Precipitation response due to aerosol varied depending upon location of maximum convection. Specific to Runs 1 and 4 (statistically significant to a confidence level of 98.2%), precipitation is enhanced at the center of the NJ storms, while reduced on the storm perimeter. For Runs 2 and 3 (statistically significant to a confidence level of 70.0%), there is a spatial precipitation shift in NJ, and reduced precipitation over NYC.

PSD variation alters precipitation patterns and totals. Results show that HVFM PSD suppresses precipitation, while HVCM PSD enhances accumulated precipitation totals. Spatial

precipitation patterns also change. These PSD effects are attributed to hastened/reduced rates of autoconversion due to the presence of higher volumes of GCCN/CCN (reduced GCCN number concentration can result in increased GCCN volume when the modal radii is large as is the case in 18 July 2007), which enhances/impedes droplet coalescence rates, in agreement with work by Rosenfeld 2000, Comarazamy et al. 2006, and Rosenfeld et al. 2008.

(c) Can urban precipitation forecasts be improved?

In summary, results suggest that modeled precipitation results are closer to NWS observations when PSD obtained from AERONET is ingested, and that precipitation amounts and spatial patterns are sensitive to PSD variations. Assimilation of observed PSD data improves total precipitation results in localized and synoptic precipitation events, as shown when comparing Runs 1 and 3 with NWS observations. The answer to fundamental question b will be given in the next section.

4.5 PSD and LCLU

With the objective of responding to the fundamental question of the role of the city in enhancing/suppressing precipitation in an aerosol rich environment, two more month-long simulations for July 2007 were run under No City LCLU conditions. All urban grid cells were replaced with the deciduous broadleaf land classification. One simulation was run with zero PSD

updates with a constant value for CCN (300 cm^{-3}) and GCCN (20 cm^{-3}) throughout (simulation NA2), while the other simulation PSD was updated 11 times (simulation A2).

RMSE plots between NWS total daily precipitation observations and NA1, A1, A2, and NA2 are shown in Fig. 62. The spatial plots (top) are attained via interpolation of error at the closest grid point to the model errors. The bar graph (bottom) is representative of actual RMSE values for each simulation over 16 sites. Results for all month-long simulations in Table 7 show that the accuracy of total precipitation compared with observations is reduced for the A2 and NA2 scenarios. For 11 of 16 sites, the A1 scenario outperforms all other month long simulations. The two No City simulations (A2 and NA2) capture the five precipitation events of July 2007 within 12 hours of their occurrences, consistent with the City simulations (A1, NA1 and NA1-high).

4.5.1 11 July 2007 No City

New Run 5 is used to determine the effects of varying LCLU on the localized precipitation event (Run 1) while new Run 6 is used to determine the effects of LCLU and PSD. Model results show that Runs 5 and 6 produce more precipitation between the 40.4N and 40.9N latitudes and also extends further east than Runs 1 and 4 (Fig. 63). Although removal of the city does not increase totals by more than a few mm over NYC and along LI, the further eastward extension of major precipitation over the region is indication of the LCLU impacting precipitation. With the presence of the city (Runs 1 and 4), heavy precipitation is pushed

westward, it is less scattered, and more intense. Although the surface roughness parameter for the City LCLU is higher than the No City roughness, the wind must penetrate deeper inland to initiate precipitation. The city is forcing this precipitation further downwind consistent with previous reports by Bornstein and Lin (2000). Replacing HVFM PSD (Run 5) with HVCM PSD (Run 6) results in precipitation enhancement due to the presence of a greater volume of GCCN. Precipitation differences for Run 1 minus Run 5 (Fig. 64) show suppression due to the presence of the city (indicated by the color blue) over most of the region except at locations of maximum precipitation (near storms at 40.25N/74.15W and 41N/74.6W) (Also shown in Table 8).

Vertical wind plots in Fig. 65 shows evidence of stronger convection west of NYC for city runs than no city runs from 1300 - 1400 EDT. After the first rain out, Runs 1 and 4 take longer to recover and produce more rain. As a result of this delayed development of rainfall due to the presence of the city, strengthened convection over NJ from 1500 – 1600 EDT for Runs 5 and 6 is shown. Vertical temperature/wind plots along the 40.85N latitude at the beginning of the high intensity rainfall (1100 EDT) are shown in Fig. 66. Results for Figs. 66a,b, and d show evidence of reduced low level temperatures for the No City. There is also reduced convection intensity between 75W and 74.6W.

Analysis of CBH differences calculated for Run 1 minus Run 5 for CCNY, the northern NJ storm, and the southern NJ storm (Fig. 67) show that CBH does not differ for the first 12 hours of simulation. The impact of LCLU variation becomes evident at 0800 EDT. In each of the three cases, there is an initial positive difference, (Run 1 exhibited higher CBHs than did Run 3). During the most intense rainfall (1100 – 1300 EDT) there is a negative difference for each of the three sites, indicating that Run 1 exhibited higher CBH than Run 5. These results suggest that the presence of the city adds convection, which pushes CBH higher between these times. CDC for

the two storms at three different times is plotted in Fig. 68. Precipitation rates (Fig. 69) increase faster in Runs 3 and 4 for both storms. In the southern storm, Runs 5 and 6 experience the highest precipitation rates (80 – 110 mm/h), while values for Runs 1,4,7, and 8 experience a broader range (from 1- 130 mm/h)The northwestern storm shows negligible CDC until 1 pm for all simulations, while the southwestern storm initiates at 0900 EDT. The southwestern storm also has higher CDC for No City cases (Runs 5 and 6) than most other simulations except Run 1.

Turbulent kinetic energy (TKE) is the mean kinetic energy per unit mass associated with eddies in turbulent flow. Physically, TKE is characterized by measured root-mean-square (RMS) velocity fluctuations. Generally, the TKE can be defined as the mean of the turbulence normal stresses:

$$\mathrm{TKE} = \frac{1}{2}\left(\overline{(u_1')^2} + \overline{(u_2')^2} + \overline{(u_3')^2}\right) \tag{39}$$

Plots in Fig. 70 show differences in the temporal evolution of TKE at 0 m, 1000 m, and 2000 m during intense rainfall (1100 -1400 EDT) across the region for City (Run 1) minus No City (Runs 5 and 6) cases. Figure 70a corresponds to Run 1 minus Run 5, while Fig. 70b corresponds to Run 1 minus Run 6. Initially, TKE differences for both Run 1 minus Run 5 and Run 1 minus Run 6 show positive differences over the surface of NJ (denoted by red), and negative differences (denoted by blue) east of 74 W, corresponding with the location of NYC. At 1200 EDT, the TKE differences for both columns begin to increase eastward, showing higher values over NYC by 1400 EDT. These plots are evidence that the city LCLU increases TKE over the course of the precipitation event. Alternating the HVFM (Run 5) with HVCM (Run 6) shows reduced TKE differences across the region from 1200 -1400 EDT. The exception is the southwest corner of the domain (40.4N, -74.4W) at 1400 EDT. This is attributed to increased accumulated precipitation totals at this location for Run 1, previously shown in Fig. 63a. As the

elevation increases, maximum positive differences are found further west. It would be expected that NYC would experience higher TKE differences since it is highly urbanized. This anomaly where the highest TKE exists over NJ is attributed to warmer temperatures west of 74W.

4.5.2 18 July 2007 No City

Run 9 is the observed PSD case, and Run 10 corresponds to the case with the PSD of 11 July 2007. Reduced precipitation over the center of the domain is shown with the inclusion of the city, regardless of PSD (Fig. 71). Runs 9 and 10 produce more precipitation along Long Island than Runs 3 and 2 (Fig. 72). Runs 9 and 10 are used to determine the effects of varying PSD and LCLU on the mesoscale storm (Run 3). Vertical wind plots for both City and No City cases are shown in Fig. 73. Plots do not show large differences in convection between City and No City cases. This lends support to the argument that vertical convection is more affected by LCLU changes for a localized precipitation event than a mesoscale event. Vertical temperature/wind plots along the 40.85N latitude at the start of the high intensity rainfall (1100 EDT) for this sensitivity study are shown in Fig. 74. Results for Figs. 74c and d, show evidence of reduced low level temperatures between 74.2W and 73.4W for No City cases. This corresponds to the location of NYC. There is also reduced low level convection intensity between 75W and 74.6W, and 73.8W and 73.4W.

CDC for 40.83N/7.95W at three different times is plotted in Fig. 75. Precipitation rates for all mesoscale simulations are shown in Fig. 76. The No City cases (Runs 9 and 10) initially have higher precipitation rates than the City cases (Runs 2,3,11, and 12) at 1100 EDT, but City

cases have much higher rates by 1300 EDT due to the fact that the urban environment must be first heated to produce the increased convection necessary to induce higher precipitation rates.

Analysis of the previous experiments gives us a greater understanding of the role of aerosol PSD and LCLU on precipitation on the urban environment of NYC. Revisiting the fundamental research questions to answer the second:

> (b) How does the combination of land cover, land use (LCLU) and PSD affect precipitation totals and amounts?

Results show that while the runs with City LCLU and PSD updates matches observations best, LCLU variation impacts model results more than PSD variation. Deviation from observations are more evident in No City cases than in City cases. Accuracy increases with the inclusion of PSD updates, reducing errors from as much as 50% or higher (Run 5 and 6) to less than 5% (Run 1). Analysis of CBH differences calculated for Run 1 minus Run 5 for CCNY, the northern NJ storm, and the southern NJ storm show that CBH does not differ for the first 12 hours of simulation. The impact of LCLU variation becomes evident at 1000 EDT. In each of the three cases, there is an initial negative difference (0500 - 0600 EDT), which means that Run 5 exhibited higher CBH than did Run 1. Between 0800 and 1100 EDT, there is a positive difference trend for the three sites, indicating that Run 1 exhibited higher CBH than Run 5. The added convection from the city pushes the CBH up to 500 m higher for all three sites later in the run (1200-1400 EDT). These results suggest that the presence of the city impacts precipitation by pushing aerosols higher into the atmosphere via added convection and modified surface to atmosphere interactions that occur once the surface is warmed.

Using the method of factor separation (Stein and Alpert 1993), it is possible to determine the individual contributions of PSD and LCLU on precipitation. For *n* number of factors (two in this case), 2^n simulations are necessary (at least four in this case). For July 2007 monthly simulations over 16 sites (Fig. 77), results show that removal of the city and PSD updates weighs heaviest on precipitation results (nearly two fold over the simulation with City and PSD updates, average of 103% increase). Removal of the city with PSD updates has the second highest impact on precipitation, with nine of 16 sites showing increases (average of 7% over all sites). Lastly, City with no PSD updates shows increases at five of 16 locations (average of -18% over all sites). These results support the suggestion that LCLU is dominant in impacting precipitation over and near NYC, with PSD variation effects being secondary, but also important in producing rainfall.

Results for the present study agree with the urban effects synthesis based on the ideas of Bornstein (2011) but created by Grimmond (2011) and Shepherd (2011) in Fig. 7. Wind, UHI, and convergence/divergence primarily affect storm formation and path, while aerosol ingestion impacts storms after dynamic effects have set the stage for precipitation to occur via modification of cloud microphysics. When calm conditions combine with a strong UHI and convergence into the city, a precipitation maximum will occur over the urban center because convection will be highest where temperature is warmest (18 July 2007 at 1300 EDT). When strong winds combine with divergence upwind of the city and convergence downwind, precipitation will be diverted around the city; with maximum precipitation amounts resident in lateral and downwind convergence zones (18 July 2007 at times after 1300 EDT). When weak regional winds are present during a UHI and flow converges downwind of the urban boundary, the maximum precipitation will be advected to the downwind urban edge (11 July 2007).

Table 5: Total accumulated monthly precipitation validation for July2007 (underlined values are representative of improvements, red/blue values represent positive/negative bias).

	July 2007 NWS	July 2007 (NA1)	July 2007 (A1)
Mineola	218	147	120
Oceanside	110	125	115
Wantaugh	84	115	85
Bound Brook	120	180	120
Canistear RSVR	112	160	153
Canoe Brook	223	193	150
Essex Fells	194	177	156
Harrison	163	155	164
New Brunswick	141	149	137
New Milford	183	120	125
Plainfield	139	148	150
JFK	134	131	134
Central Park	175	150	177
EWR	170	179	171
LGA	180	168	180
Secaucus	81	98	83

Table 6: Daily precipitation comparison for RAMS and observations (Runs 1 and 3). (underlined values are representative of improvements, red/blue values represent positive/negative bias).

	7/11 NWS	7/11 Run1	7/11 Run 4	7/18 NWS	7/18 Run 3	7/18 Run 2
Mineola	11.4	1.6	10	97.0	36	18
Oceanside	11.9	20	10	0	3	21
Wantaugh	4.8	5	16	17.8	20	14
Bound Brook	0	0	3	3.6	23	26
Canistear RSVR	0	30	43	24.4	41	50
Canoe Brook	0	0	4	10.2	32	20
Essex Fells	44.7	20	20	0	46	53
Harrison	50.3	19	10	15.0	23	40
New Brunswick	0	3	10	1.27	10	9
New Milford	32.5	19	15	56.64	60	51
Plainfield	0	6	13	0	10	16
JFK	20	18	15	19.05	21	14
Central Park	26	20	8	40.39	41	38
EWR	43	45	47	12.7	25	25
LGA	23	10	7	67.82	60	27
Secaucus	0	2	17	8.13	10	14

Table 7: July2007 total monthly accumulated precipitation (underlined values are representative of improvements, red/blue values represent positive/negative bias).

	July 2007 NWS	July 2007 (NA2)	July 2007 Updates (A1)	July 2007 (NA1)	July 2007 (NA1-high)	July 2007 (A2)
Mineola	218	138	120	147	150	89
Oceanside	110	110	115	125	120	113
Wantaugh	84	111	85	115	100	106
Bound Brook	120	117	120	180	95	201
Canistear RSVR	112	190	153	160	70	157
Canoe Brook	223	193	150	193	98	167
Essex Fells	194	137	156	177	114	116
Harrison	163	164	164	155	100	110
New Brunswick	141	83	137	149	93	105
New Milford	183	88	125	120	96	79
Plainfield	139	110	150	148	50	175
JFK	134	109	134	131	125	111
Central Park	175	153	177	150	106	104
EWR	170	155	171	179	68	137
LGA	180	168	180	168	126	89
Secaucus	81	166	83	98	89	97

Table 8: Total daily precipitation for 11 July 2007 Runs (underlined values are representative of improvements, red/blue values represent positive/negative bias).

	NWS	Run 1	Run 4	Run 5	Run 6
Mineola	11	1.6	10	1	1
Oceanside	12	20	10	3	3
Wantaugh	5	5	16	2	2
Bound Brook	0	0	3	4	22
Canistear RSVR	0	30	43	47	34
Canoe Brook	0	0	4	22	35
Essex Fells	45	20	20	10	21
Harrison	50	19	10	8	12
New Brunswick	0	3	10	26	7
New Milford	33	19	15	5	3
Plainfield	0	6	13	1	6
JFK	20	18	15	3	3
Central Park	26	20	8	1	1
EWR	43	45	47	3	5
LGA	23	10	7	1	1
Secaucus	0	2	17	2	2

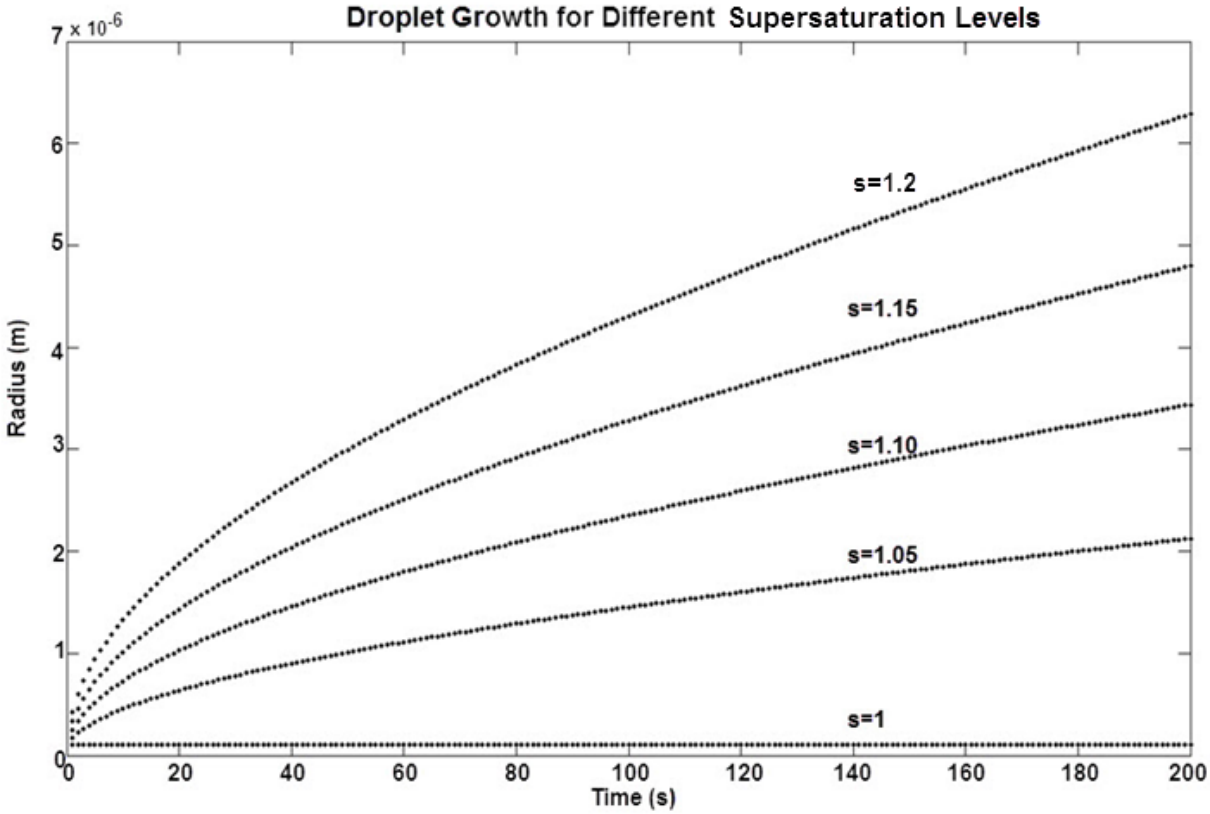

Fig. 25: Growth of droplets by diffusion only at different saturation levels.

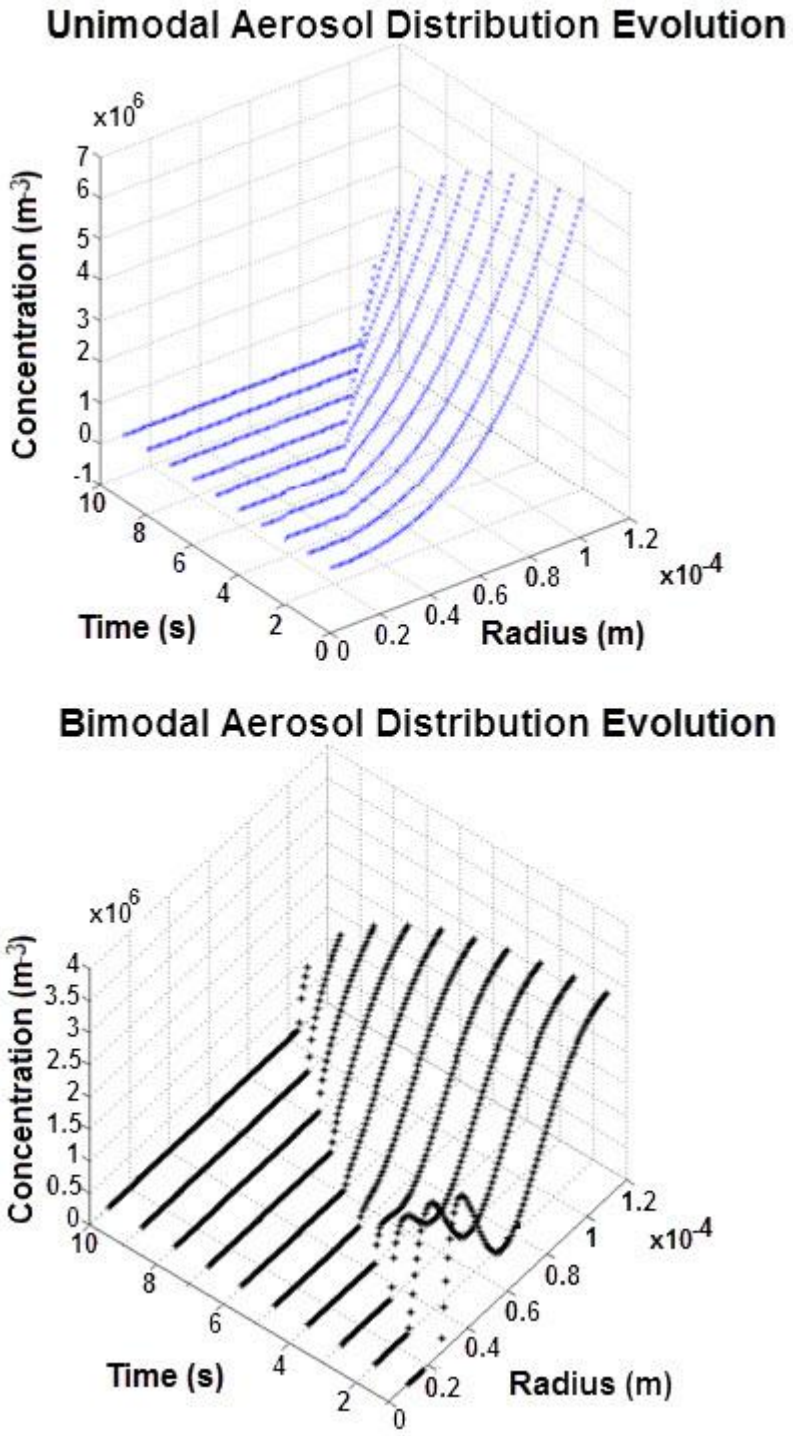

Fig. 26: PSD evolution over time for a unimodal distribution (top) and a bimodal distribution (bottom). Updraft velocity in both cases is 1 m s^{-1}

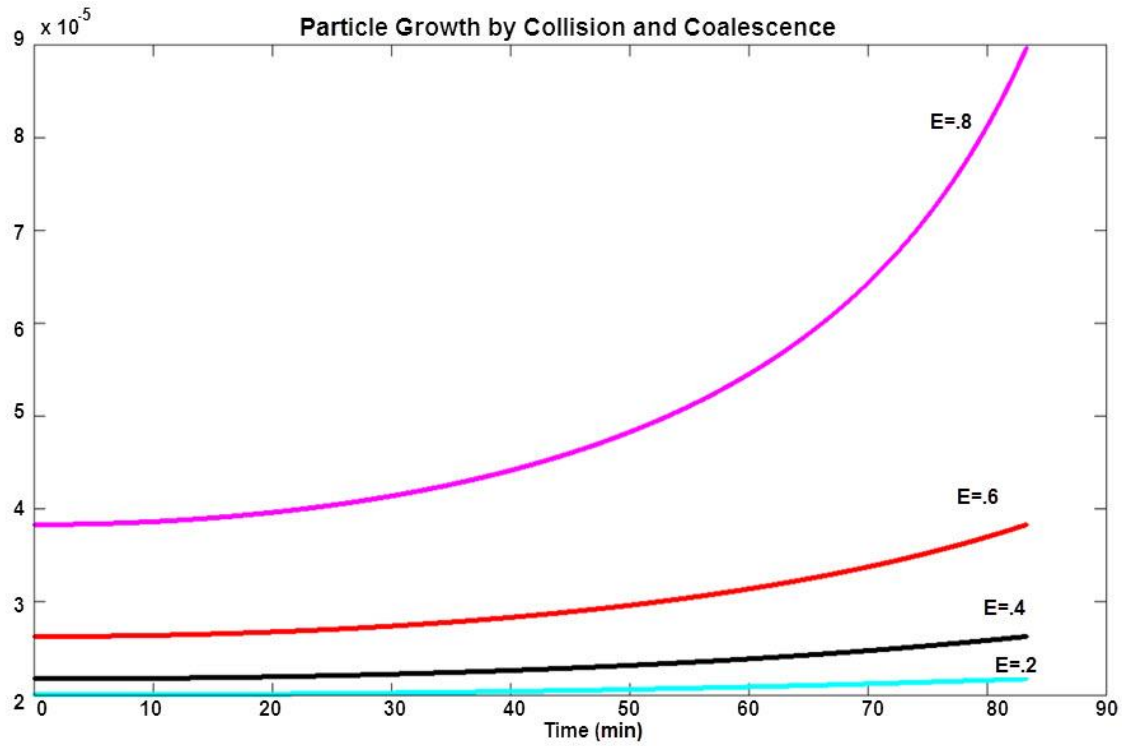

Fig. 27: Particle growth by collision and coalescence for different collection efficiencies (E).

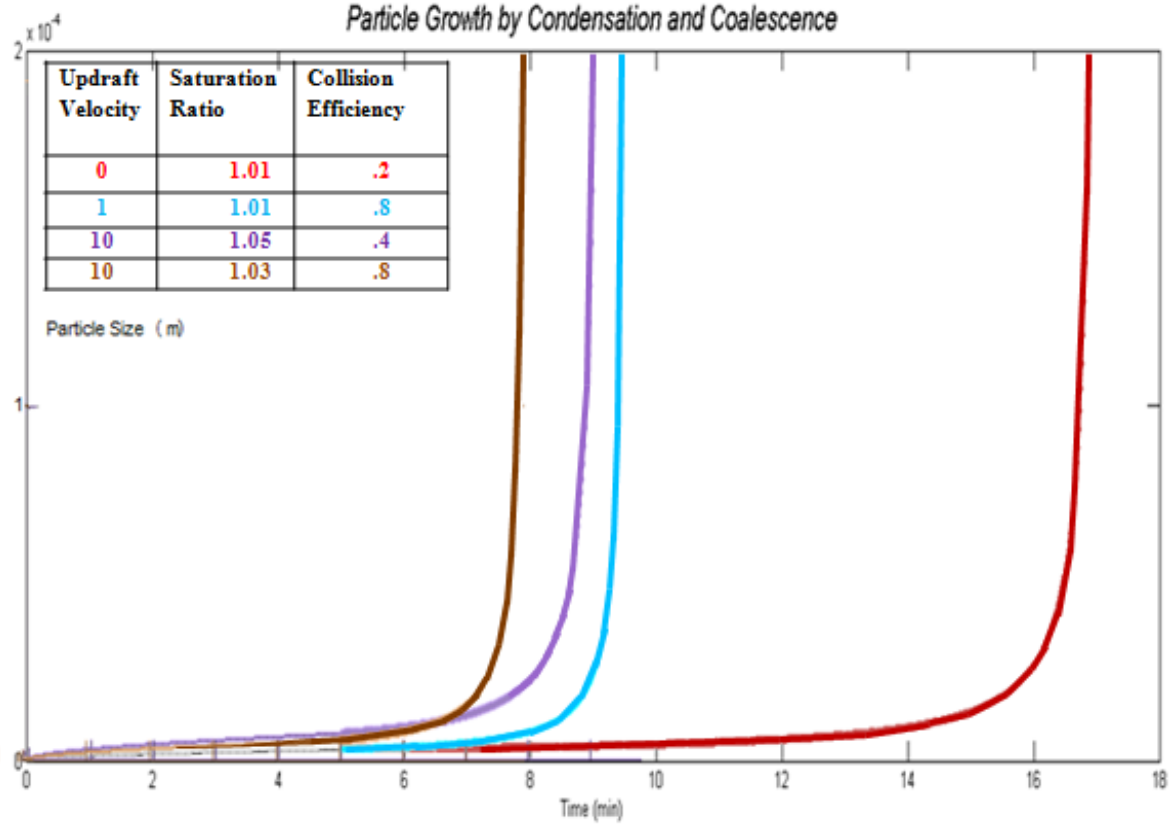

Fig. 28: Parametric study of particle growth by condensation and coalescence.

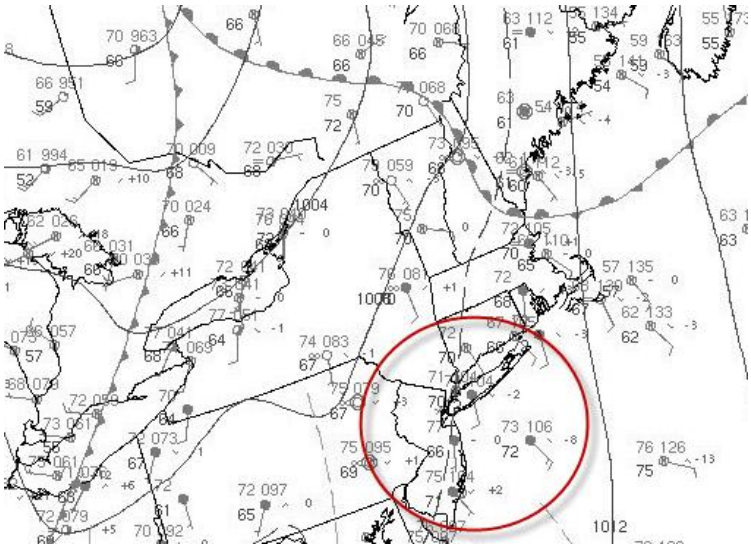

Fig. 29: Surface pressure map for the Northeast United States on 11 July 2007 (12pm) suggest that rainfall was not due to major synoptic influences or direct frontal movement.

Source: http://nomads.ncdc.noaa.gov

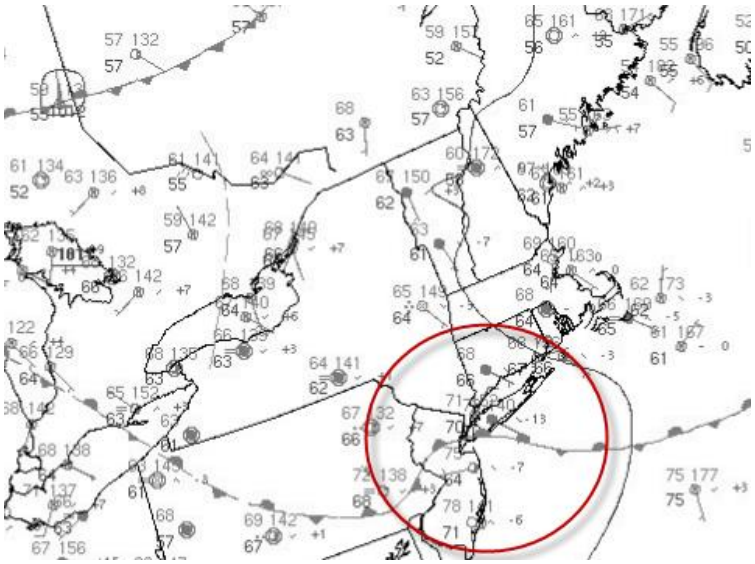

Fig. 30: Surface pressure map for 18 July 2007 (12pm). As a low pressure system develops directly southwest of the city, a stationary front contacts NYC. A stationary front is a non-moving boundary between two different air masses. Long periods of rainfall are common.

Source: http://nomads.ncdc.noaa.gov

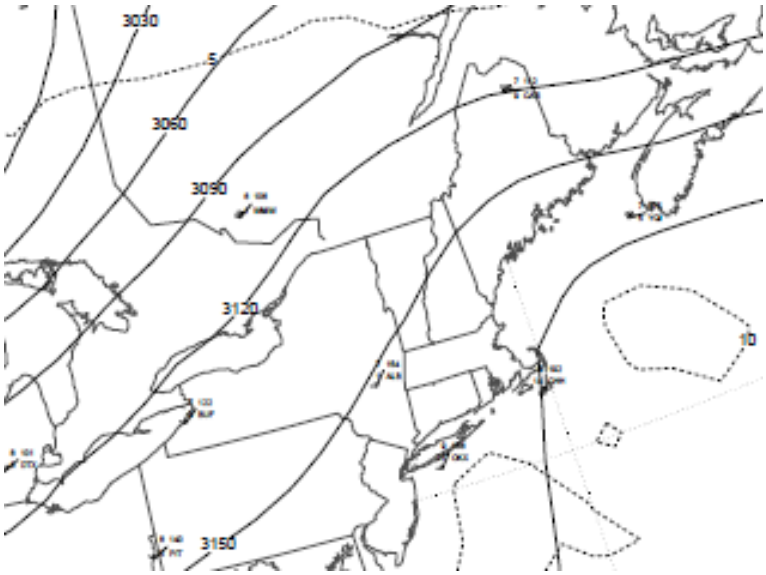

Fig. 31: The 700 mb upper level plot ten hours prior to the rainfall on 11 July 2007.

Source: http://weather.uwyo.edu/

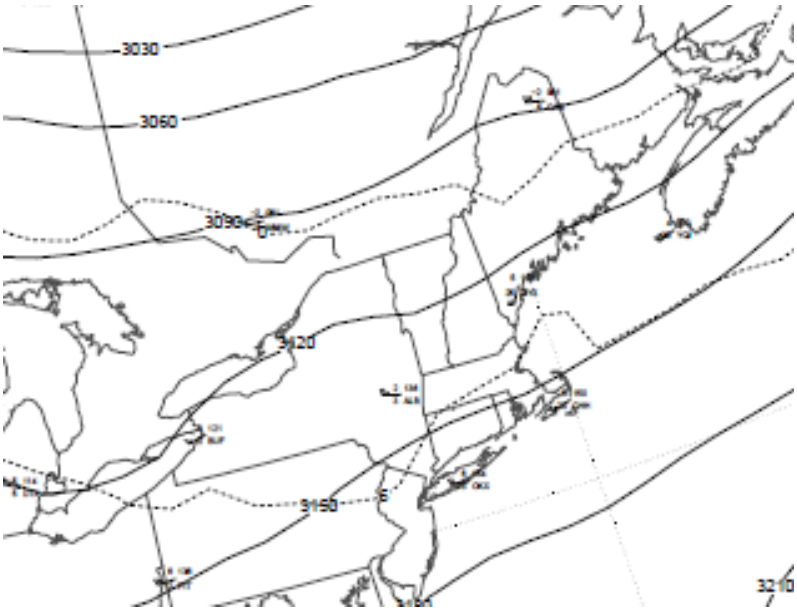

Fig. 32: The 700 mb upper level plot ten hours prior to the rainfall on 18 July 2007. Source:

http://weather.uwyo.edu/

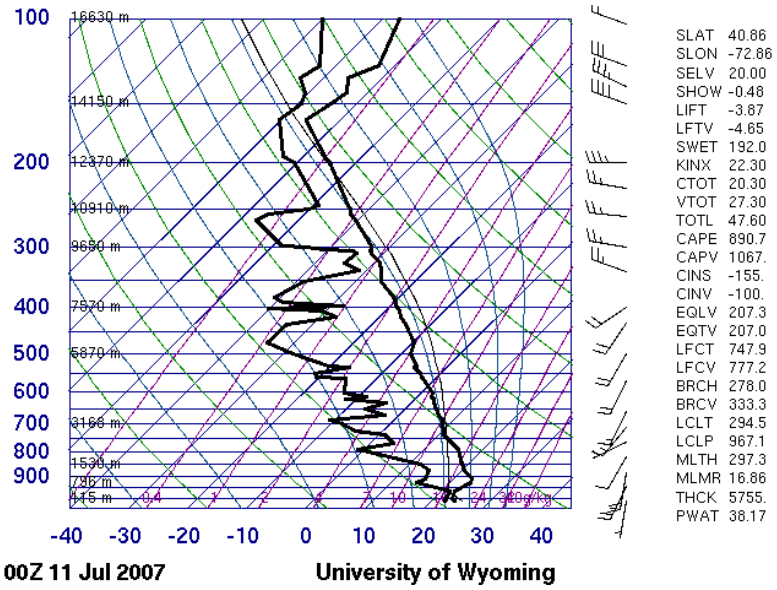

Fig. 33: The Skew-T plot ten hours prior to the rainfall on 11 July 2007. Here the Dew Point line experiences instability in the atmosphere at 300mb.

Source:http://weather.uwyo.edu/upperair/sounding.html

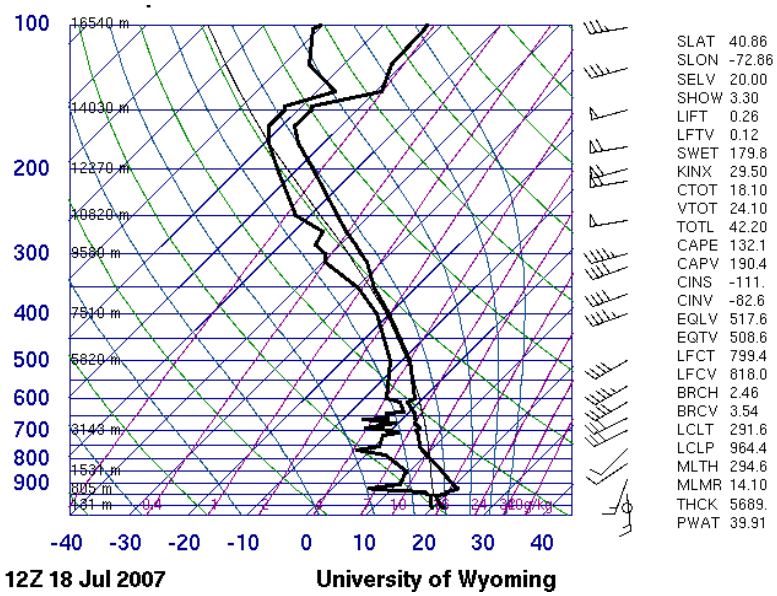

Fig. 34: Skew-T plot seven hours prior to the rainfall on 18 July 2007. Here, the Dew Point line experiences marginal instability in the atmosphere below 500mb.

Source: http://weather.uwyo.edu/upperair/sounding.html

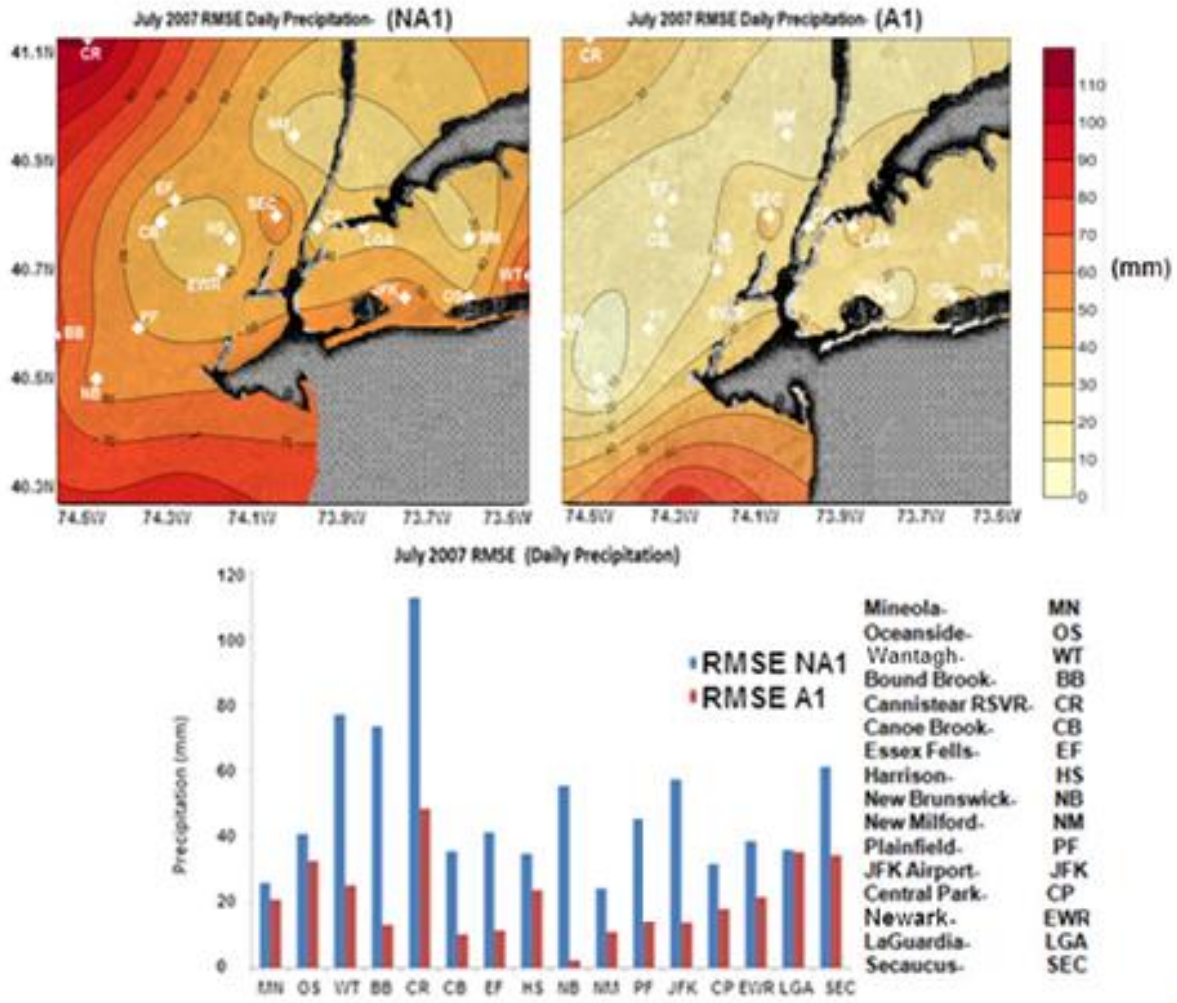

Fig. 35: Accumulated daily precipitation RMSE for the A1 (top left) and NA1 (top right) cases. The bar graph (bottom) is representative of actual RMSE values for each simulation over the 16 sites. The blue bars represent the errors for the A1 case, red bars are the errors for the NA1 case.

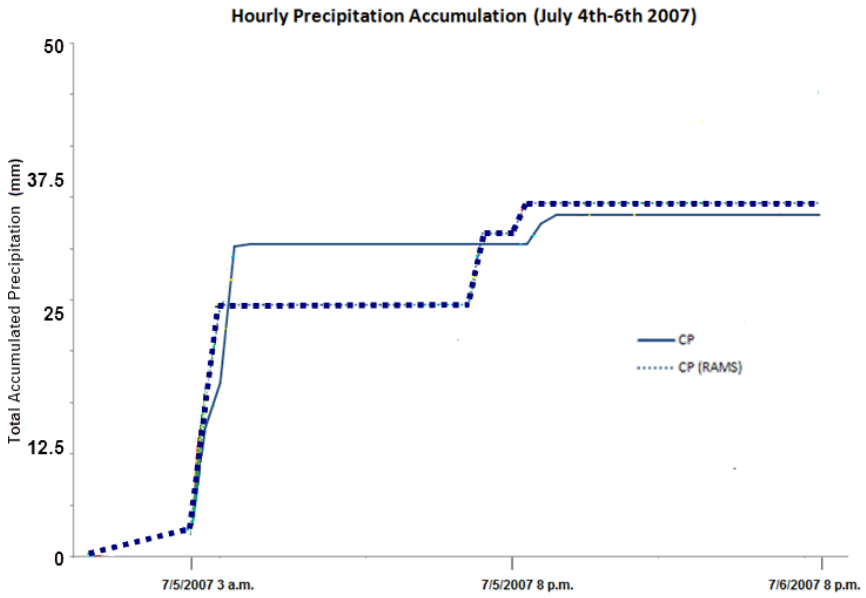

Fig. 36: Precipitation over CP for 4-6 July 2007. Dotted lines represent model results. Solid lines represent observations.

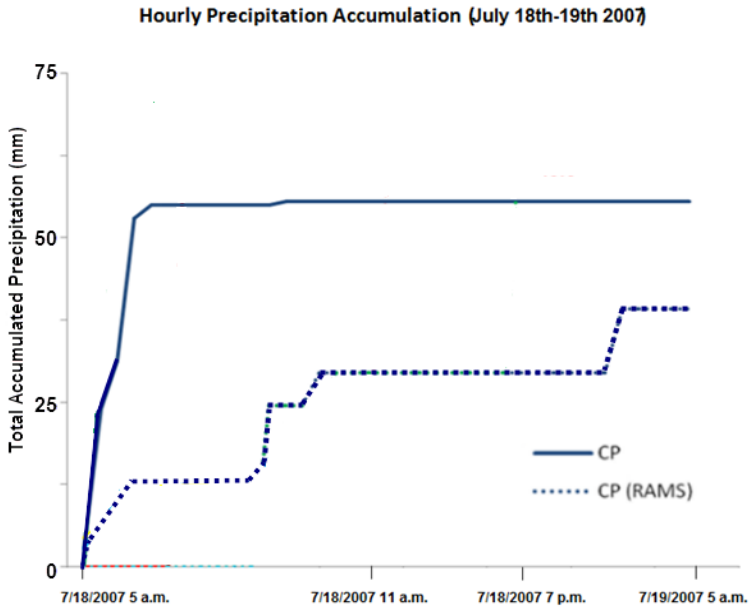

Fig. 37: Precipitation over CP for 18 July 2007. Dotted lines represent model results. Solid lines represent observations.

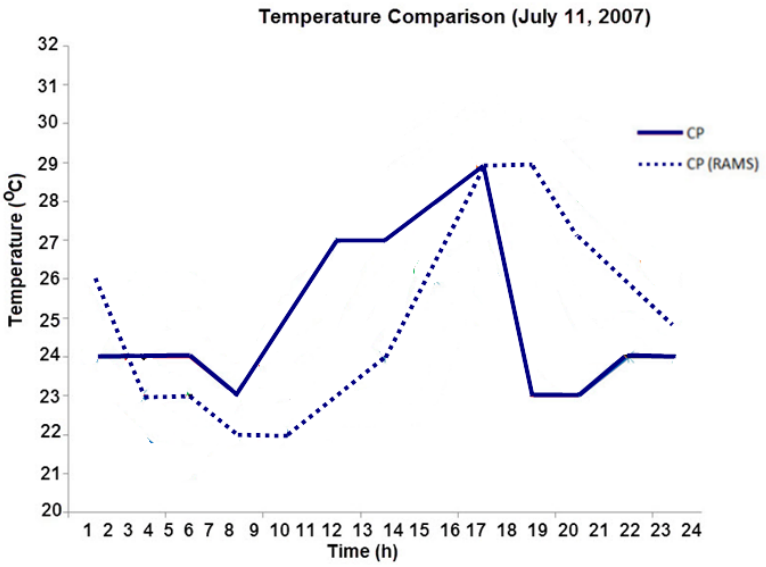

Fig. 38: RAMS surface temperature validation for 11 July 2007 with PSD assimilation for CP, where solid lines are NWS observations, and dashed lines are model results.

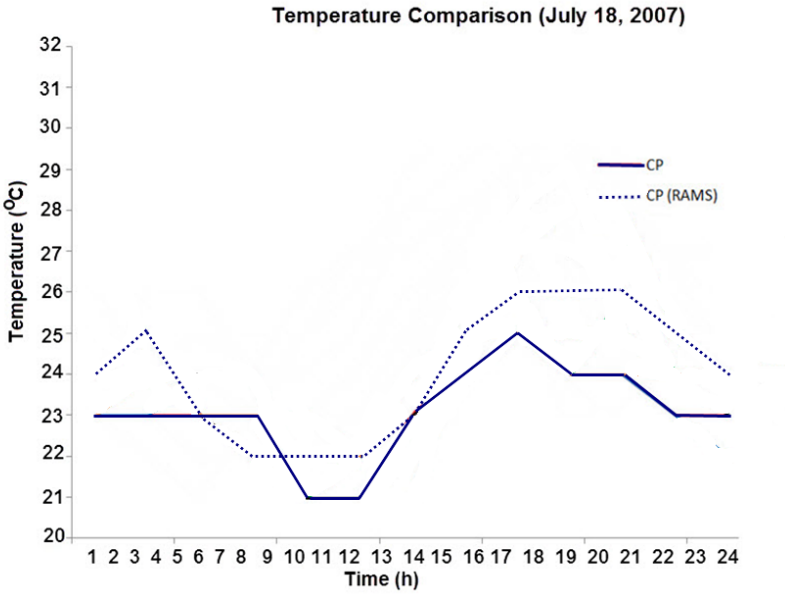

Fig. 39: RAMS surface temperature validation for 18 July 2007 with PSD assimilation for CP, where solid lines are NWS observations, and dashed lines are model results.

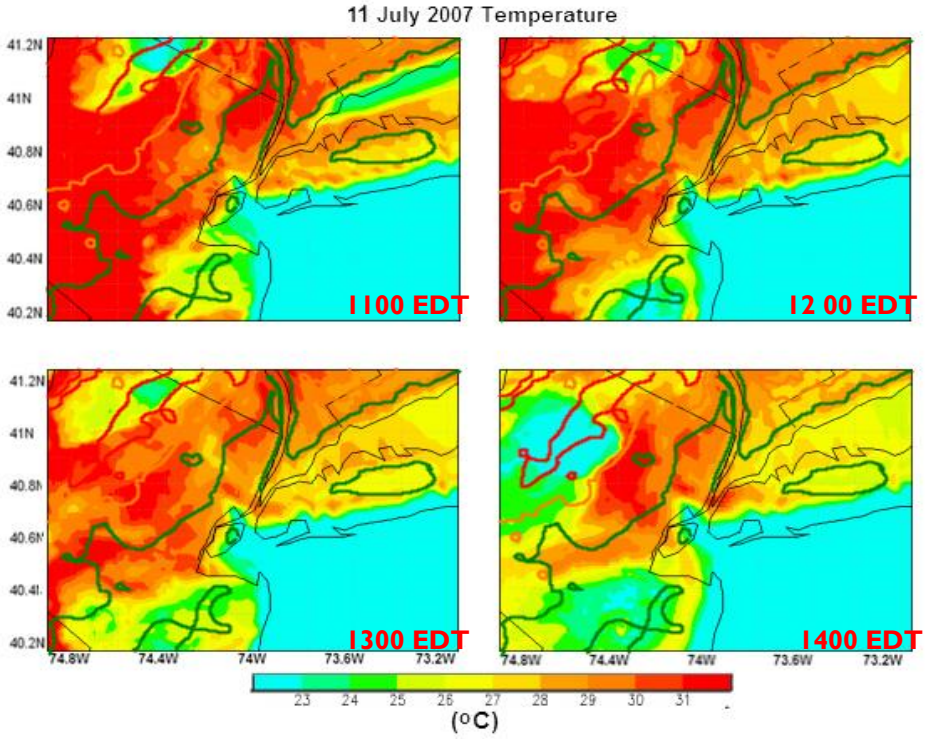

Fig. 40: 11 July 2007 temperature over the NYC region 2 m from the surface at different times between 1100 and 1400 EDT.

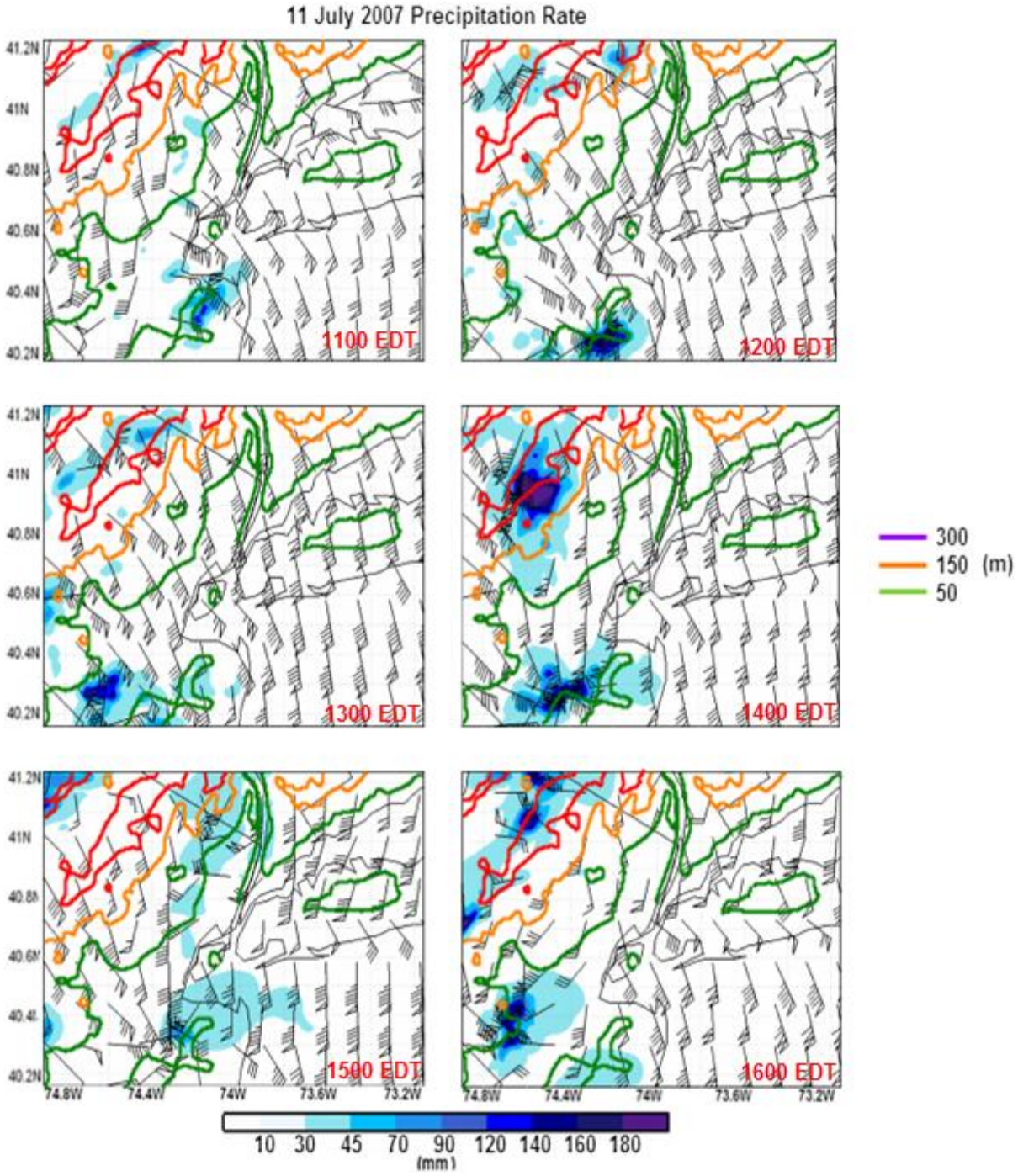

Fig. 41: Hourly precipitation rates for Run 1, 11 July 2007 with ingested data, representing a localized event (wind barbs are multiplied by a factor of 10).

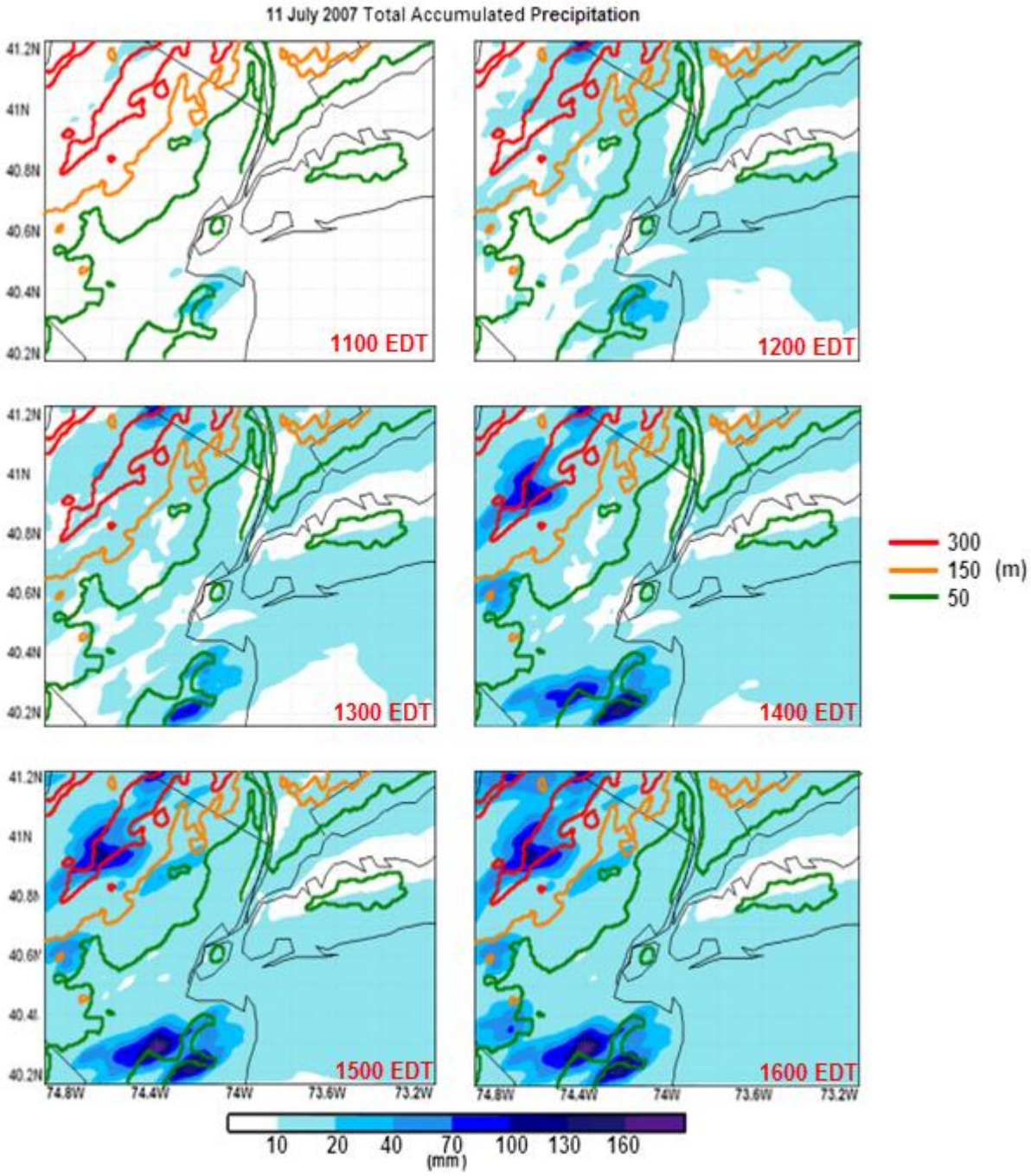

Fig. 42: Hourly total accumulated precipitation for Run 1, 11 July 2007 with ingested PSD data, representing a localized event.

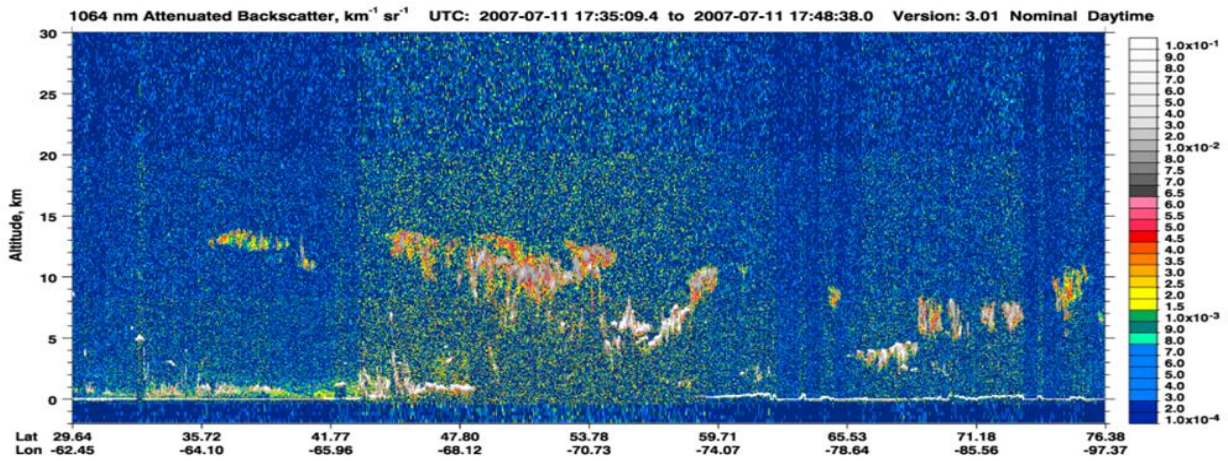
1064 nm Attenuated Backscatter, km-1 sr-1 UTC: 2007-07-11 17:35:09.4 to 2007-07-11 17:48:38.0 Version: 3.01 Nominal Daytime
Altitude, km
Lat 29.64 35.72 41.77 47.80 53.78 59.71 65.53 71.18 76.38
Lon -62.45 -64.10 -65.96 -68.12 -70.73 -74.07 -78.64 -85.56 -97.37

a)

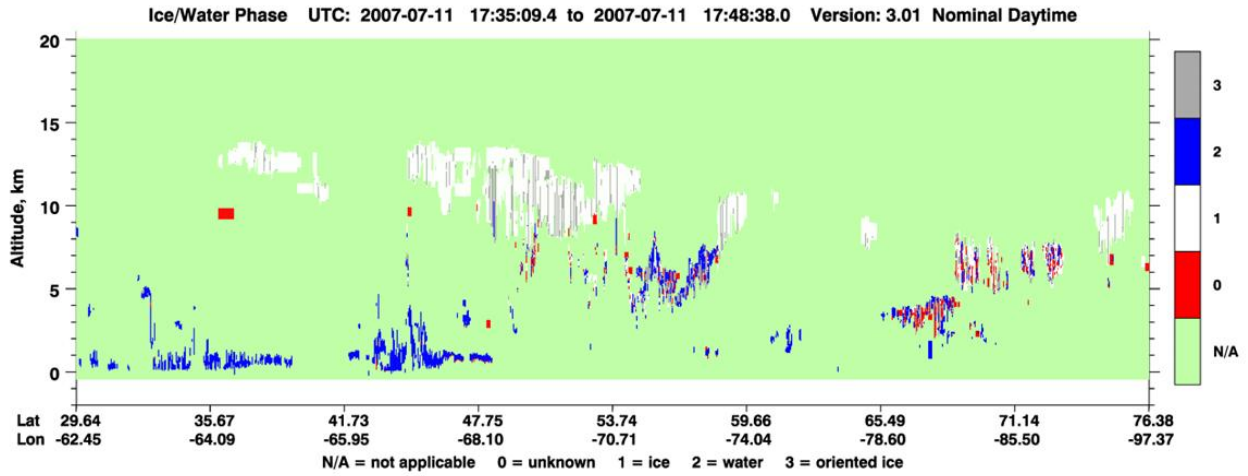
Ice/Water Phase UTC: 2007-07-11 17:35:09.4 to 2007-07-11 17:48:38.0 Version: 3.01 Nominal Daytime
Altitude, km
Lat 29.64 35.67 41.73 47.75 53.74 59.66 65.49 71.14 76.38
Lon -62.45 -64.09 -65.95 -68.10 -70.71 -74.04 -78.60 -85.50 -97.37
N/A = not applicable 0 = unknown 1 = ice 2 = water 3 = oriented ice

b)

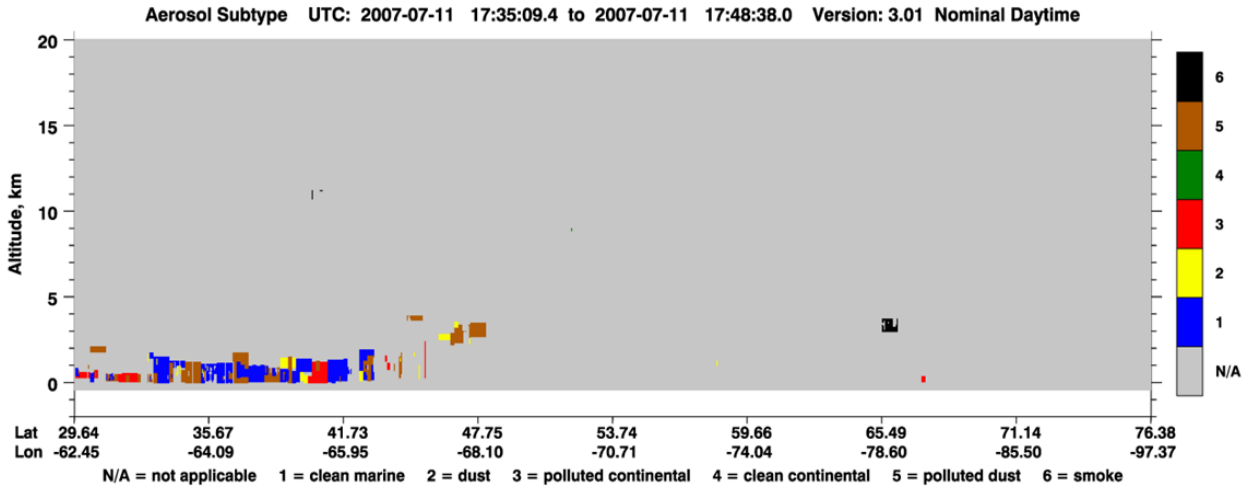
Aerosol Subtype UTC: 2007-07-11 17:35:09.4 to 2007-07-11 17:48:38.0 Version: 3.01 Nominal Daytime
Altitude, km
Lat 29.64 35.67 41.73 47.75 53.74 59.66 65.49 71.14 76.38
Lon -62.45 -64.09 -65.95 -68.10 -70.71 -74.04 -78.60 -85.50 -97.37
N/A = not applicable 1 = clean marine 2 = dust 3 = polluted continental 4 = clean continental 5 = polluted dust 6 = smoke

c)

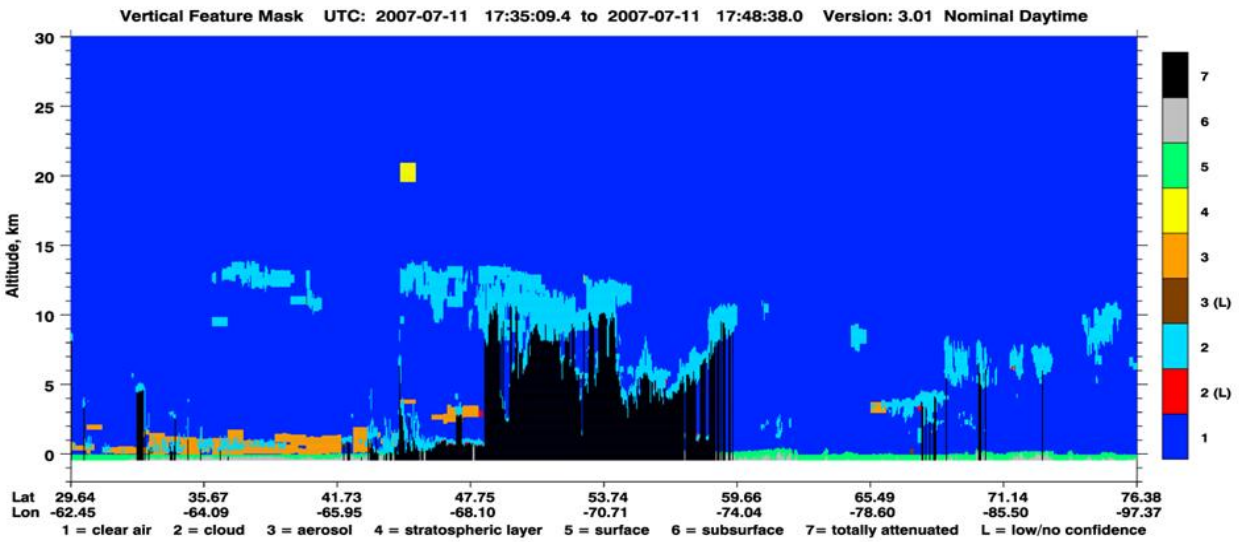

d)

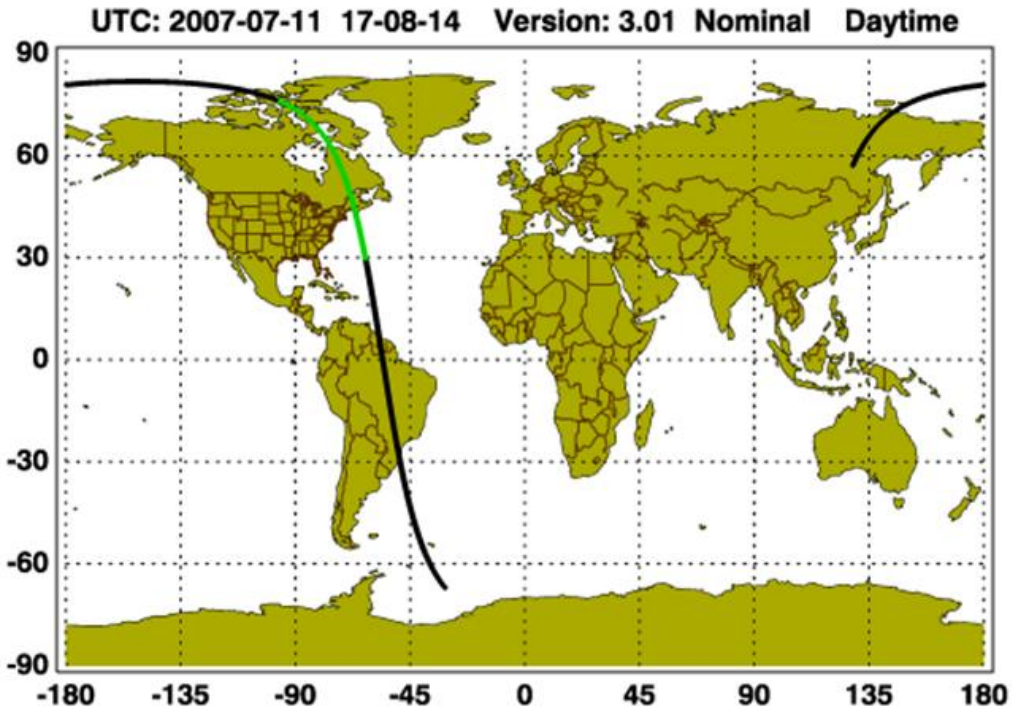

e)

Fig. 43: CALIPSO data for 11July 2007. a) Attenuated backscatter. b) Water phase in the cloud structure. c) Aerosol subtype. d) Atmospheric features over the region. e) Satellite path. The green band shows the region of data for plots a through d.

Source: http://eosweb.larc.nasa.gov/PRODOCS/calipso/table_calipso.html

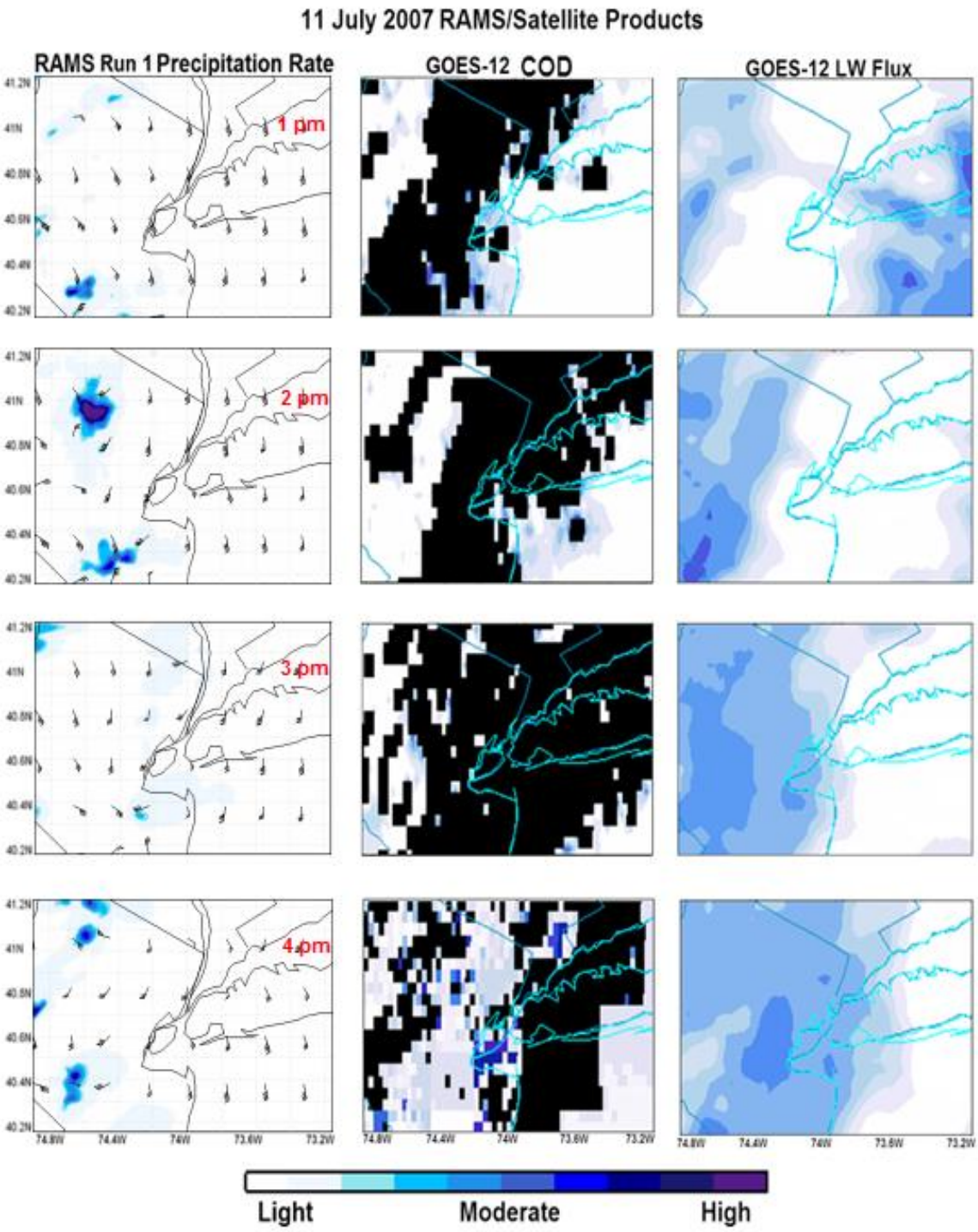

Fig. 44: 11 July 2007 comparison of evolution between: a) Run 1 precipitation rate (column 1), b) COD (column 2), and c) LW Flux (column 3). Row 1 is 1pm Row 2 is 2pm, Row 3 is 3pm, and Row 4 is at 4pm.

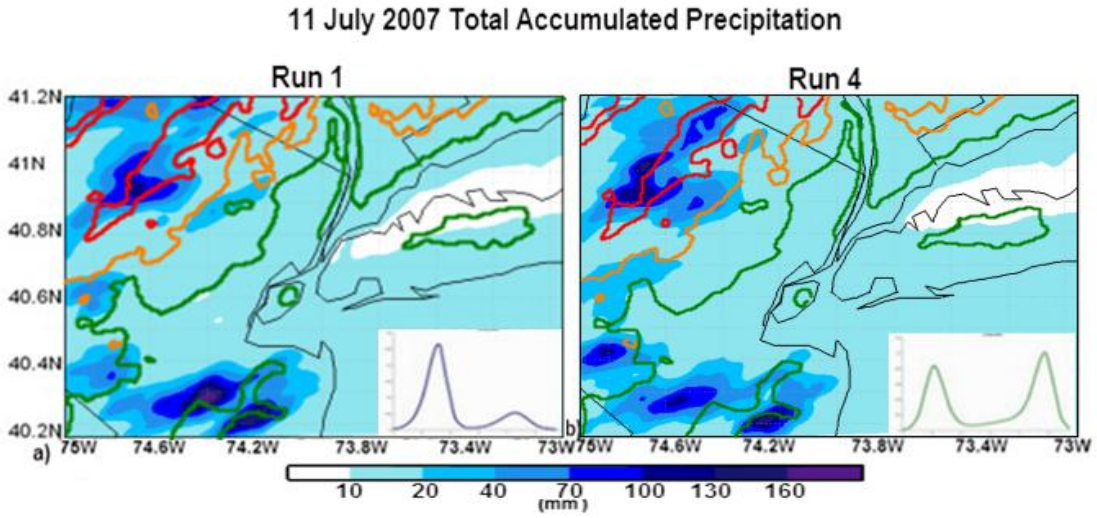

Fig. 45: a) Total accumulated precipitation for 11 July 2007. The ingested PSD is shown on the lower right portion of the plot. This is the HVFM PSD measured at the CCNY AERONET site on 11 July 2007. b) Total Accumulated Precipitation for 11 July 2007. The ingested PSD is shown on the lower right portion of the plot. This is the HVCM PSD measured at the CCNY AERONET site on 18 July 2007.

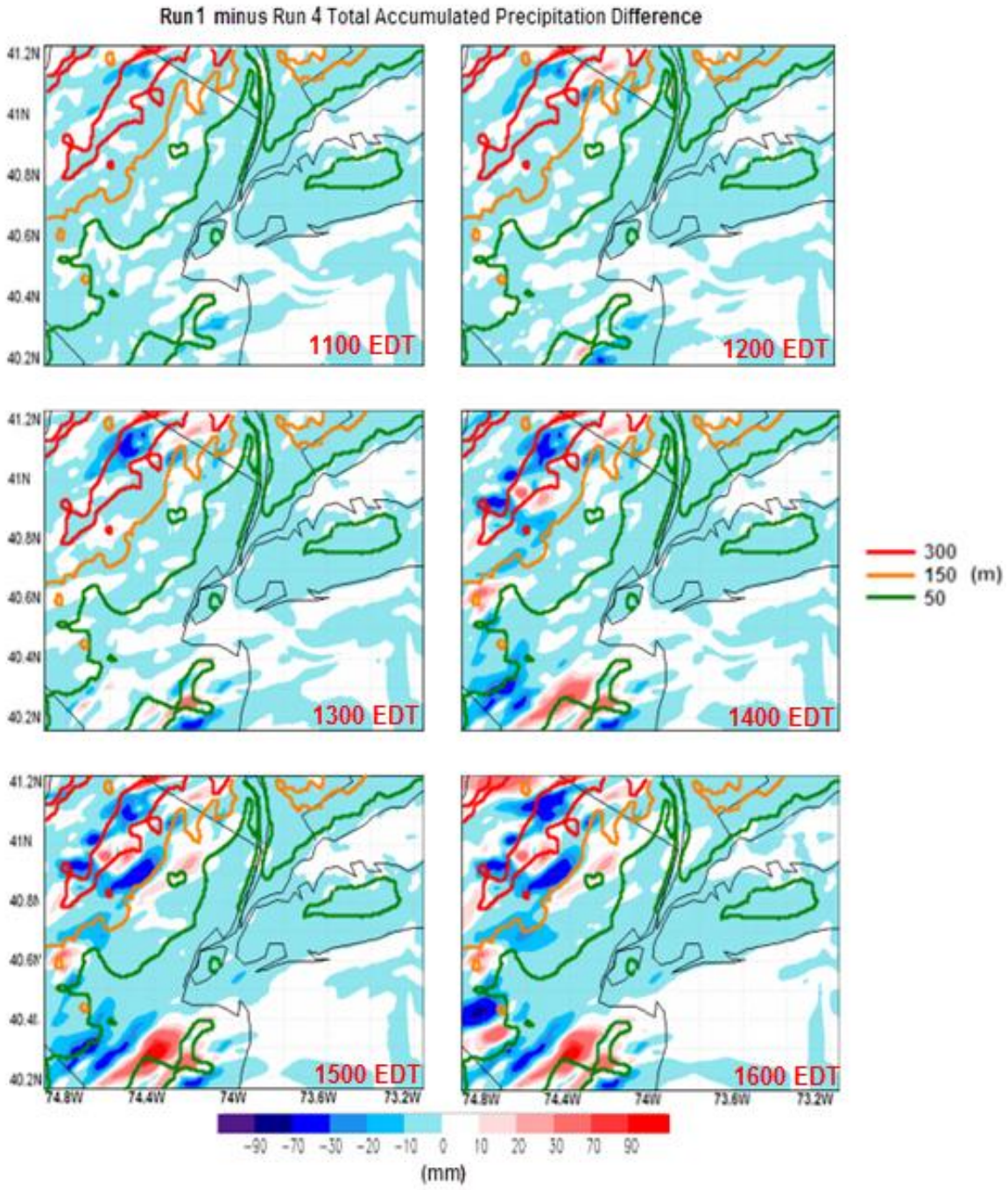

Fig. 46: Total accumulated precipitation difference between the observed and idealized cases for 11 July 2007.

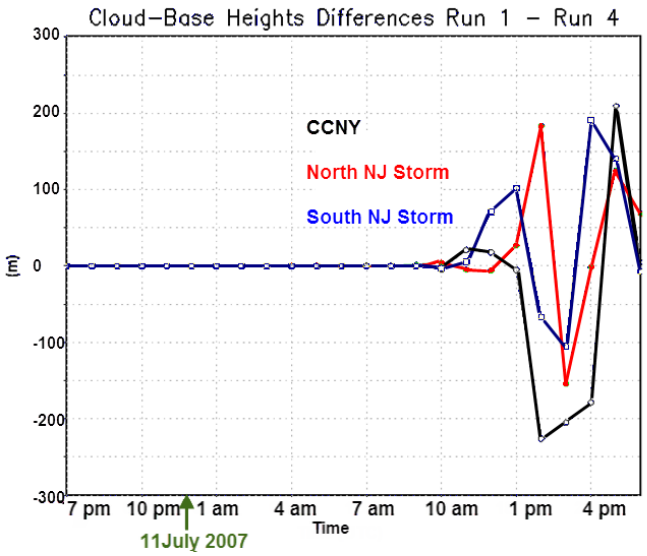

Fig. 47: CBH differences for three sites for Run 1 minus Run 4 (HVFM – HVCM, City Case) within the region of interest.

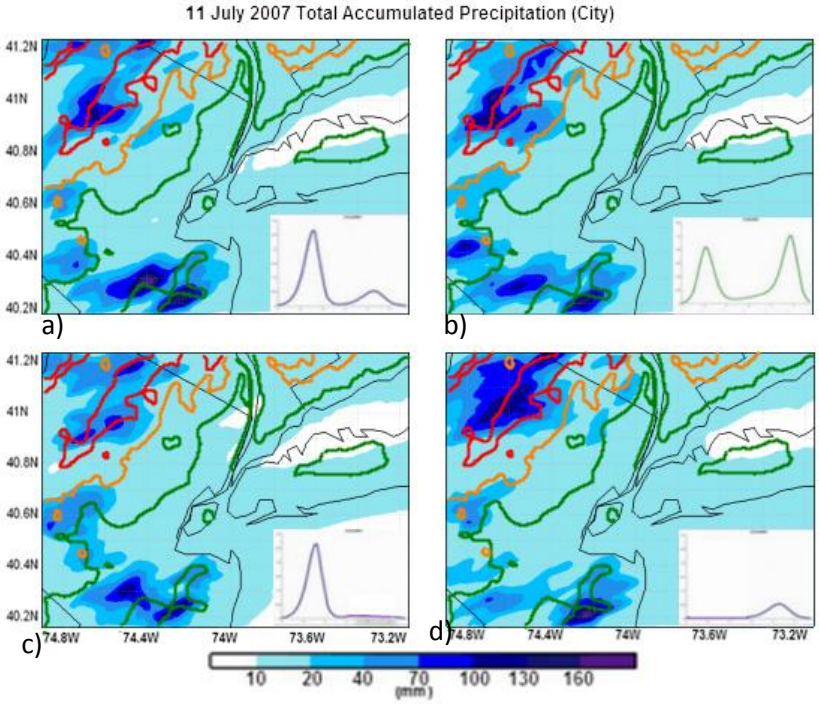

Fig. 48: Total accumulated precipitation PSD sensitivity cases for the 11 July 2007 localized event. a) Observed PSD (Run 1). b) PSD for 18 July 2007 (Run 4). c) Observed PSD, no coarse mode (Run 7). d) Observed PSD, no fine mode (Run 8).

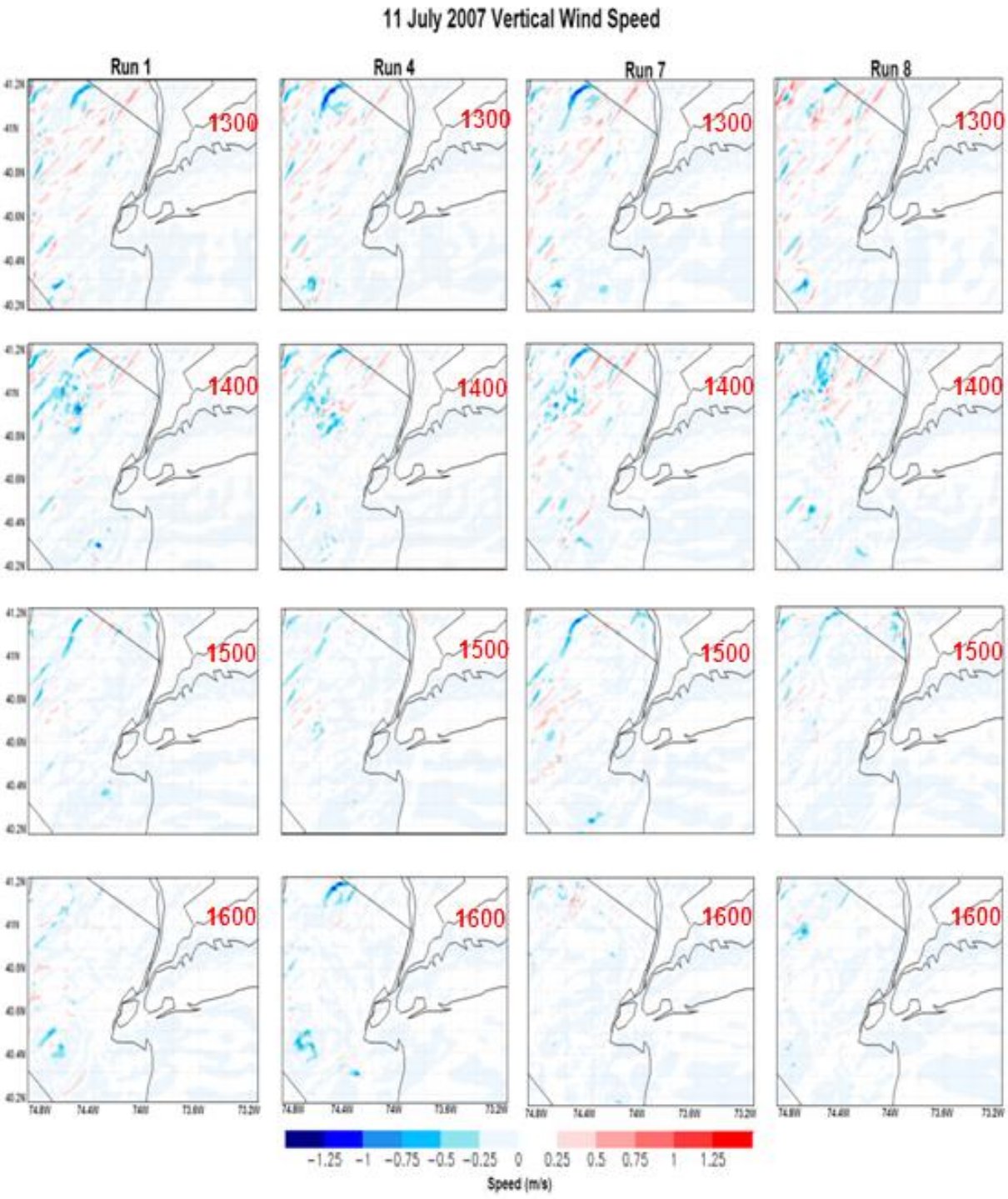

Fig. 49: PSD sensitivity cases vertical wind for the 11 July 2007 localized event. a) Observed PSD (Run 1). b) PSD for 18 July 2007 (Run 4). c) Observed PSD, no fine mode (Run 7). d) Observed PSD, no coarse mode (Run 8). Maximum wind is on the order of +/- 1m s^{-1}.

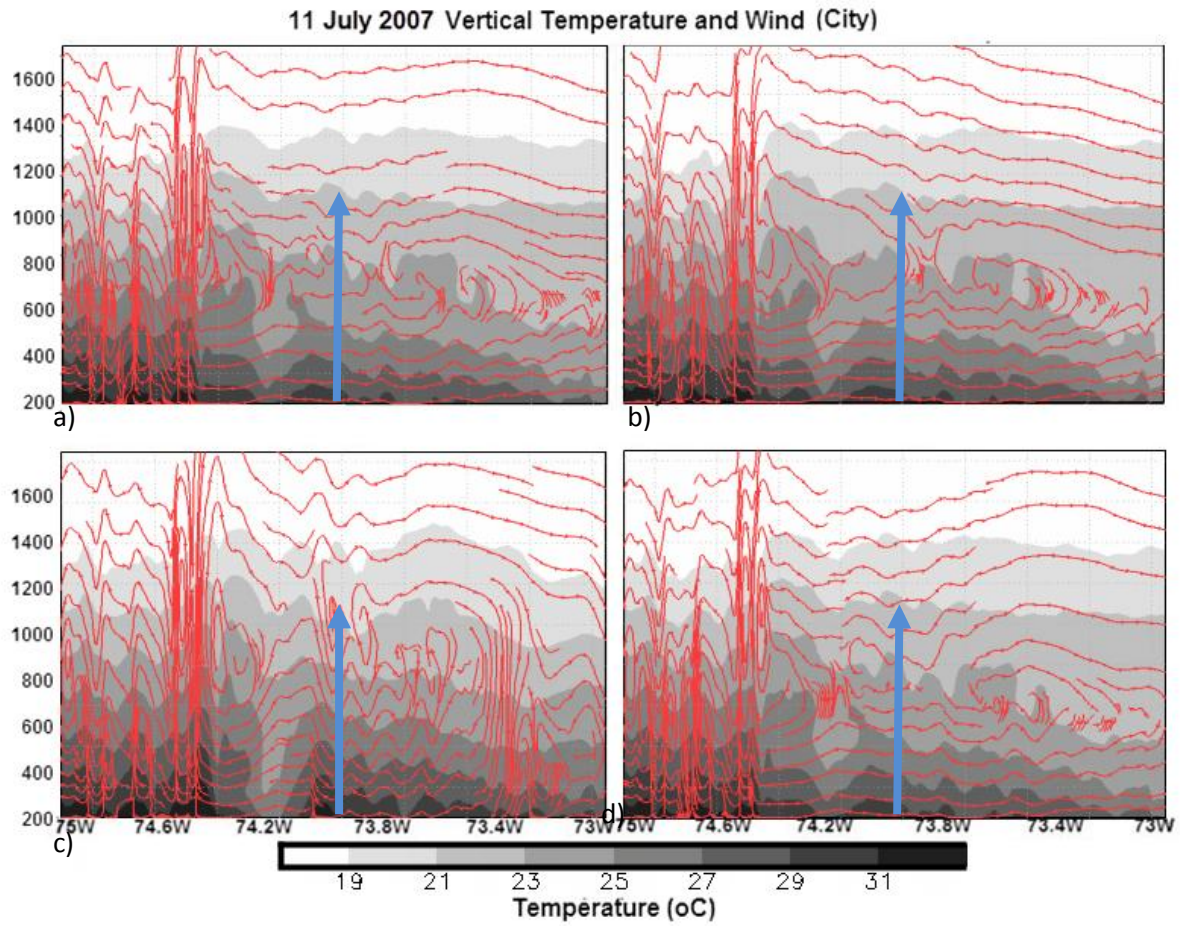

Fig. 50: PSD sensitivity cases vertical temperature and wind for the 11 July 2007 localized event. a) Observed PSD (Run 1). b) PSD for 18 July 2007 (Run 4). c) Observed PSD, no fine mode (Run 7). d) Observed PSD, no coarse mode (Run 8). Wind streamlines are for u and w, measured in m s^{-1}. Maximum vertical wind is on the order of 1 m s^{-1}. Blue arrows mark the location of NYC.

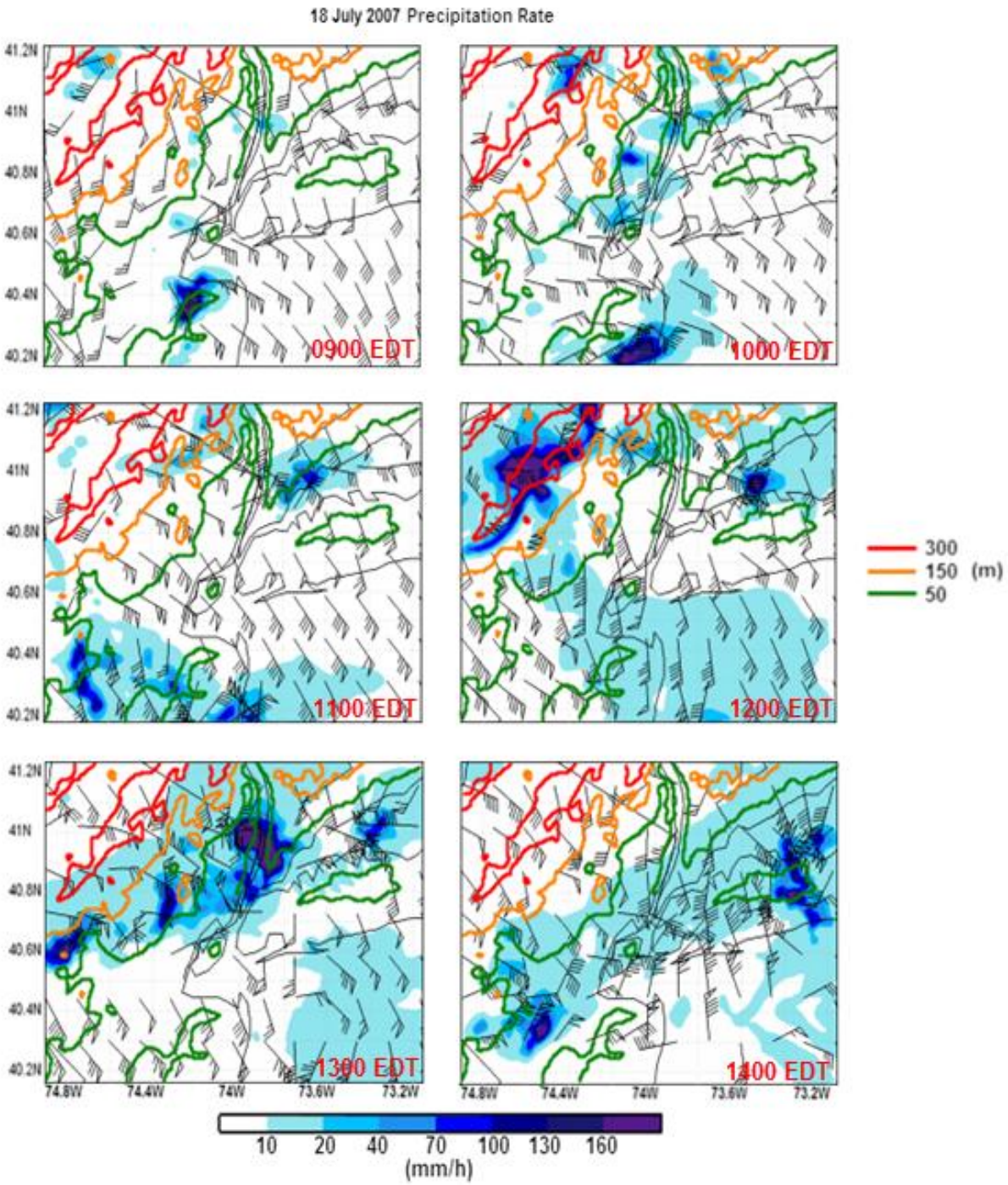

Fig. 51: Hourly precipitation rate for Run 3, 18 July 2007 with assimilated PSD data, representing a mesoscale event.

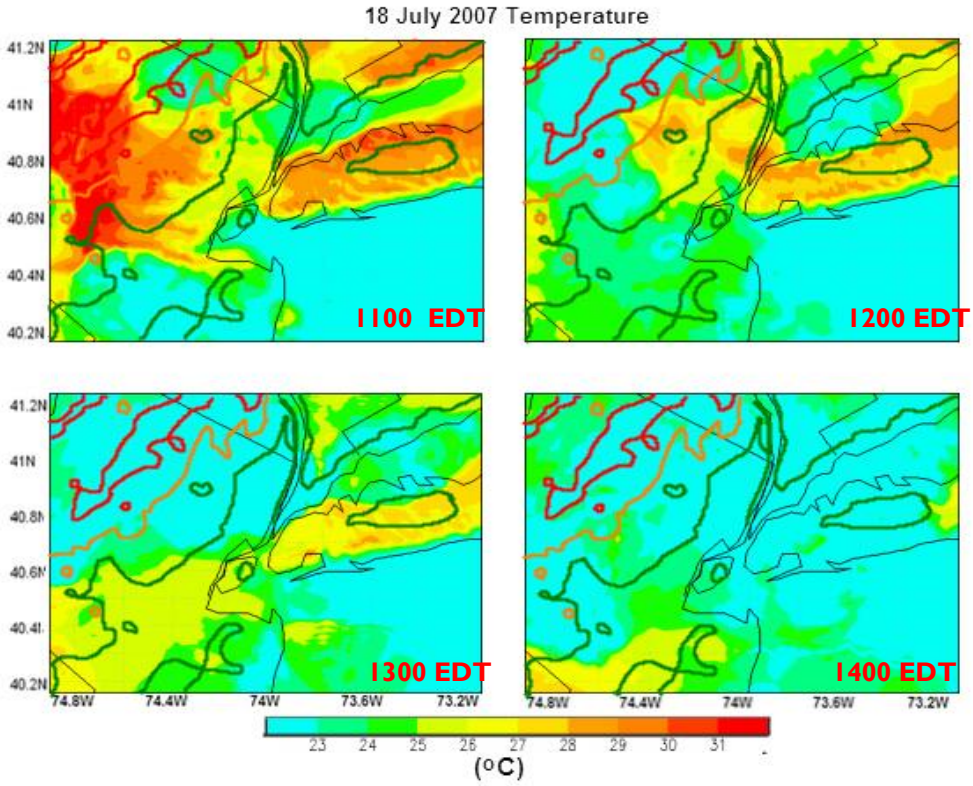

Fig. 52: 18 July 2007 temperature over the NYC region 2 m from the surface at different times between 1100 and 1400 EDT.

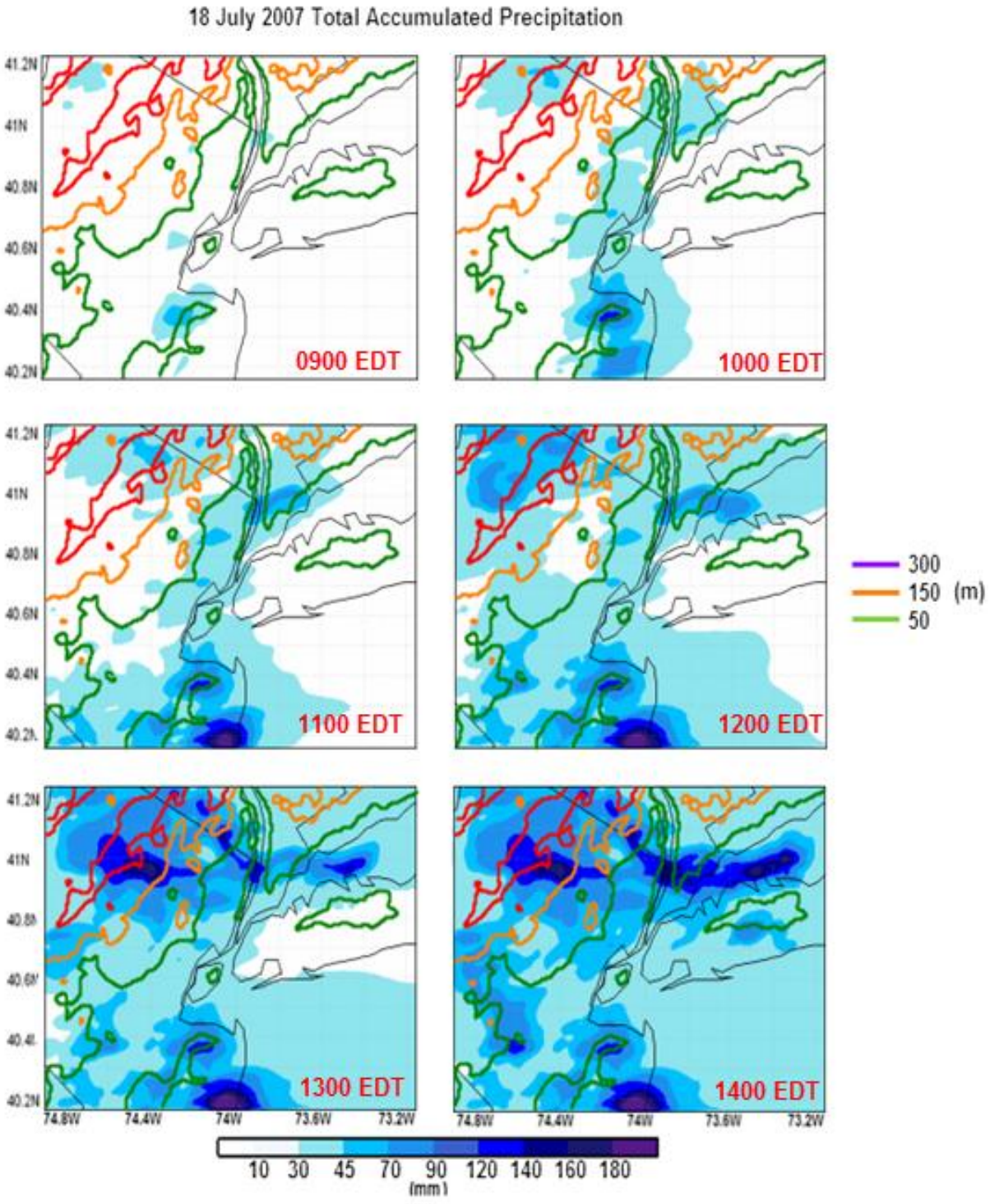

Fig. 53: Hourly total accumulated precipitation for Run 3, 18 July 2007 with ingested PSD data, representing a mesoscale event.

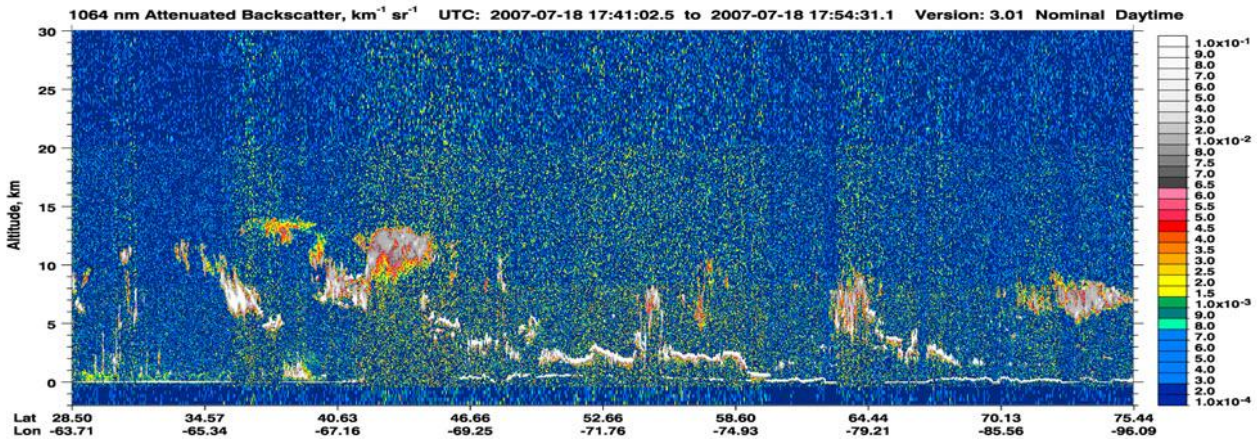
1064 nm Attenuated Backscatter, km-1 sr-1 UTC: 2007-07-18 17:41:02.5 to 2007-07-18 17:54:31.1 Version: 3.01 Nominal Daytime
Altitude, km
Lat 28.50 34.57 40.63 46.66 52.66 58.60 64.44 70.13 75.44
Lon -63.71 -65.34 -67.16 -69.25 -71.76 -74.93 -79.21 -85.56 -96.09

a)

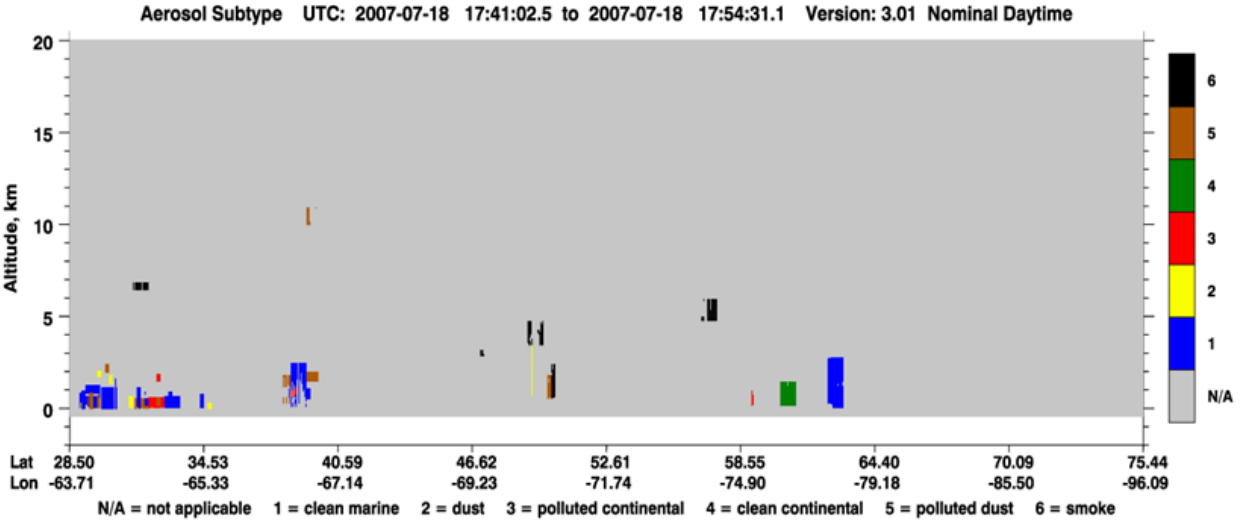
Aerosol Subtype UTC: 2007-07-18 17:41:02.5 to 2007-07-18 17:54:31.1 Version: 3.01 Nominal Daytime
Altitude, km
Lat 28.50 34.53 40.59 46.62 52.61 58.55 64.40 70.09 75.44
Lon -63.71 -65.33 -67.14 -69.23 -71.74 -74.90 -79.18 -85.50 -96.09
N/A = not applicable 1 = clean marine 2 = dust 3 = polluted continental 4 = clean continental 5 = polluted dust 6 = smoke

b)

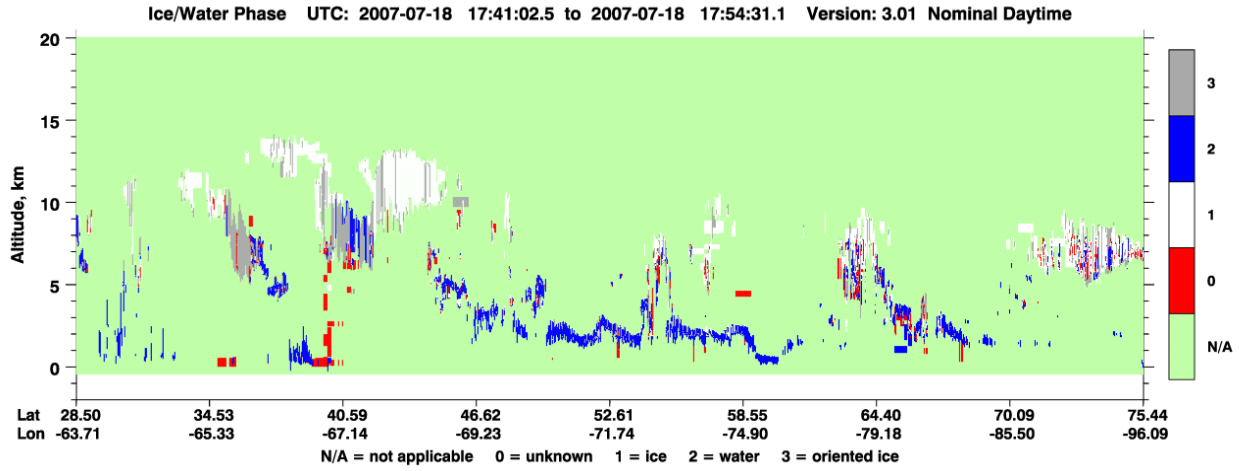
Ice/Water Phase UTC: 2007-07-18 17:41:02.5 to 2007-07-18 17:54:31.1 Version: 3.01 Nominal Daytime
Altitude, km
Lat 28.50 34.53 40.59 46.62 52.61 58.55 64.40 70.09 75.44
Lon -63.71 -65.33 -67.14 -69.23 -71.74 -74.90 -79.18 -85.50 -96.09
N/A = not applicable 0 = unknown 1 = ice 2 = water 3 = oriented ice

c)

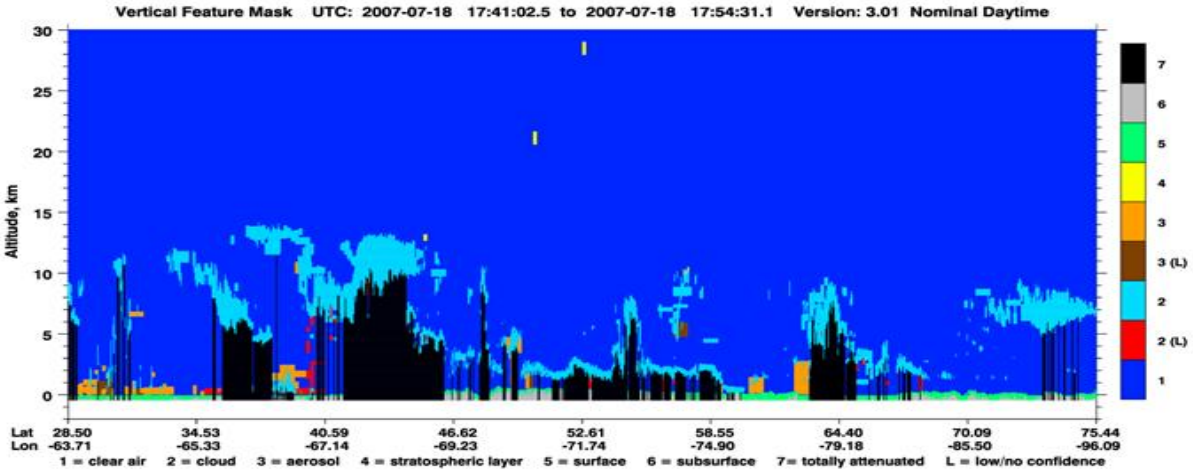

d)

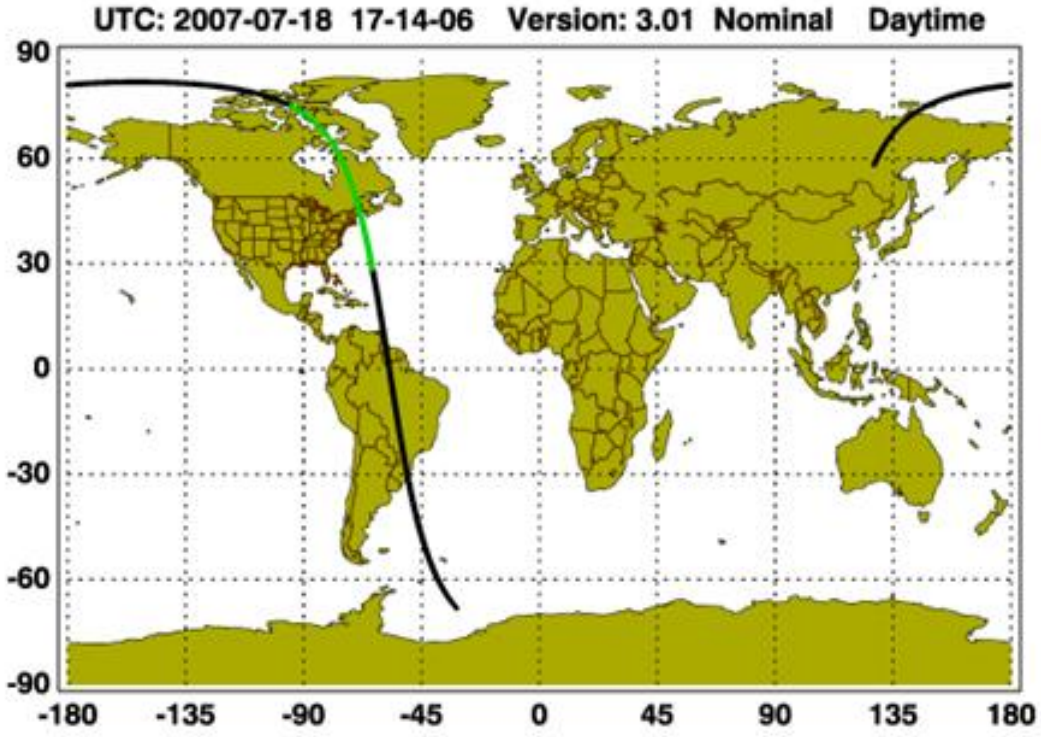

e)

Fig. 54: CALIPSO data for 18 July 2007. a) Attenuated backscatter. b) Water phase in the cloud structure. c) Aerosol subtype. d) Atmospheric features over the region. e) Satellite path. The green band shows the region of data for plots a through d.

Source: http://eosweb.larc.nasa.gov/PRODOCS/calipso/table_calipso.html

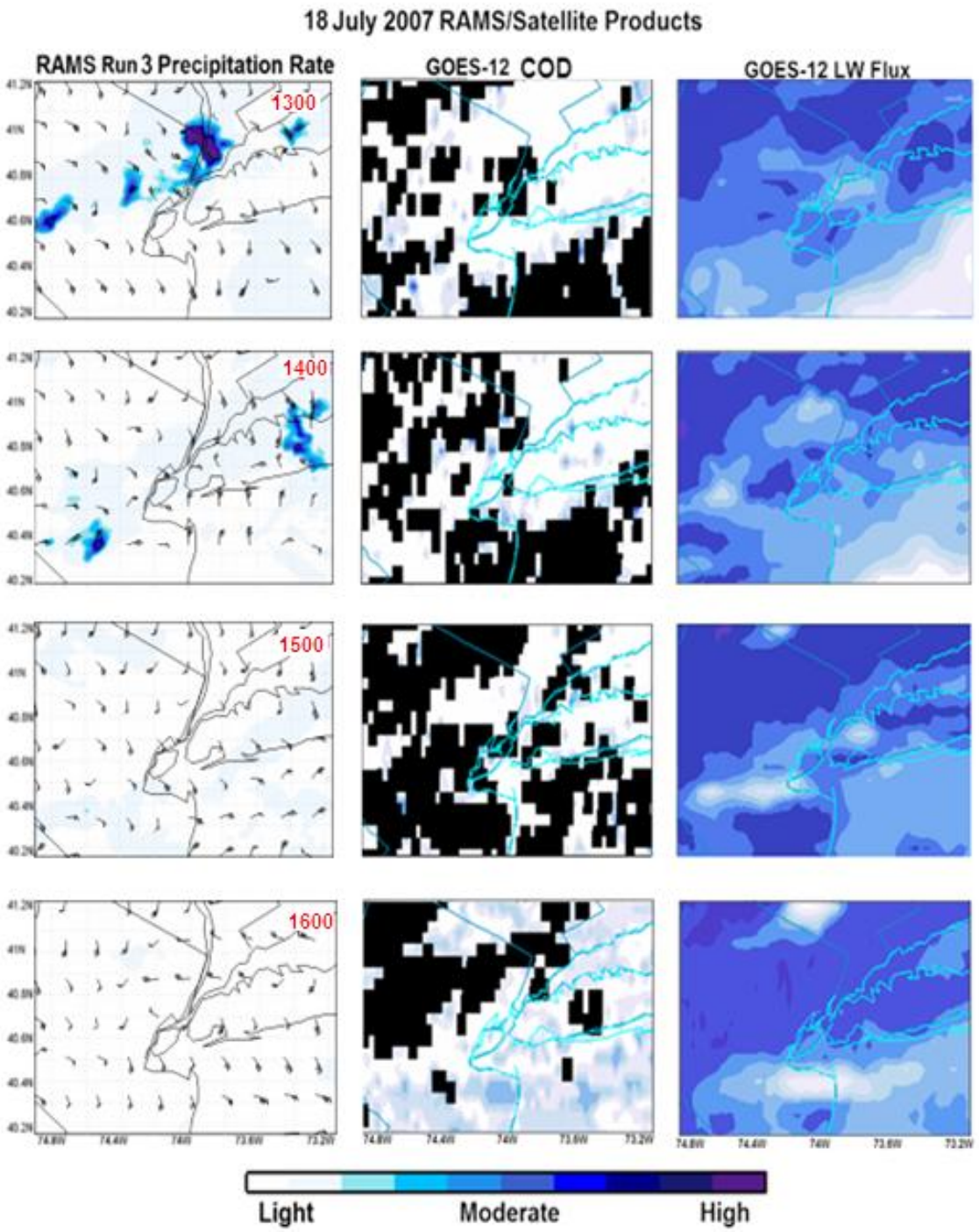

Fig. 55: 18 July 2007 comparison of evolution between: a) Run 3 precipitation rate (column 1), b) COD (column 2), and c) LW Flux (column 3). Row 1 is 1pm Row 2 is 2pm, Row 3 is 3pm, and Row 4 is at 4pm.

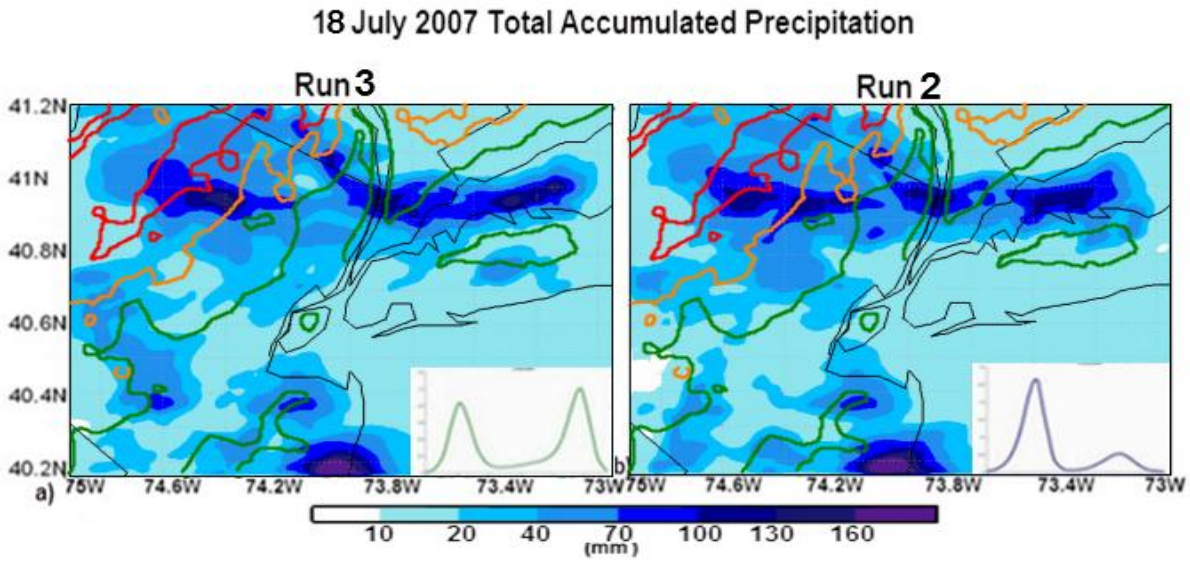

Fig. 56: a) Total Accumulated Precipitation for 18 July 2007. The ingested PSD is shown on the lower right portion of the plot. This is the PSD observed at the CCNY AERONET site on 18 July 2007. b) Total Accumulated Precipitation for 18 July 2007. The ingested PSD is shown on the lower right portion of the plot. This is the PSD measured at the CCNY AERONET site on 11 July 2007.

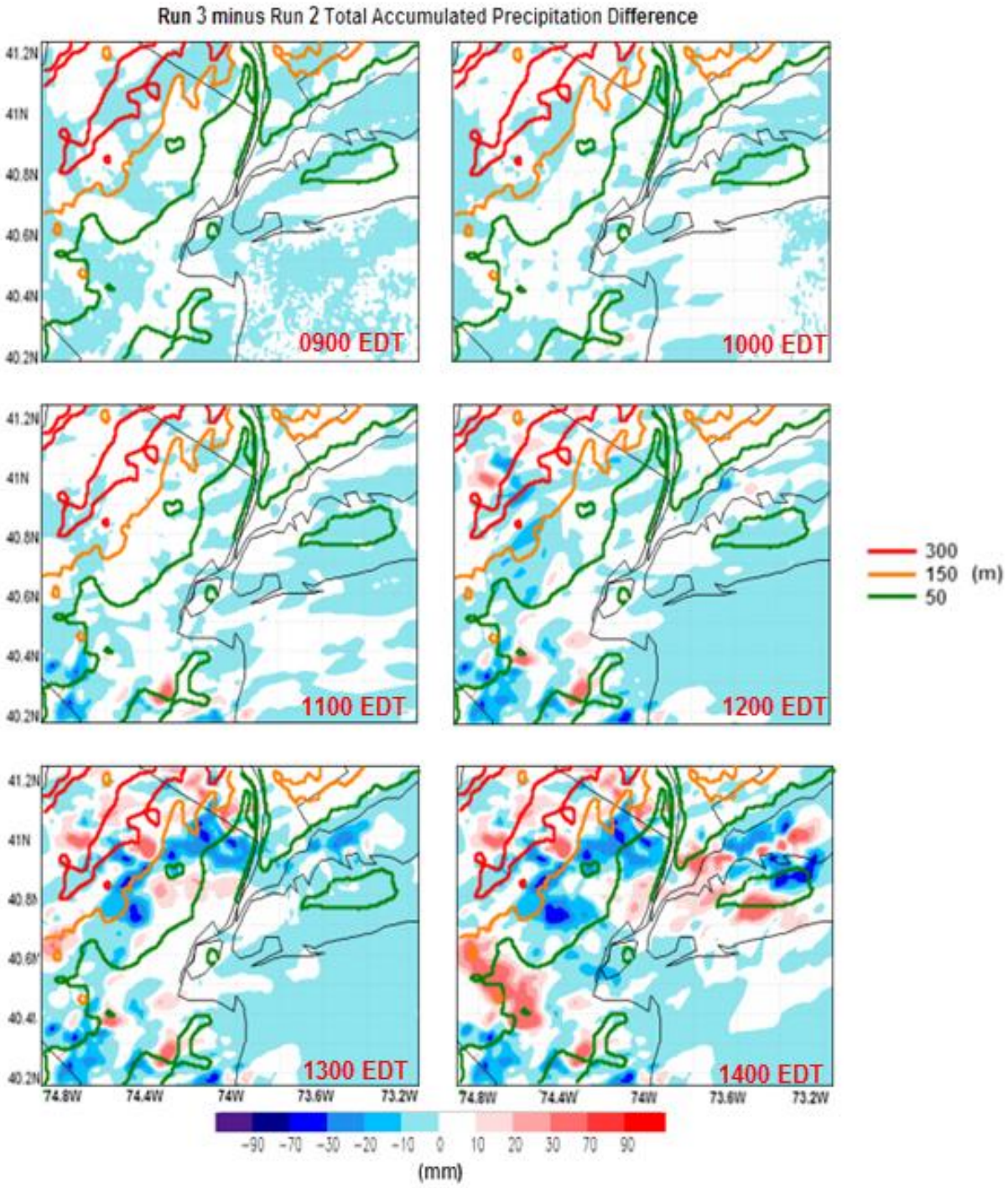

Fig. 57: Total accumulated precipitation difference between the observed and idealized cases for 18 July 2007.

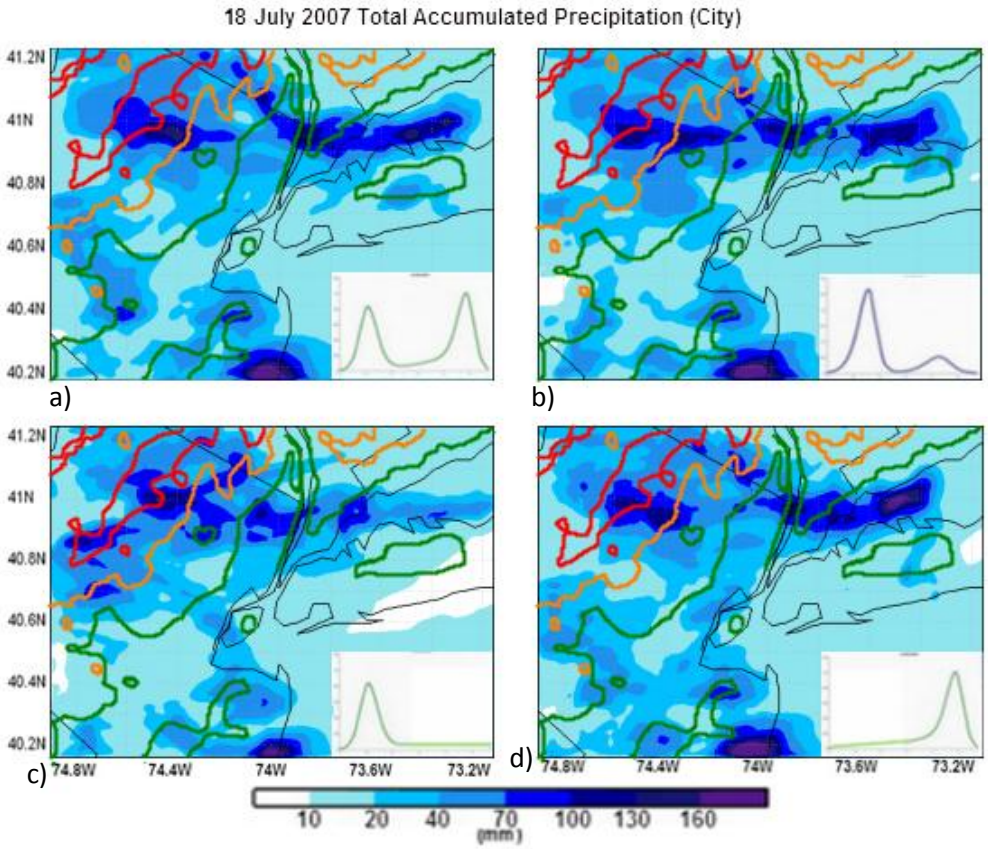

Fig. 58: Total accumulated precipitation PSD sensitivity cases for the 18 July 2007 localized event. a) Observed PSD (Run 3). b) PSD for 18 July 2007 (Run 4). c) Observed PSD, no coarse mode (Run 9). d) Observed PSD, no fine mode (Run 10).

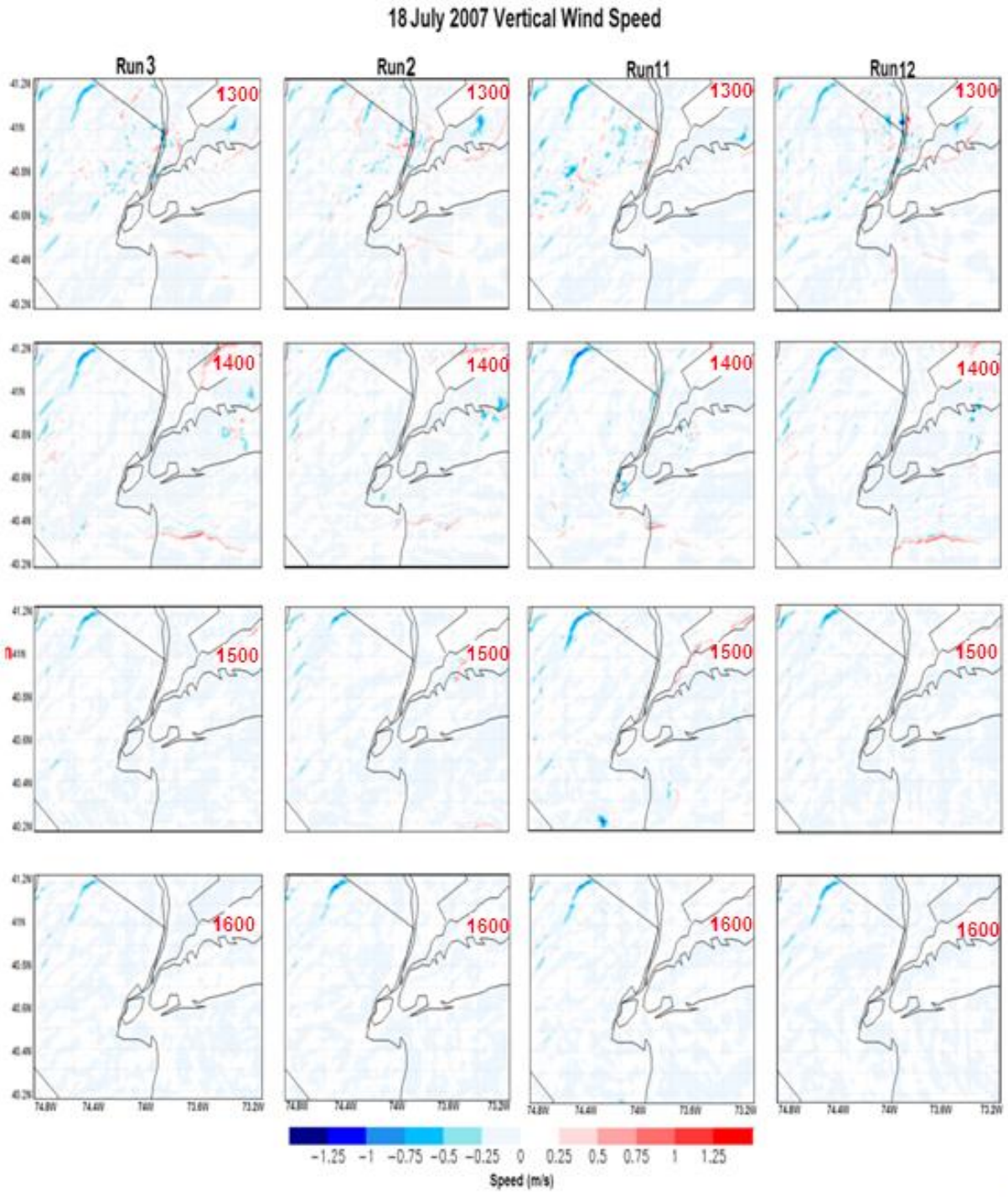

Fig. 59: Vertical wind for PSD sensitivity cases for the 18 July 2007 regional event. a) Observed PSD (Run 3). b) PSD for 18 July 2007 (Run 2). c) Observed PSD, no coarse mode (Run 11). d) Observed PSD no fine mode (Run 12). Maximum wind is on the order of +/-1 m s^{-1}.

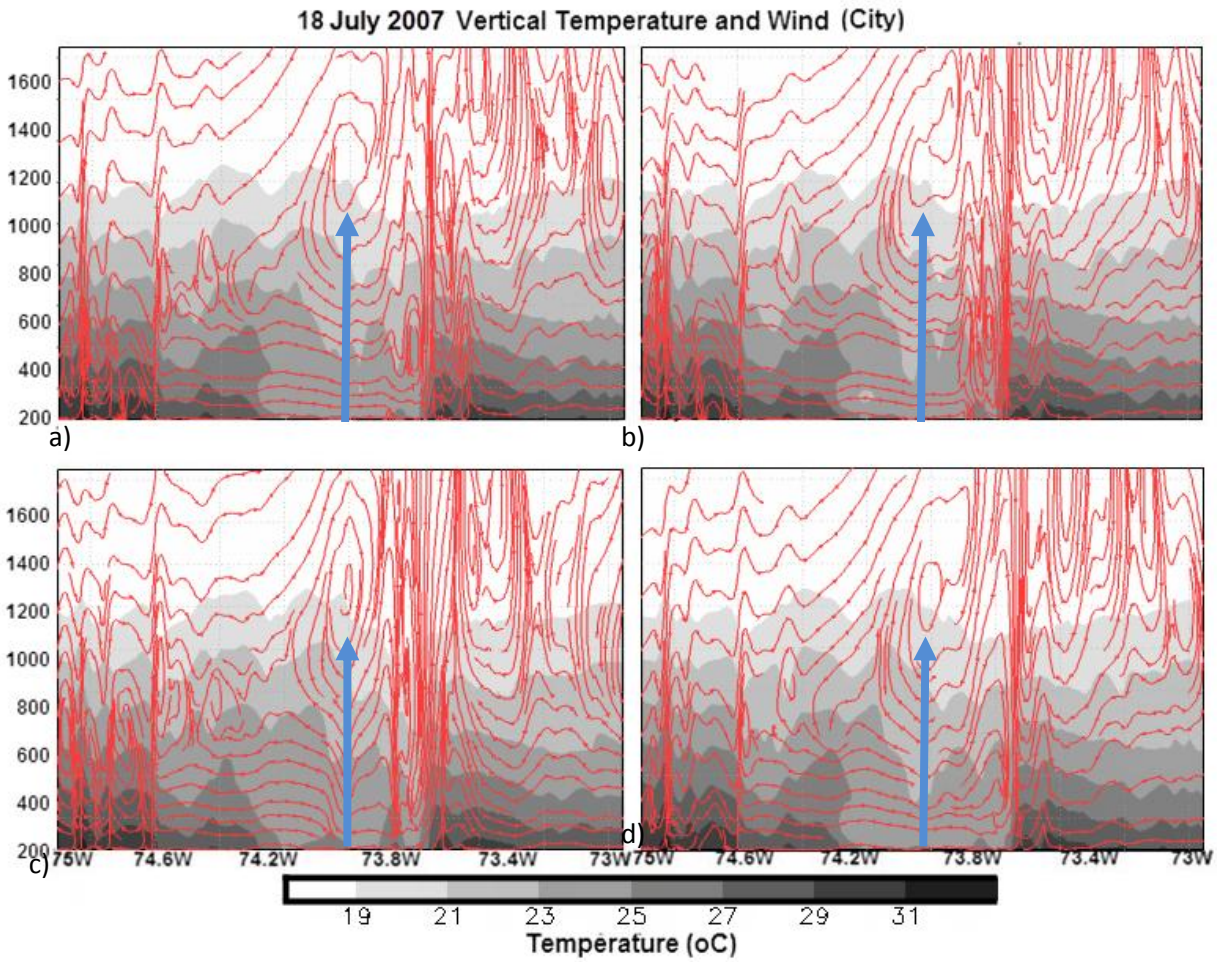

Fig. 60: Vertical temperature and wind for PSD sensitivity cases for the 18 July 2007 regional event. a) Observed PSD (Run 3). b) PSD for 18 July 2007 (Run 2). c) Observed PSD, no coarse mode (Run 11). d) Observed PSD, no fine mode (Run 12). Wind streamlines are for u and w, measured in m s^{-1}. Maximum vertical wind is on the order of 1 m s^{-1}. Blue arrows mark the location of NYC.

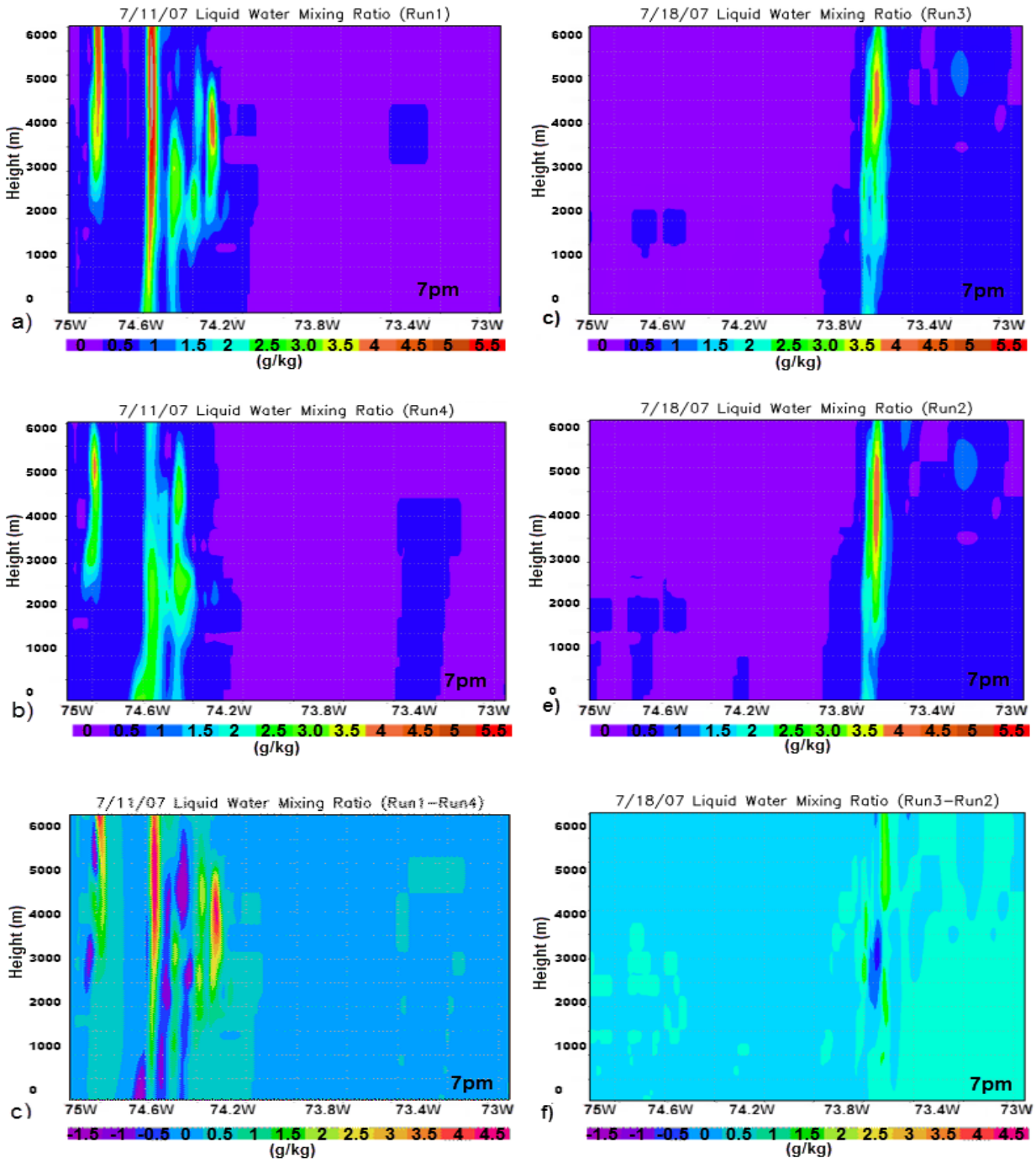

Fig. 61: Liquid Water Mixing Ratio (LWMR) plots through the 40.9N latitude in g/kg. The center of NYC is located at the 73.9W longitude. Heights are in meters. a) LWMR for Run 1. b) LWMR for Run 4. c) LWMR difference (Run 1 minus Run 4). d) LWMR for Run 3. e) LWMR for Run 2. f) LWMR difference (Run 3 minus Run 2).

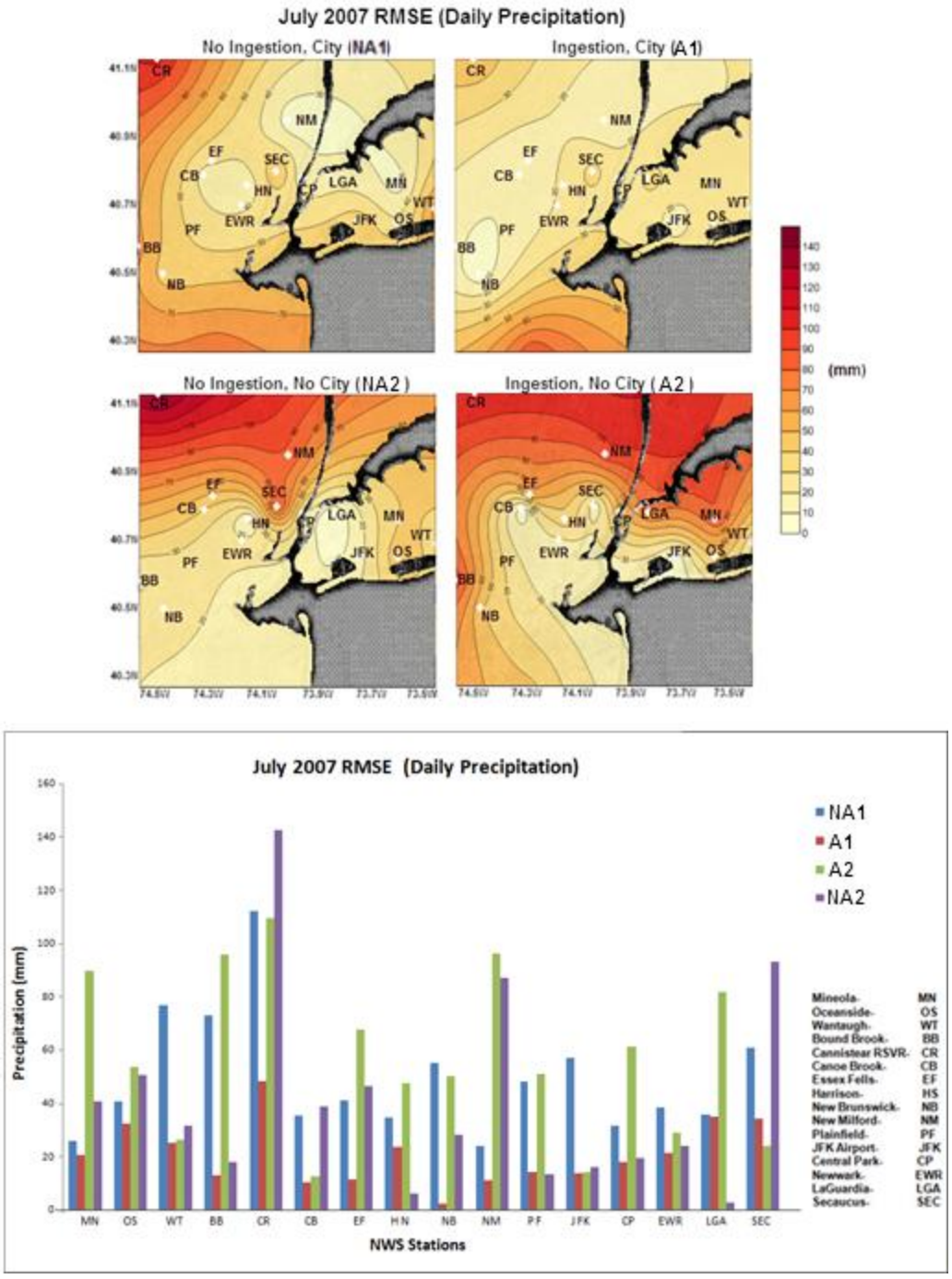

Fig. 62: Accumulated daily precipitation RMSE for NA1 (blue), A1 (red), A2 (green), and NA2 (purple). The spatial plots (top) are attained via interpolation of error at the closest grid point to the model errors. The bar graph (bottom) is representative of actual RMSE values for each simulation over 16 sites.

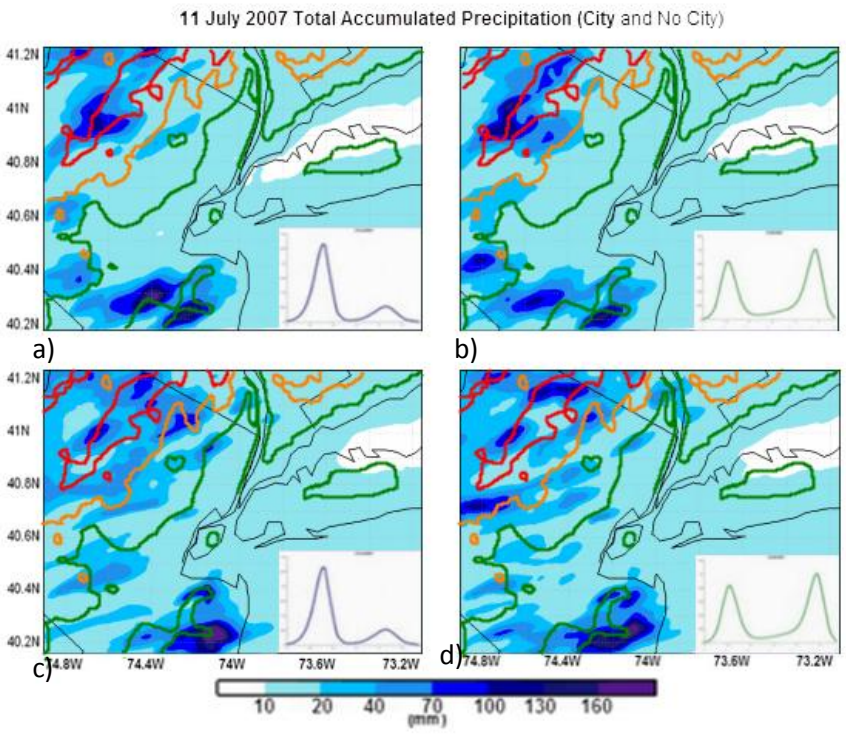

Fig. 63: Total accumulated precipitation for PSD sensitivity cases for the 11 July 2007 event. a) Observed PSD (Run 1). b) PSD for 18 July 2007 (Run 4). c) Observed PSD, No City (Run 5). d) PSD for 18 July 2007, No City (Run 6).

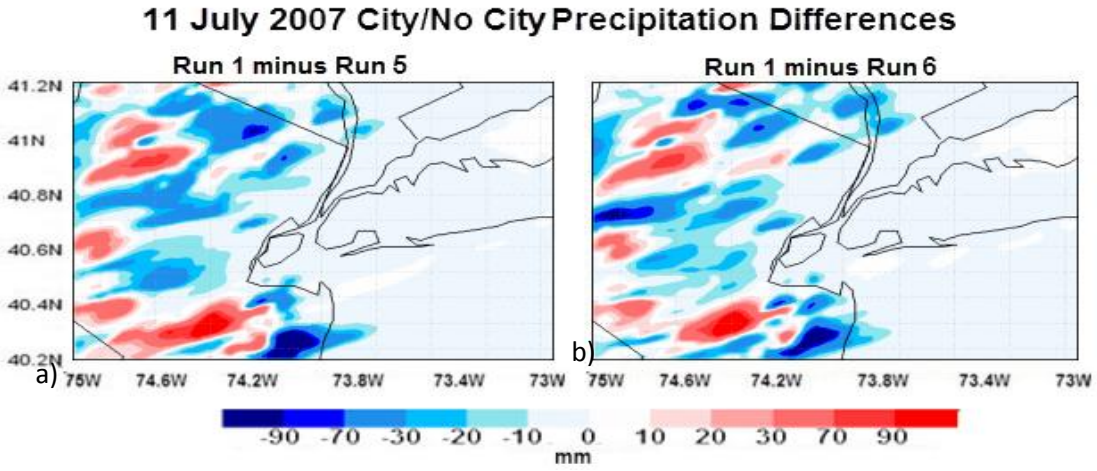

Fig. 64: a) Precipitation differences for Run 1 minus Run 5. b) Precipitation differences for Run 1 minus Run 6.

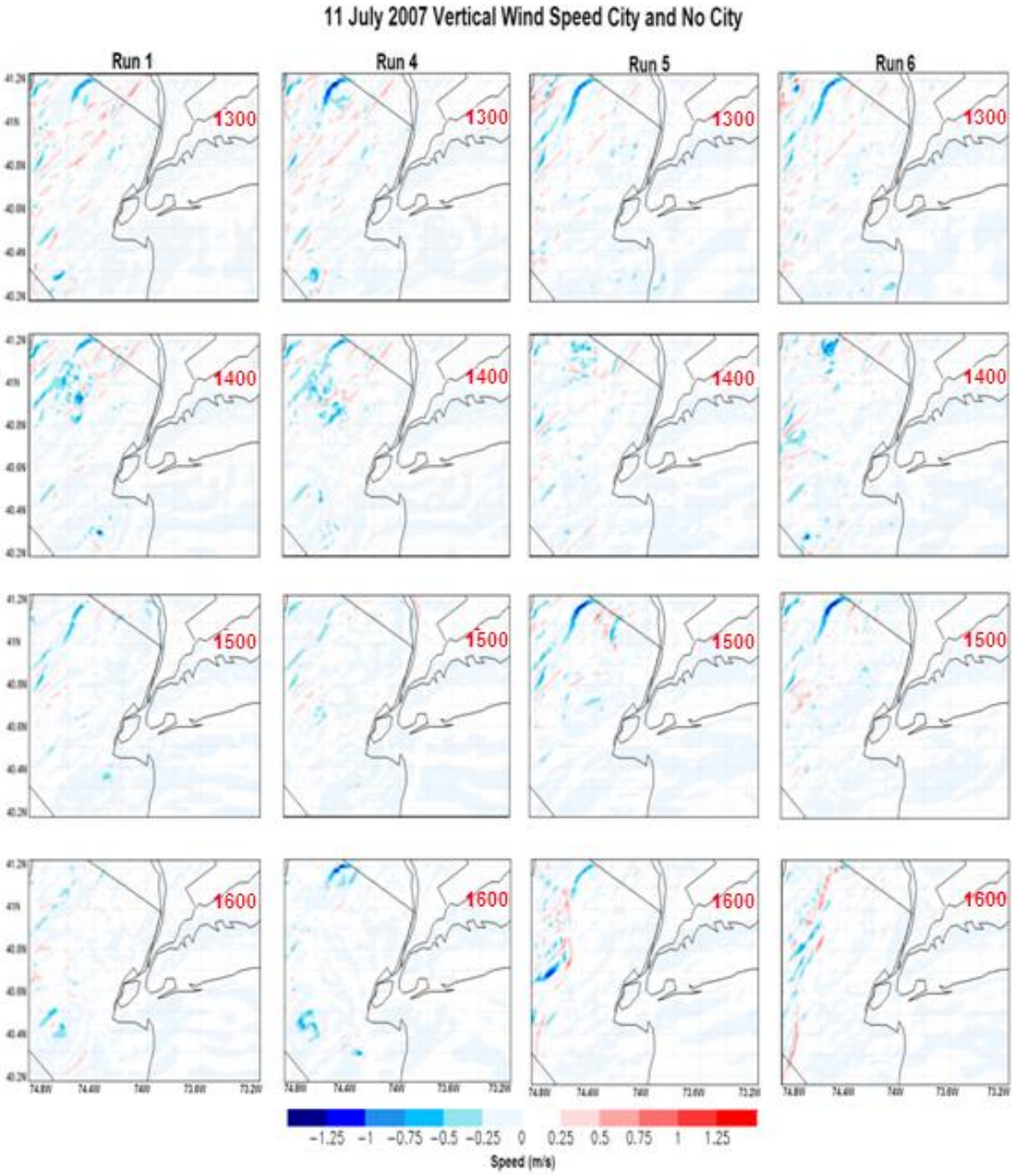

Fig. 65: Vertical wind for 11 July 2007 PSD and LCLU sensitivity cases. a) Observed PSD (Run 1). b) PSD for 18 July 2007 (Run 4). c) Observed PSD, No City (Run 5). d) PSD for 18 July 2007, No City (Run 6). Wind streamlines are for u and w, measured in m s^{-1}. Maximum wind is on the order of +/-1 m s^{-1}.

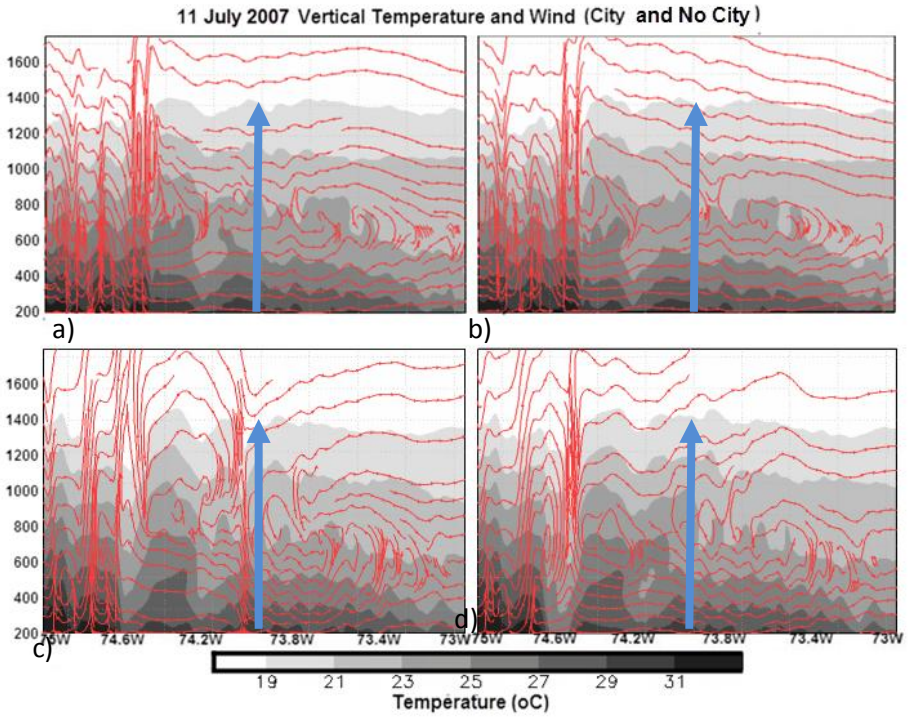

Fig. 66: Vertical temperature and wind for PSD sensitivity cases for the 11 July 2007 localized event. a) Observed PSD (Run 1). b) PSD for 18 July 2007 (Run 4). c) Observed PSD, No City (Run 5). d) PSD for 18 July 2007, No City (Run 6). Wind streamlines are for u and w, measured in m s^{-1}. Maximum vertical wind is on the order of 1 m s^{-1}. Blue arrows mark the location of NYC.

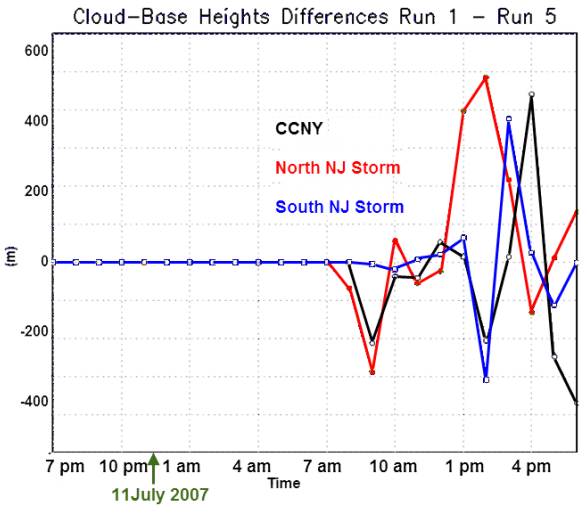

Fig. 67: CBH differences between Run 1 and Run 5 for three different sites.

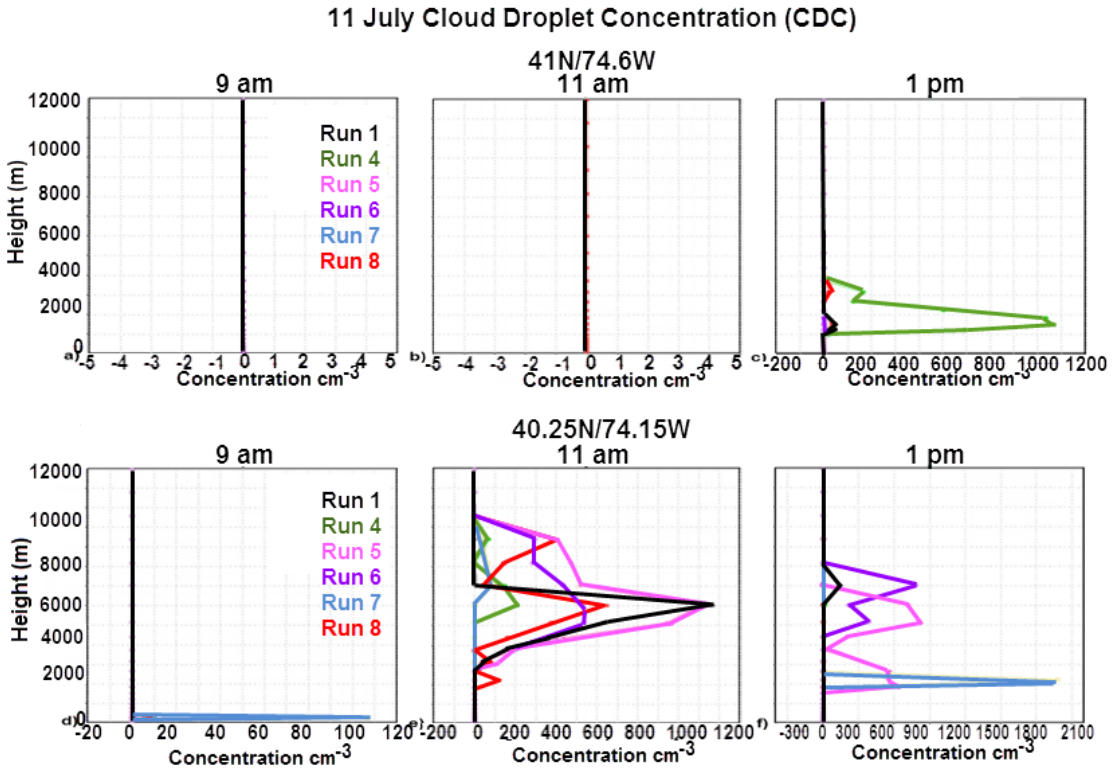

Fig. 68: CDC evolution for two storms during 11 July. Northwestern storm (top) at 4pm, 6pm, and 8pm. Southwestern storm (bottom).

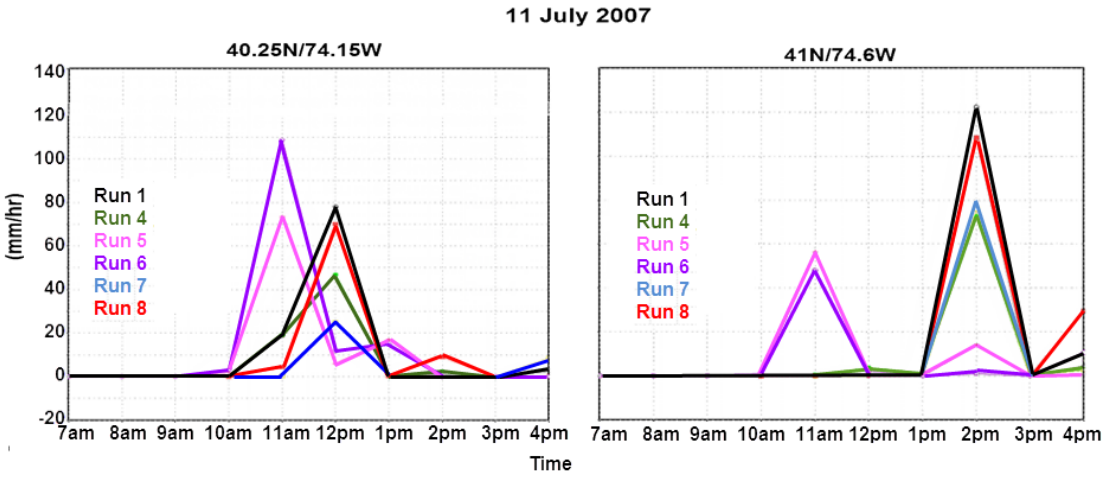

Fig. 69: Precipitation rates for all 11 July simulations for two major storms over NJ, for City and No City cases.

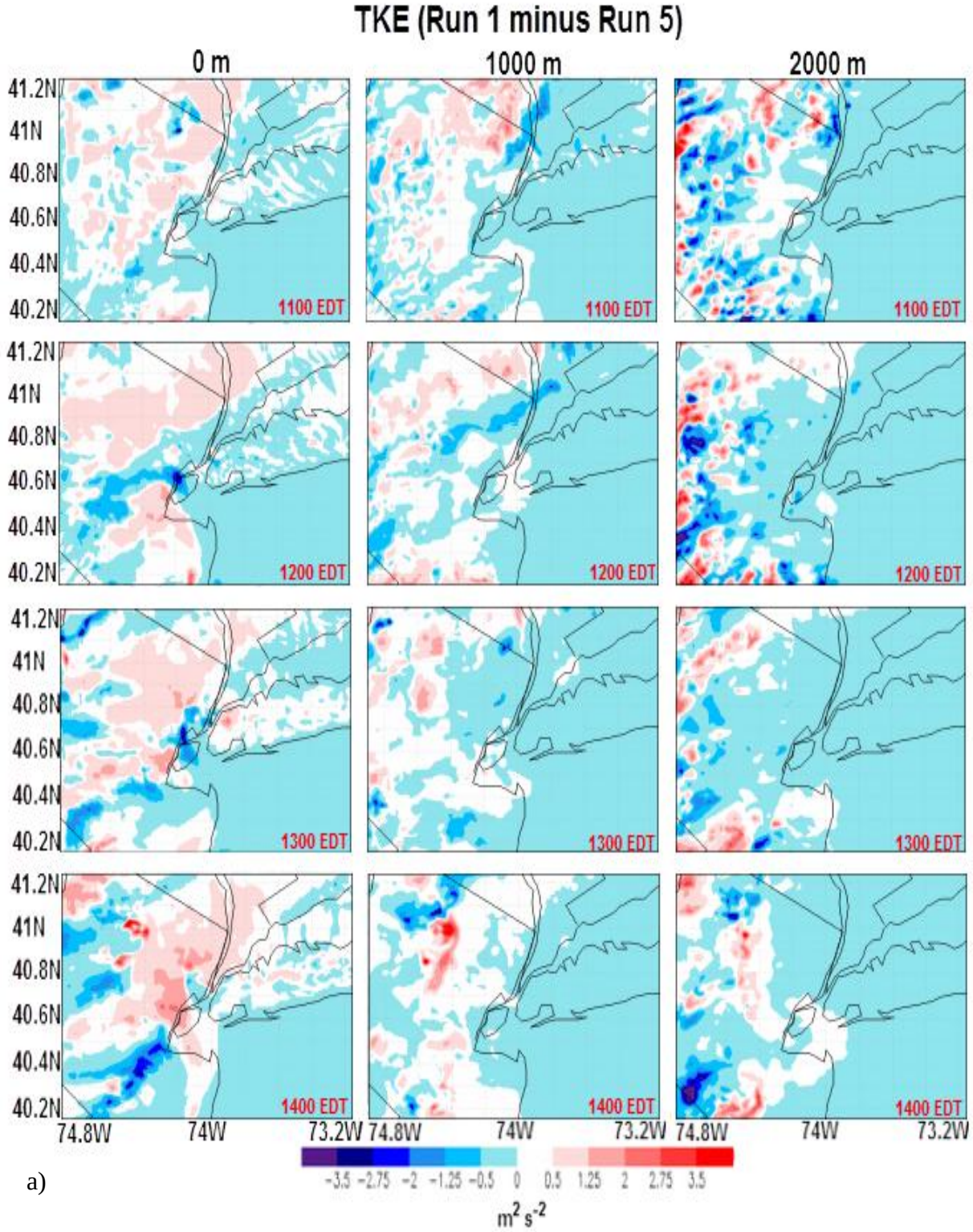
TKE (Run 1 minus Run 5)
0 m
1000 m
2000 m
41.2N
41N
40.8N
40.6N
40.4N
40.2N
1100 EDT
1200 EDT
1300 EDT
1400 EDT
74.8W
74W
73.2W
-3.5 -2.75 -2 -1.25 -0.5 0 0.5 1.25 2 2.75 3.5
m2 s-2

a)

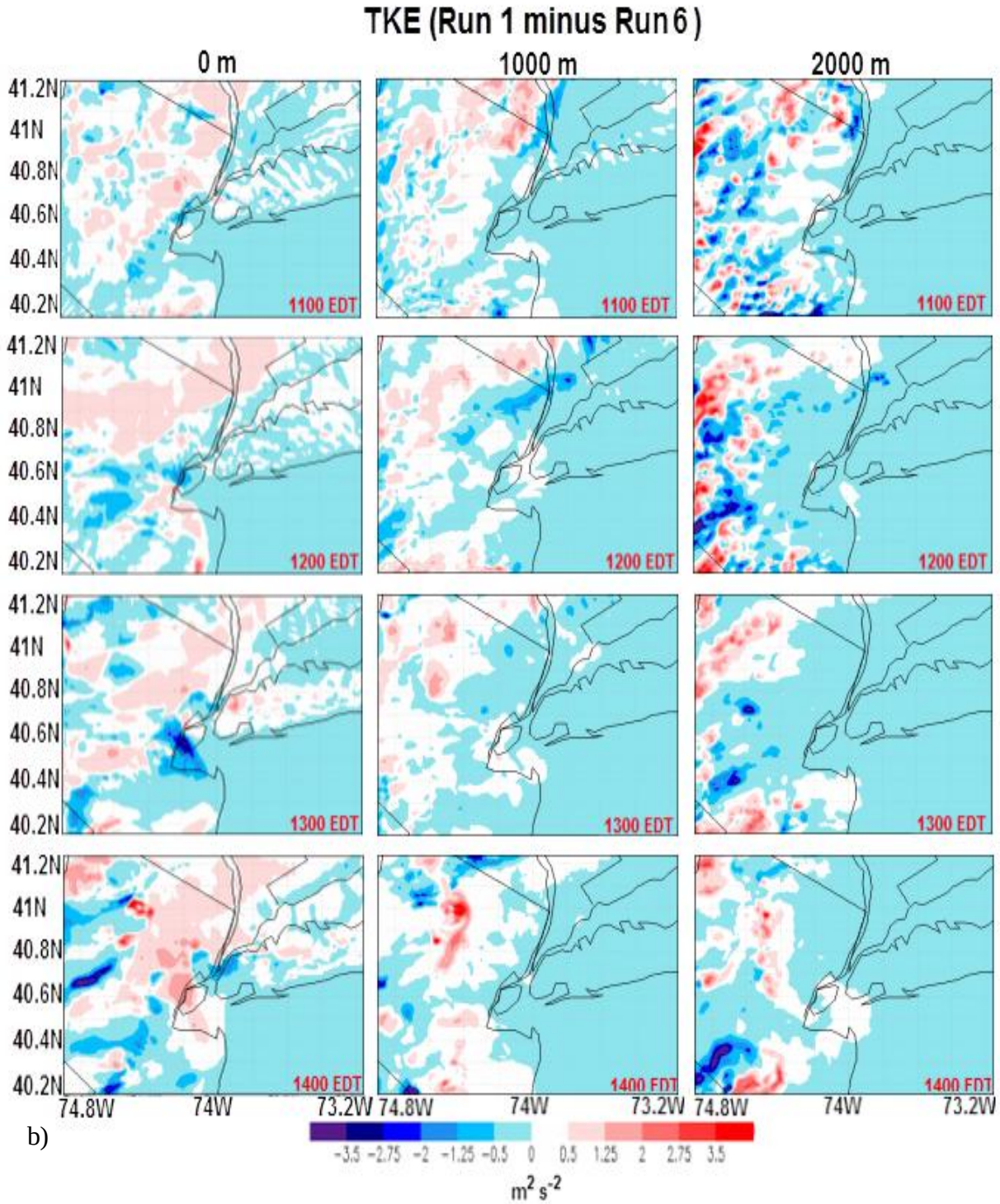

Fig. 70: TKE evolution differences for a) Run 1 (City) minus Run 5 (No City) at three elevations including 0 m, 1000 m, and 2000 m and b) Run 1 (City) minus Run 6 (No City) at three elevations including 0 m, 1000 m, and 2000 m.

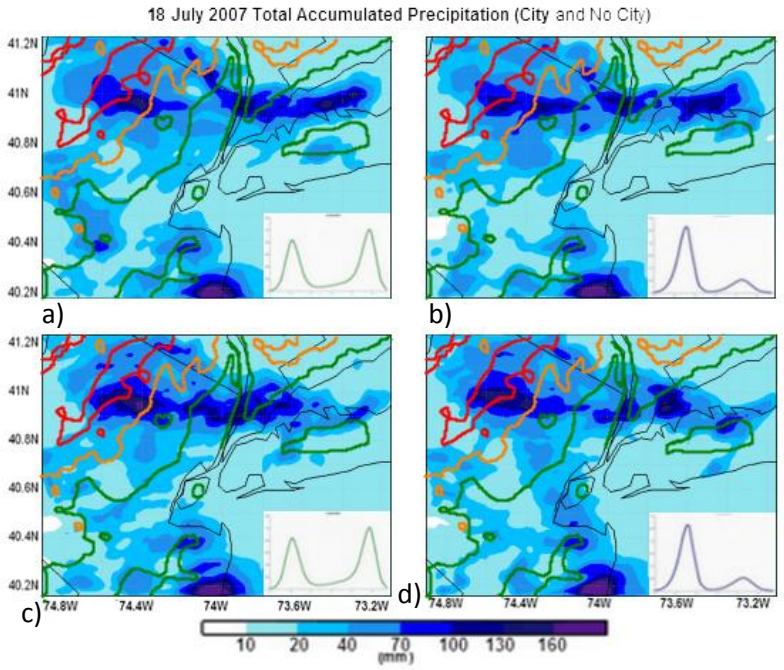

Fig. 71: PSD sensitivity cases for the 18 July 2007 mesoscale event. a) PSD for 11 July 2007 (Run 2). b) Observed PSD for 18 July 2007 (Run 3). c) Observed PSD, No City (Run 9). d) PSD for 11 July 2007, No City (Run 10).

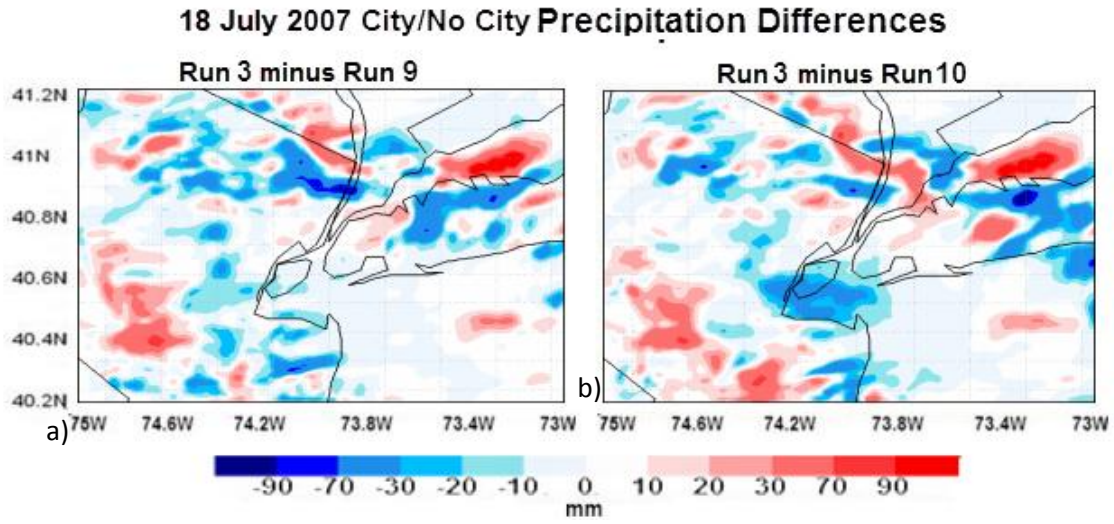

Fig. 72: a) Precipitation differences for Run 3 (City) minus Run 9 (No City). b) Precipitation differences for Run 3 minus Run 10 (No City).

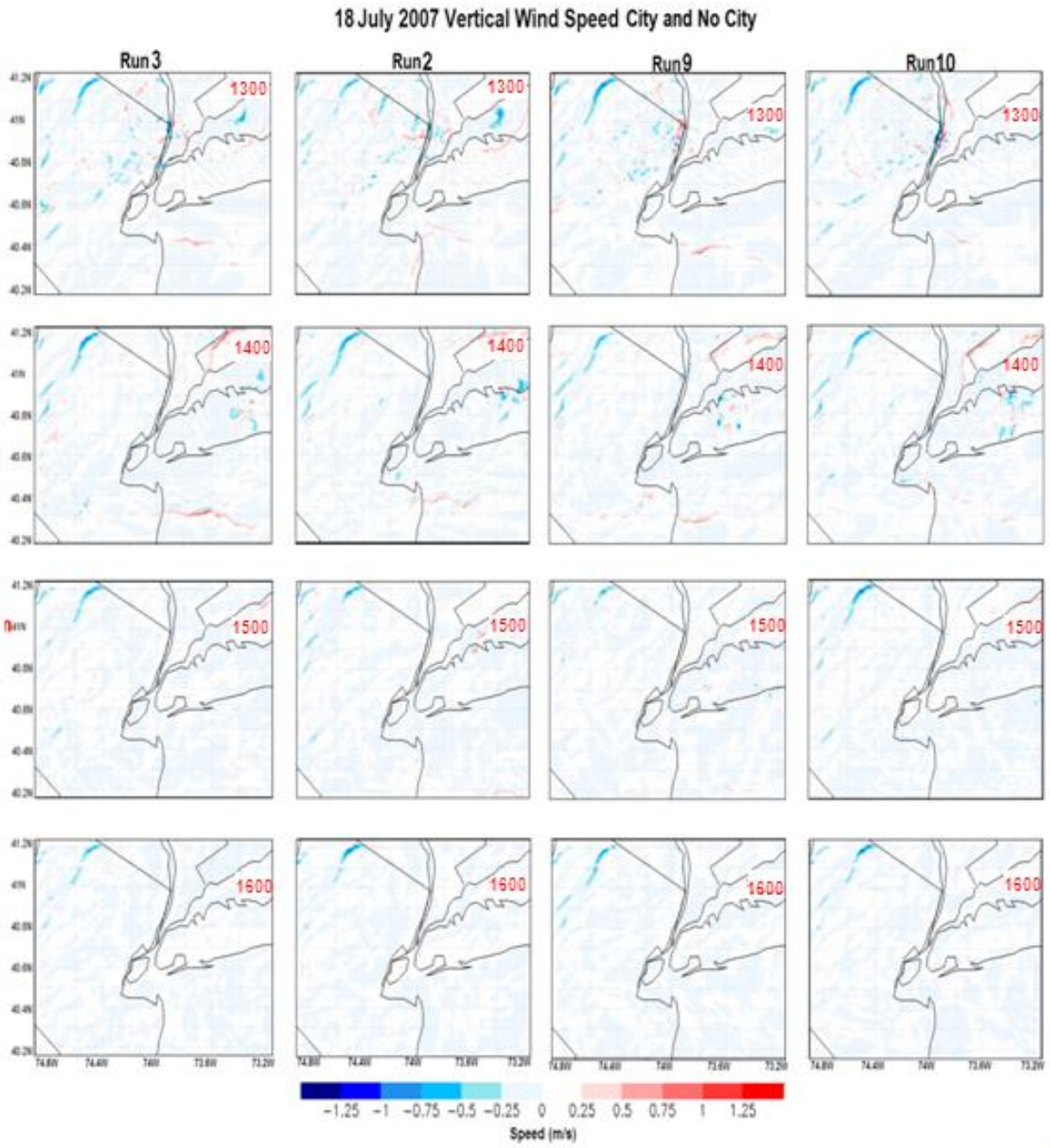

Fig. 73: Vertical wind for PSD and LCLU sensitivity cases for the 18 July 2007 mesoscale event. a) PSD for 11 July 2007 (Run 2). b) Observed PSD for 18 July 2007 (Run 3). c) Observed PSD, No City (Run 9). d) PSD for 11 July 2007, No City (Run 10). Maximum wind is on the order of +/- 1 m s^{-1}.

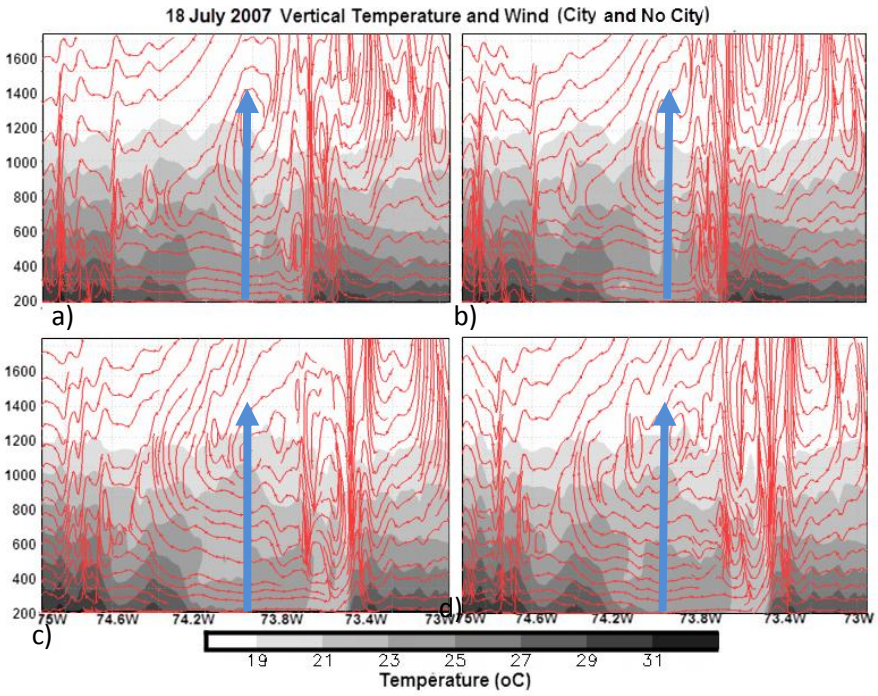

Fig. 74: Vertical temperature and wind for PSD sensitivity cases for the 18 July 2007 mesoscale event. a) PSD for 11 July 2007 (Run 2). b) Observed PSD for 18 July 2007 (Run 3). c) Observed PSD, No City (Run 9). d) PSD for 11 July 2007, No City (Run 10). Wind streamlines are for u and w, measured in m s^{-1}. Maximum vertical wind is on the order of 1 m s^{-1}. Blue arrows mark the location of NYC.

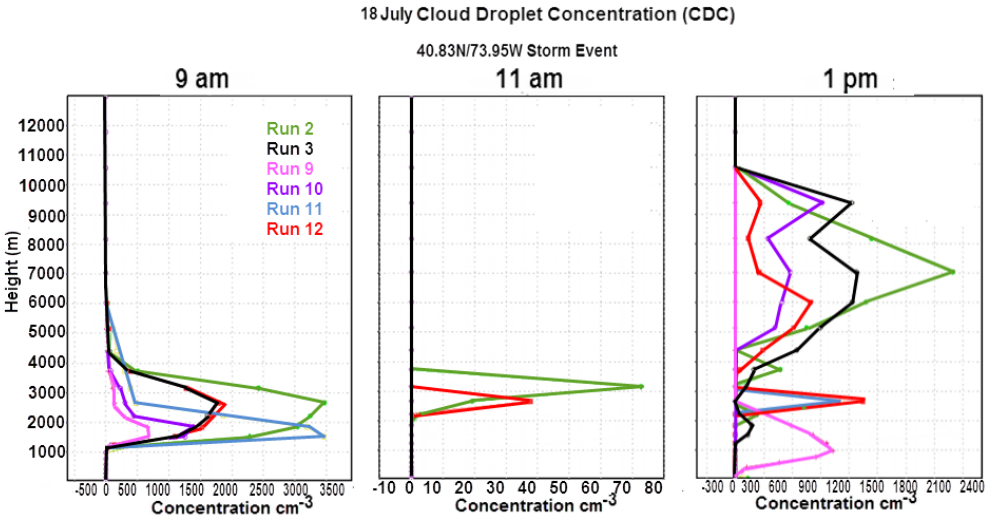

Fig. 75: CDC evolution over NYC during 18 July at 4pm, 6pm, and 8pm.

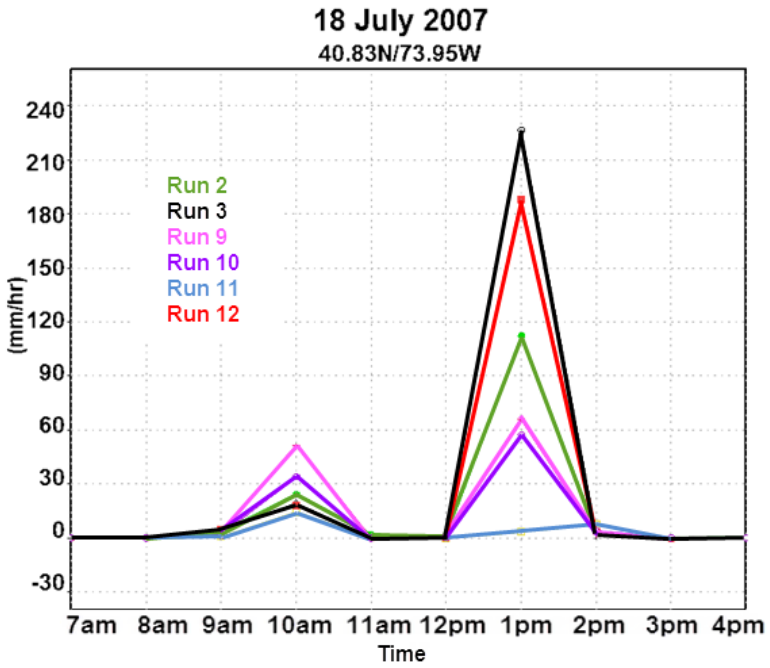

Fig. 76: Precipitation rates for all 18 July simulations for NYC.

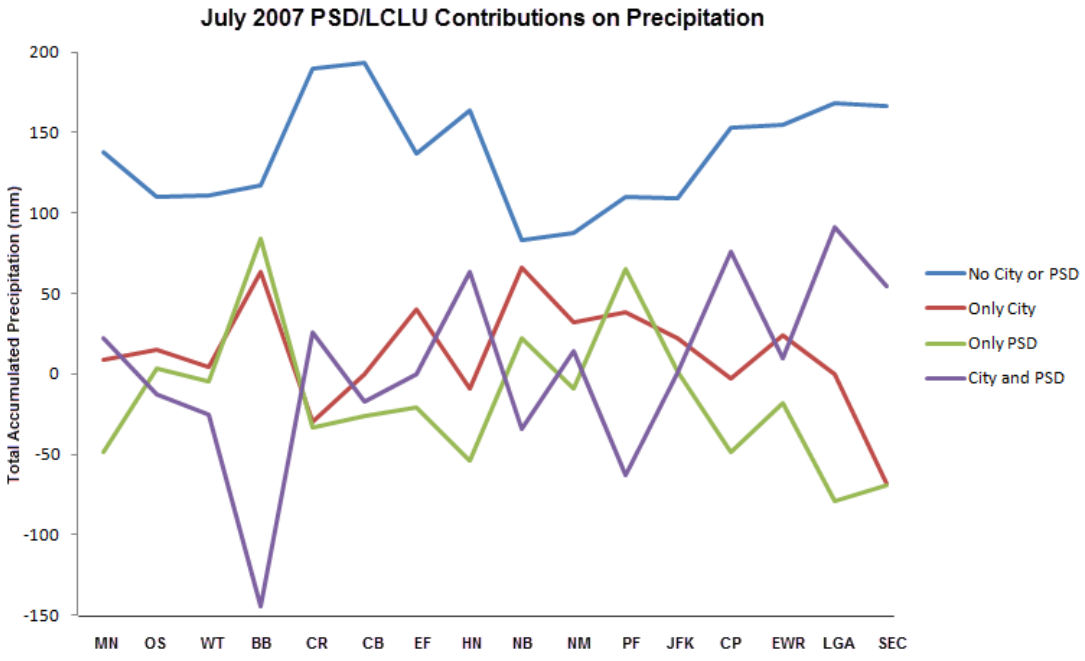

Fig. 77: PSD/LCLU contributions on precipitation.

Chapter 5

Summary, Conclusion, and Future Work

5.1 Summary and Conclusion

The aim of this research was to investigate the role of PSD and LCLU on storms over and near complex urban environments such as NYC. PSDs/LCLU obtained from AERONET/NLCD were ingested/assimilated into RAMS and precipitation results for all cases were compared. Results show that monthly precipitation forecasting is improved when observed PSDs and present LCLU is ingested/assimilated. For 12 of 16 different sites, runs with observed PSD/present LCLU show reduced error over runs that did not have either observed PSD updates, or current LCLU. Previous studies have shown that variation in aerosol concentrations taken from observations impacts precipitation amounts, rates, and spatial orientation (Ntelekos et al. 2009; Fan et al. 2012), and that ingestion of observed PSD from handheld radiometers into cloud resolving models has improved precipitation estimates (Comarazamy et al. 2006). This thesis represents the first time that AERONET PSDs have been shown to improve precipitation estimates in a complex coastal urban environment when ingested into a cloud resolving model such as RAMS.

In addition to the monthly experiments, 12 experiments for two different daily precipitation events were investigated with RAMS to study the role PSD and LCLU play in local and regional precipitation events. For both storms, varied PSDs and LCLUs were ingested into RAMS. Results show that the presence of the city acts to suppress precipitation over NYC. Results show that HVFM PSD suppresses precipitation, while HVCM PSD enhances

accumulated precipitation totals. Spatial precipitation patterns also change. These PSD effects are attributed to hastened/reduced rates of autoconversion due to the presence of higher volumes of GCCN/CCN (reduced GCCN number concentration can result in increased GCCN volume when the modal radii is large as is the case in 18 July 2007), which enhances/impedes droplet coalescence rates, in agreement with observational work regarding pollution tracks over Turkey, Canada, and Australia (Rosenfeld 2000), work on convective storms over the tropical environment of Puerto Rico (Comarazamy et al. 2006), and a conceptual cloud physics frame work (Rosenfeld et al. 2008).

Results also show that urban effects and LCLU provides the dominant forcing for precipitation modification, and then PSD variation, in agreement with studies of convective storms over and downwind of St. Louis (van den Heever and Cotton 2007), and the synthesis of urban effects based on the ideas of Bornstein (2011) but created by Grimmond (2011) and Shepherd (2011), which was presented in Chapter 2 (Fig. 7). Analysis of CBH differences show that added convection induced by the presence of urban LCLU elevates the CBH. These results provide further support that the presence of the city impacts precipitation, elevating aerosols higher into the atmosphere via the added convection, and modified surface to atmosphere interactions, including TKE. Deviation from observed accumulated precipitation results are higher in No City cases than in City cases. Where wind, UHI, and convergence/divergence primarily affect the formation and path of storms, aerosols affect storms after their initial formation. CNN can cause invigoration or suppression due to delayed autoconversion, while GCCN can increase precipitation intensity and accumulation.

In summary, RAMS simulations for the urban environment of NYC were conducted in order to quantify the effect of varying aerosol PSD and LCLU on model precipitation results.

Results show that precipitation results are closer to NWS observations when observed PSD obtained from AERONET is ingested in conjunction with LCLU assimilated from NLCD, and that precipitation amounts and spatial patterns are sensitive to PSD modification. This research was limited in that observed PSD from a single site (CCNY) was ingested for the entire domain. In order to further investigate PSD variations, it will be necessary to ingest varying PSD at multiple locations. In addition, vertical variation in aerosol concentrations will improve representation of PSD over a given region. This work opens up many possibilities in the area of prediction and forecasting of weather events. In the instances where PSD is available from AERONET or similar sources, modification of a cloud resolving model's microphysics via assimilation of real data can improve precipitation estimates. If data is not available for a specific time, it may be beneficial to use PSD averages based on past aerosol climatology. The author's approach to advancing the present understanding of PSD in precipitation systems will be presented in the following section.

5.2 Future Work

5.2.1 PSD and LIDAR

LIDAR at CCNY has been used to obtain aerosol extinction-to-backscatter ratio (Gross et al. 2009, Fig.78); a parameter used for inversion of LIDAR signals so that cloud droplets may be visualized. This information may be used to explore precipitation prediction using cloud-aerosol models and parameterizations. For example, a number of parameterized models estimate

concentration and PSD of cloud droplets given the updraft velocity and number of CCN in the vertical column. It may be possible to combine this vertical PSD with the horizontal PSD attained from AERONET to attain a 3D map of the aerosol field. The goal is to determine how PSDs vary in space and time. It may also be possible to extract this information by using the multispectral extinction from AERONET after it is run through an inversion algorithm. LIDAR may then be used to create a homogenous vertical probability envelope distribution. The author is not aware of any work that has used this methodology in the literature.

5.2.2 PSD Over Two Regions

The PSD effects on regions other than NYC should also be investigated. NYC is unique in that it is within proximity of the Atlantic Ocean, with the Hudson and East Rivers separating Manhattan from Queens, Brooklyn, Staten Island, and The Bronx. U.S. Cities that are far from bodies of water as large as the Atlantic Ocean may have vastly different responses to PSD modification (Phoenix, Atlanta, Las Vegas, and Orlando). Some proposed areas to research outside of the contiguous U.S. are listed following this paragraph.

The Caribbean (10N – 20N, 60W -88W) is subjected to intrusion of Saharan Dust (SD) between the months of May and August which suppresses rainfall during the midsummer season (Comarazamy and González 2008; Doherty et al. 2008; Angeles et al. 2010). Islands such as Puerto Rico, with multiple mesonet networks such as AERONET and ceilometers sites allow for the attainment of spatially varying PSD and in depth analysis of localized convective events impacted by the SD. Linfen, in the Shanxi Province of China (36.08N, 111.52E), is at the center

of the coal industry. Here, emissions from vehicles and industry have created an atmosphere where people literally choke on coal dust. Work by Das (2008) showed evidence that seasonal and regional variability of aerosol mass concentration had a considerable influence on aerosol effects. Shen et al. (2007) suggests that these aerosol effects inhibit rainfall production, and have led to extreme drought events as a result.

5.2.3 Cloud Resolving Models

Atmospheric mesoscale models such as RAMS and WRF have come a long way, but still have ways to go concerning precipitation prediction. The inclusion of spatially varying aerosol PSD and concentration in RAMS is currently being explored. This may further improve the accuracy of weather predictions. The ultimate goal would be to assimilate gridded aerosol PSD data from geostationary satellites such as GOES-East (currently orbiting the planet) and GOES-R (to be launched in 2015) into the model as data becomes available. Since PSD from GOES satellites is not yet available, they must be derived via AOT products using an algorithm similar to the one used bin this work by Dubovik and King (2000) . Another way to possibly improve model performance is investigate the assimilation of higher resolution spatial and temporal boundary conditions.

Precipitation lag, the phenomenon in which model results lag observations by six or more hours may be reduced by analysis nudging at reduced update intervals. For the present study, NCEP reanalysis data was updated every six hours. As shown in the temperature and precipitation validation plots of Chapter 4, simulation results lag observations by 6 hours,

consistent with results by Comarazamy et al. 2006. It may also be beneficial to assimilate North American Mesoscale (NAM) data 4 times per day at 12 km resolution (http://www.ncdc.noaa.gov/model-data/north-american-mesoscale-forecast-system-nam). NAM is one of the major weather models run by the NCEP for producing weather forecasts. Dozens of weather parameters are available from the NAM grids, from temperature and precipitation to lightning and TKE. The NAM model generates multiple grids of weather forecasts over the North American continent at various horizontal resolutions. The Continental United States (CONUS), 12 km resolution, gridded data are available for download through NOMADS. Another option is the North American Regional Reanalysis (NARR). The NARR project is an extension of the NCEP Global Reanalysis which is run over the North American Region. NARR provides 32 km spatial resolution data at 29 vertical levels at eight times daily temporal resolution. Rerunning some of the simulations described in this document with NARR or NAM data may reveal the importance of boundary condition resolution and update frequency in RAMS.

5.2.4 The Plan Going Forward

Changing climate and increased hurricane intensity impact lives, property and livelihoods negatively throughout the Caribbean region. Figure 79 shows the results for precipitation changes over the Caribbean for the multi model data (MMD)-A1B energy scenario. The A1B represents balanced energy across different energy sources (IPCC 2007). The author will use the tools gained from the present research to investigate the effects of PSD modification on

precipitation and climate over the Caribbean. The Caribbean is of interest because aerosol cloud interactions are well documented in the tropics (Lau et al. 2009), aerosol data for cloud resolving models such as PSD via AERONET and LIDAR is available, researchers can focus on warm season precipitation, and there are a high number of extreme precipitation events over the islands that have been well documented. The Caribbean also lies in the path of the SD plume, which plays a crucial role in modulating the seasonal variability of rainfall over the region (Jury 2009).

The aim going forward is first to analyze the influence of PSD (specifically SD) on Caribbean precipitation systems. In order to zoom in on PSD effects on storms over the region, horizontal PSD from the AERONET site will be coupled with vertical PSD attained from a ceilometer and or LIDAR to obtain the three-dimensional (3D) aerosol structure in the local atmosphere. This 3D PSD is to be ingested into a cloud resolving model such as RAMS, and can be modified to determine the effect of PSD changes on precipitation in the tropics. Although there are many AERONET sites over the Caribbean, PSD data is not robust over every island. It is important to find ways to attain more data. Since PSD is derived from inversion of AOT, researchers may translate satellite borne AOT info into a gridded PSD product for assimilation into cloud resolving models. Satellite AOT has been used to track major natural events including Amazon mass burning, and the SD intrusion. Once the satellite PSD product is available, the author will test the assimilation of gridded satellite PSD into a cloud resolving model for the specific case of Puerto Rico, where a wealth of data is available from AERONET stations, LIDAR (http://ece.uprm.edu/noaa-crest/index.php), ceilometers, and NOAA/NWS NEXRAD.

Rainfall over the island of Puerto Rico is heavily influenced by local dynamical systems associated with orographic cloud formation over the highest central mountains and convective

clouds formed by coastal convergence (Comarazamy and González 2008). These effects may largely contribute to the total annual precipitation during the dry and early rainfall seasons (Dec-July). The west coast of the island is subjected to convergence episodes between the easterly trade winds and a westerly sea-breeze which frequently initiate strong afternoon showers when coupled with surface heating (Jury 2009). Variation in the concentration of aerosols due to the SD intrusion has also influenced rainfall across the island. Records for PSDs and precipitation over Puerto Rico indicate strong correlation between high aerosol concentrations and precipitation suppression during the drier summer season (Comarazamy et al. 2006). The proposed future work has the potential of providing further insight of the effect of PSD on precipitation in a tropical environment.

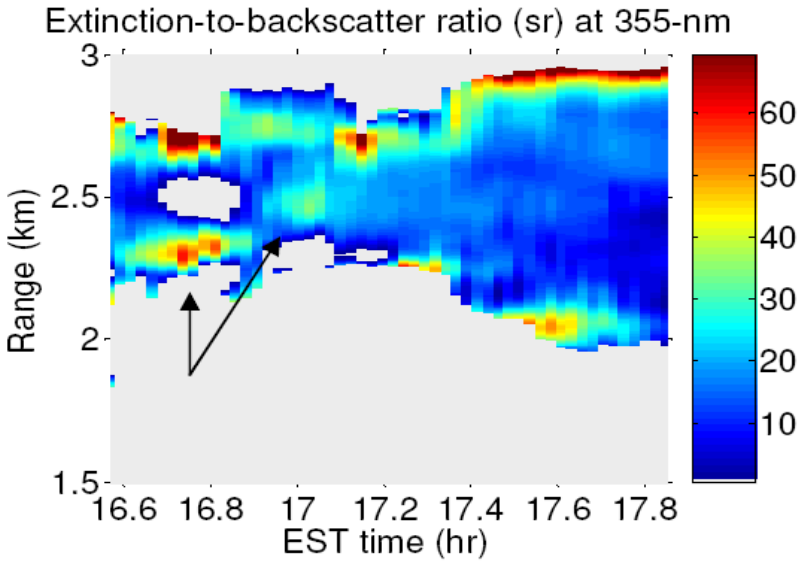

Fig. 78: Extinction to backscatter ratio in a cloud showing small droplets (Gross 2009).

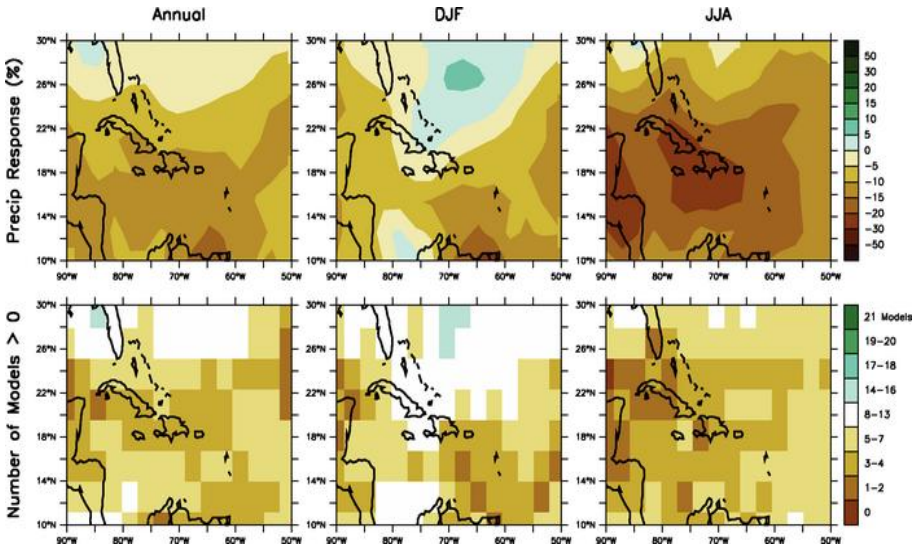

Fig. 79: Precipitation changes over the Caribbean from the MMD-A1B simulations. Top row: Annual mean, DJF (December, January and February) and JJA (June, July, and August) fractional precipitation change between 1980 to 1999 and 2080 to 2099, averaged over 21 models. Bottom row: number of models out of 21 that project increases in precipitation. (IPCC, 2007)

Appendix

Root Mean Square Error (RMSE)

The root-mean-square error (RMSE) is a frequently used measure of the differences between values predicted by a model or an estimator and the values actually observed. The RMSE serves to aggregate the magnitudes of the errors in predictions for various times into a single measure of predictive power (Lehmann and Casella 1998). RMSE is a good measure of accuracy, but only to compare forecasting errors of different models for a particular variable and not between variables. The RMSE of a model prediction with respect to the estimated variable X_{model} is defined as the square root of the mean squared error:

$$RMSE = \sqrt{\frac{\sum_{i=1}^{n} (X_{obs,i} - X_{model,i})^2}{n}}$$

where X_{obs} represents observed values and X_{model} modeled values at particular time and place i. RMSE values have units, and can be used to distinguish model performance in a calibration period with that of a validation period.

Statistical Significance

Statistical significance is a statistical assessment of whether observations reflect a pattern rather than just chance. With sufficient data, a statistically significant result may be very small in magnitude. A two-tailed test is a statistical procedure used to compare the null hypothesis that a

parameter is equal to a particular value against the alternative hypothesis that the parameter is different from this value. Evidence regarding the null hypothesis is obtained from a test statistic, and the test is said to be "two-tailed" since its alternative hypothesis does not specify whether the parameter is greater than or less than the value specified by the null hypothesis. Values on both tails of its distribution provide evidence against the null hypothesis. This type of test is relevant for situations in which researchers wish to test a null hypothesis but do not have a prior belief about the direction of the alternative, a situation which is likely to happen in practice.

Null hypotheses represent theories that are believed to be true but have not been proved. The final conclusion once the test has been carried out is always given in terms of the null hypothesis. The researcher may then reject the null hypothesis or not reject the null hypothesis. The significance level α for a given hypothesis test is a value for which a P-value less than or equal to α is considered statistically significant. Typical values for α are 0.1, 0.05, and 0.01. For a two-sided test, we are interested in the probability that $2P(Z \geq z^*) = \alpha$, so the critical value z^* corresponds to the $\alpha/2$ significance level. To achieve a significance level of 0.05 for a two-sided test, the absolute value of the test statistic ($|z|$) must be greater than or equal to the critical value 1.96 (which corresponds to the level 0.025 for a one-sided test).

Another interpretation of the significance level is that it corresponds to the value for which one chooses to reject or accept the null hypothesis. The probability of a Type I error is equal to the significance level α, and the probability of rejecting the null hypothesis when it is in fact false (a correct decision) is equal to 1 - α. To minimize the probability of Type I error, the significance level is generally chosen to be small.

LCLU Tables

Table App1: NLCD 2006 Land classes and their properties.

Source: http://www.mrlc.gov/nlcd06_leg.php

Class\ Value	Classification Description
Water	*areas of open water or permanent ice/snow cover.*
11	**Open Water** - areas of open water, generally with less than 25% cover of vegetation or soil.
12	**Perennial Ice/Snow** - areas characterized by a perennial cover of ice and/or snow, generally greater than 25% of total cover.
Developed	*areas characterized by a high percentage (30% or greater) of constructed materials (e.g. asphalt, concrete, buildings, etc.).*
21	**Developed, Open Space** - areas with a mixture of some constructed materials, but mostly vegetation in the form of lawn grasses. Impervious surfaces account for less than 20% of total cover.
22	**Developed, Low Intensity** - areas with a mixture of constructed materials and vegetation. Impervious surfaces account for 20% to 49% percent of total cover. These areas most commonly include single-family housing units.
23	**Developed, Medium Intensity** – areas with a mixture of constructed materials and vegetation. Impervious surfaces account for 50% to 79% of the total cover. These areas most commonly include single-family housing units.
24	**Developed High Intensity** -highly developed areas where people reside or work in high numbers including apartment complexes, row houses and commercial/industrial. Impervious surfaces account for 80% to 100% of the total cover.
Barren	*areas characterized by bare rock, gravel, sand, silt, clay, or other earthen material, with little or no "green" vegetation present regardless of its inherent ability to support life.*
31	**Barren Land (Rock/Sand/Clay)** - areas of bedrock, desert pavement, scarps, talus, slides, volcanic material, glacial debris, sand dunes, strip mines, gravel pits and other accumulations of earthen material. Generally, vegetation accounts for less than 15% of total cover.
Forest	*areas characterized by tree cover (natural or semi-natural woody vegetation, generally greater than 6 meters tall); tree canopy accounts for 25% to 100% of the cover.*
41	**Deciduous Forest** - areas dominated by trees generally greater than 5 meters tall, and greater than 20% of total vegetation cover. More than 75% of the tree species shed foliage simultaneously in response to seasonal change.
42	**Evergreen Forest** - dominated by trees greater than 5 meters tall, and greater than 20% of total vegetation cover. More than 75% of the trees maintain their leaves all year. Canopy is never without green foliage.
43	**Mixed Forest** - dominated by trees generally greater than 5 meters tall, and greater than 20% of total vegetation cover. Neither deciduous nor evergreen species are greater than

	75% of total tree cover.
Shrubland	*woody vegetation with aerial stems, less than 6 meters tall, with individuals or clumps not touching. Both evergreen and deciduous species of true shrubs, young trees, and trees or shrubs that are small or stunted because of environmental conditions are included.*.
51	**Dwarf Scrub** - Alaska only. Shrubs less than 20 centimeters tall with shrub canopy typically greater than 20% of total vegetation. Often co-associated with grasses, sedges, herbs, and non-vascular vegetation.
52	**Shrub/Scrub** - Dominated by shrubs; less than 5 meters tall with shrub canopy typically greater than 20% of total vegetation. Includes true shrubs, and trees stunted from environmental conditions.
Herbaceous	*areas characterized by natural or semi-natural herbaceous vegetation; herbaceous vegetation accounts for 75% to 100% of the cover.*
71	**Grassland/Herbaceous** - Dominated by gramanoid or herbaceous vegetation, generally greater than 80% of total vegetation. Not subject to intensive tilling, but can be utilized for grazing.
72	**Sedge/Herbaceous** - Alaska only areas dominated by sedges and forbs, generally greater than 80% of total vegetation. This type can occur with significant other grasses or other grass like plants, and includes sedge tundra, and sedge tussock tundra.
73	**Lichens** - Alaska only areas dominated by fruticose or foliose lichens generally greater than 80% of total vegetation.
74	**Moss** - Alaska only areas dominated by mosses, generally greater than 80% of total vegetation.
Planted/Cultivated	*areas characterized by herbaceous vegetation that has been planted or is intensively managed for the production of food, feed, or fiber; or is maintained in developed settings for specific purposes. Herbaceous vegetation accounts for 75% to 100% of the cover.*
81	**Pasture/Hay** – areas of grasses, legumes, or grass-legume mixtures planted for livestock grazing or the production of seed or hay crops, typically on a perennial cycle. Pasture/hay vegetation accounts for greater than 20% of total vegetation.
82	**Cultivated Crops** – areas used for the production of annual crops, such as corn, soybeans, vegetables, tobacco, and cotton, and also perennial woody crops such as orchards and vineyards. Crop vegetation accounts for greater than 20% of total vegetation.
Wetlands	*areas where the soil or substrate is periodically saturated with or covered with water.*
90	**Woody Wetlands** - areas where forest or shrubland vegetation accounts for greater than 20% of vegetative cover and the soil or substrate is periodically saturated with or covered with water.
95	**Emergent Herbaceous Wetlands** - Areas where perennial herbaceous vegetation accounts for greater than 80% of vegetative cover and the soil or substrate is periodically saturated with or covered with water.

Table App2: LEAF-3 land designations and properties.

Alb green	Alb brown	emiss	sr max	Tai_ max	sai	Veg clump	Veg frac	Veg ht	Root dep	Dead frac	Rc min	LEAF-3 Class
.00	.00	.00	.00	.00	.00	.00	.00	.00	.00	.00	0	0 Ocean
.00	.00	.00	.00	.00	.00	.00	.00	.00	.00	.00	0	1 Lakes, rivers
.00	.00	.00	.00	.00	.00	.00	.00	.00	.00	.00	0	2 Icecap
.00	.00	.00	.00	.00	.00	.00	.00	.00	.00	.00	0	3 Desert
.14	.24	.97	5.4	8.0	1.0	1.0	.80	20.0	1.5	.0	500	4 Evergreen
.14	.24	.95	5.4	8.0	1.0	1.0	.80	22.0	1.5	.0	500	5 Deciduous Needle leaf
.20	.24	.95	6.2	7.0	1.0	.0	.80	22.0	1.5	0	500	6 Deciduous Broad leaf
.17	.24	.95	4.1	7.0	1.0	.0	.90	32.0	1.5	.0	500	7 Evergreen Broad leaf
.21	.43	.96	5.1	4.0	1.0	.0	.75	.3	.7	.7	100	8 Short grass
.24	.43	.96	5.1	5.0	1.0	.0	.80	1.2	1.0	.7	100	9 Tall grass
.20	.24	.95	5.1	1.0	.2	1.0	.20	.7	1.0	.0	500	10 Semi desert
.20	.24	.95	5.1	4.5	.5	1.0	.60	.2	1.0	.0	50	11 Tundra
.14	.24	.97	5.1	5.5	1.0	1.0	.70	1.0	1.0	0	500	12 Evergreen Shrub
.20	.28	.97	5.1	5.5	1.0	1.0	.70	1.0	1.0	.0	500	13 Deciduous shrub
.16	.24	.96	6.2	7.0	1.0	.5	.80	22.0	1.5	.0	500	14 Mixed woodland
.22	.40	.95	5.1	5.0	.5	.0	.85	1.0	1.0	.0	100	15 Crop/mixed

												farming
.18	.40	.95	5.1	5.0	.5	.0	.80	1.1	1.0	.0	500	16 Irrigated crop
.12	.43	.98	5.1	7.0	1.0	.0	.80	1.6	1.0	.0	500	17 Bog or marsh
.20	.36	.96	5.1	6.0	1.0	.0	.80	7.0	1.0	.0	100	18 Wooded grassland
.20	.36	.90	5.1	3.6	1.0	.0	.74	6.0	.8	.0	500	19 Urban and built up
.17	.24	.95	4.1	7.0	1.0	.0	.90	32.0	1.5	.0	500	20 Wetland evergreen broadleaf tree

References

Atlas, D., and Ulbrich, W., 2000: An observationally based conceptual model of warm oceanic convective rain in the tropics. *J. Appl. Meteor.*, **39**, 2165-2181.

Angeles, M. E., González, J. E., Ramírez−Beltrán, N. D., Tepley, C. A., and Comarazamy, D. E., 2010: Origins of the Caribbean rainfall bimodal behavior. *J. Geophys. Res.*, **115**, D11106, doi:10.1029/2009JD012990.

Baik, J., Kim, Y.H., and Chung, H.Y., 2000: Dry and moist convection forced by an urban heat island, *J. Appl. Meteor.*, **40**, 1462-1475.

Baumer, D., Rinke, R., and Vogel, B., 2007: Weekly periodicities of aerosol optical thickness over central Europe- evidence of an anthropogenic direct aerosol effect, *Atmos. Chem. & Phys.*, **7**, 11545-11560.

Blei, S., Ho, C.A., and Sommerfeld, M., 2002: A stochastic droplet collision model with consideration of impact efficiency, *ILASS Proc.*, Zaroga.

Bornstein, R., and LeRoy, M., 1990: Urban Barrier Effects on Convective and Frontal Thunderstorms, Fourth Conference. on Mesoscale. Processes, Boulder, CO, *Amer Meteor. Soc.*, 120–121.

Bomstein, R., Thunis, P., and Schayes, G., 1993: Simulation of urban barrier effects on polluted urban boundary layers using the three dimensional URBMETrrvM model with urban topography, *Air Poll., Elsevier Science*, 15- 34.

Bornstein, R., and Lin, Q., 2000: Urban heat islands and summertime convective thunderstorms in Atlanta: three case studies. *Atmos. Env.*, **34**, 507-516.

Borys, R. D. and D.L. Mitchell, 2000: The relationships among cloud microphysics, chemistry, and precipitation rate in cold mountain clouds. *Atmos. Env.*, **34**, 2593–2602.

Bowen, E., 1950. The Formation of Rain by Coalescence. *NASA Ast. Phys.*, 193-213.

Carrio, G. and Cotton, W., 2007: Urban land use and pollution impacts in mesoscale circulation over Houston, *13th Conf. on Meso. Proc.*, Session 11, Orographic coastal and other thermally driven mesoscale circulations.

Cheng, W., Carrio, G., Cotton, W., and Saleeby, S., 2009: Influence of cloud condensation and giant cloud condensation nuclei on the development of precipitating trade wind cumuli in a large eddy simulation, *J. Geophys. Res.*, **114**, D08201.

Cicek, I. and Turkoglu, N., 2005: Urban effects of precipitation in Ankara. *Atmos.*, **18**, 3,. 173-187.

Clark, T., 1983: Use of log-normal distributions for numerical calculations of condensation and collection, *J. Atmos. Sci.*, **33**, 810-821.

Cohard, J.M., Pinty, J.P., and Bedos, C., 1998: Extending Twomey's analytical estimate of nucleated cloud droplet concentrations from CCN spectra, *J. of Atmos. Sci*., **55**, 3348-3357.

Comarazamy, D., Gonzalez, J., Tepley, C.A., Raizada, S., and Pandya, V., 2006: The effects of atmospheric particle concentration on cloud microphysics over Arecibo, *J. Geophys. Res.*, **111**, D09205, doi:10.1029/JD006243.

Comarazamy D., and González, J., 2008: On the validation of early season precipitation on the island of Puerto Rico using a mesoscale atmospheric model., *J. Hydrometeor*, **9**, 507-520.

Cotton, W. R., Pielke Sr., R. A., Walko, R. L., Liston, G. E., Tremback, C. J., Jiang, H., McAnelly, R. L., Harrington, J. Y., Nicholls, M. E., Carrio, G. G., and McFadden, J. P., 2003. RAMS 2001: Current status and future directions. *Meteor. & Atmos. Phys.*, **82**, 5-29.

Diem, J. and Brown, D., 2003. Precipitation in Central Arizona, *Pro. Geo.*, **55**, 3, 343– 355.

Das, B., 2008: Quantitative analysis of aerosol effects on cloud radiative properties in urban polluted cities, *AIP Conf. Proc*. **1100**, pp. 372-375.

Dickinson, R. E., Sellers A. H., Kennedy P. J., and Wilson, M. F., 1986: Biosphere-Atmosphere Transfer Scheme (BATS) for the NCAR climate community model. *Tech. Note*, NCAR/TN-275+STR. 69 pp.

Dixon, P. G., and Mote, T. L., 2003: Patterns and causes of Atlanta's urban heat island-initiated precipitation. *J. Appl. Meteor.*, **42**, 1273-1284.

Doherty, O.M., Riemer, N., and Hameed S., 2008: Saharan mineral dust transport into the Caribbean: Observed atmospheric controls and trends, *J. Geophys. Res.*, **113**, D07211, doi:10.1029/2007JD009171.

Dubovik, O. and King, M., 2000: A flexible inversion algorithm for retrieval of aerosol optical properties from sun and sky radiance measurements, *J. Geophys. Res.*, **105**, 20673-20696.

Eck, T.F., Holben, B.N., Reid, J.S., Giles, D.M., Rivas, M.A., Singh, R.P., Tripathi, S.N., Bruegge, C.J., Platnick, S., Arnold, G.T., Krotkov, N.A., Cam, S. A., Sinyuk, A.,

Dubovik, O., Arola, A., Schafer, J.S., Artaxo, P., Smirnov, A., Chen, H., and P. Goloub, 2012: Fog and cloud-induced aerosol modification observed by the Aerosol Robotic Network (AERONET). *J. Geophys. Res*, **117**, D07206, doi:10.1029/2011JD016839

Fan, J., Leung, R., Li, Z., Morrison, H., Chen, H., Zhou, Y., Qian, Y., Y. Wang, 2012: Aerosolimpacts on clouds and precipitation in eastern China: Results from bin and bulk microphysics, *J. of Geophys. Res.*, **117**, D00K36, doi: 10.1029/2011JD016537

Feingold, G., Cotton, W., Davis, J.T., and Kreidenweis, S.M., 1999: The impact of giant cloud condensation nuclei on drizzle formation in stratocumulus: Implications for cloud radiative properties, *J. Atmos. Sci.*, **56**, 4100-4117.

Flatau, P.J., Tripoli, G.J., Verlinde, J., and W.R. Cotton, 1989: The CSU-RAMS cloudmicrophysical module: General theory and code documentation. Colorado State Univ., Dep. Atmos. Sci., Fort Collins, Colorado 80523. *Atmos. Sci. Pap.*, **451**, 88 pp.

Gavati, A. and Rosenfeld, D., 2004: Quantifying precipitation suppression due to air pollution, *J. Appl. Meteor.*, **43**, 1038-1056.

Grabowski, W., 1999: Cloud microphysics and the tropical climate: Cloud-resolving model perspective, *J. Clim.*, **13**, 2306-2322.

Grabowski, W., 2003: Impact of cloud microphysics on convective-radiative quasi equilibrium revealed cloud-resolving convection parameterization, *J. Clim.*, **16**, 3463-3475.

Grabowski, W., 2005: Indirect impact of atmospheric aerosols in idealized simulations of convective-radiative quasi equilibrium, *J. Clim.*, **19**, 4664-4682.

Gross, B., Chaw, S., Wu, Y., Garofolo, E., Moshary, F., and Ahmed, S., 2009: Using Mie Raman LIDAR measurements to explore cloud properties. *11th Conf. on Atmos. Chem.*, Session 9.

Holben, B. N., Eck, T.F., Slutsker, I., Smirnov, A., Sinyuk, A., Schafer, J., Giles, D., and O.Dubovik, 2006: AERONET's version 2.0 quality assurance criteria, remote sensing of atmosphere and clouds, *Proc. SPIE Int. Soc. Opt. Eng.*, 6408, 64080Q, doi:10.1117/12.706524.

Hu, Z., Bruintjes R.T., and Betterton, E.A., 1998: Sensitivity of cloud droplet growth to collision and coalescence efficiencies in a parcel model. *J. Atmos. Sci.*, **55**, 2502-2515.

Huang, J., Zhang, C., and Prospero, J.M., 2009: African aerosol and large-scale precipitation variability over West Africa, *Env. Res. Lett.*, **4**, 015006.

Huff, F.A., and Changnon, S.A.,1973: Precipitation modification by major urban areas, *Amer. Meteor. Soc.*, **54**, 1220 – 1232.

Jauregui, E., 1997: Heat island development in Mexico City. *Atmos. Env.*, **31**, 3821-3831.

Jauregui, E., and Romales, E., 1996: Urban effects of convective precipitation in Mexico City, *Atmos. Env.*, **30**, 3383-3389.

Jirak, I.L., and W.R. Cotton, 2006: Effects of air pollution along the front range of the Rocky Mountains. *J. Appl. Meteor. and Clim.*, **45**, 236-245.

Jury, M., 2009: An intercomparison of observational, reanalysis, satellite, and coupled model data on mean rainfall in the Caribbean, *J. Hydrometeor*, **10**, 413-430.

Kalnay, E., Kanamitsu, M., Kistler, R., Collins, W., Deaven, D., Gandin, L., Iredell, M., Saha,S., White, G., Woollen, J., Zhu, Y., Leetmaa, A., Reynolds, B., Chelliah, M., Ebisuzaki, W., Higgins, W., Janowiak, J., Mo, K.C., Ropelewski, C., Wang, J., Jenne, R., and D. Joseph, 1996: The NCEP/NCAR 40-Year Reanalysis Project. *Bull. Amer. Meteor. Soc.*, **77**, 437−471.

Kessler, E., 1994. On the continuity and distribution of water substance in atmospheric circulations, *Atmos. Res.*, **38**, 109-145.

Khain, A. Ovtchinnikov, M., Pinsky, M., Pokrovsky, A., and Krugliak, H., 2000: Notes on the state-of-the-art numerical modeling of cloud microphysics, *Atmos. Res.*, **55**, 159-224.

Khairoutdinov, M. and Kogan, Y., 1999: A new cloud parameterization in a large-eddy simulation model of marine stratocumulus, *Mon. Weath. Rev.*, **128**, 229-243.

Kirshen, P., Watson, C., Douglas, E., Gontz, A., Lee, J., and Tian, Y., 2007: Coastal flooding in the Northeastern United States due to climate change. Mitigation and adaptation strategies for global change, as part of the special issue entitled: "Northeast United States Climate Impact Assessment".

Kogan, Y., 1999: The simulation of a convective cloud in a 3D model with explicit microphysics part I: Model description and sensitivity experiments, *J. Atmos. Sci.*, **48**, 1160-1188.

Korelev, A. and Isaac, G., 1999: Drop growth due to high supersaturation caused by isobaric mixing, *J. Atmos. Sci.*, **57**, 1675-1685.

Lau, K. M., Kim, M. K., Sud, Y. C., and Walker, G. K., 2009: A GCM study of the response of the atmospheric water cycle of West Africa and the Atlantic to Saharan dust radiative forcing, *Ann. Geophys.*, **27**, 4023-4037, doi:10.5194/angeo-27-4023-2009

Lensky, I. and Rosenfeld, D., 1996: Estimation of precipitation area and rain intensity based on the microphysical properties retrieved from NOAA AVHRR data, *J. Appl. Meteor.*, **36**, 234-232.

Low, R., 1969: Generalized equation for the solution effect in droplet growth, *Notes Corres.*, 608-611.

Meyers, M. P., Walko, R. L., Harrington J. Y., and Cotton, W. R., 1997: New RAMS cloud microphysics parameterization. Part II: The two-moment scheme. Atmos. Res., **45**, 3-39.

Mischenko, M. Geogdzhayev, B., Cairns, B., Carlson, B.E., Chowdhary, J., Lacis, A.A., Lui, L., Rossow, W. B., and Travis, L.D., 2007: Past, present, and future of global aerosol climatologies derived from satellite observations: A perspective, J. Quant. Spectr. and Rad. Trans., **106**, 325– 347.

Morrison, H. and Grabowski, W., 2007: Modeling supersaturation and subgrid-scale mixing with two-moment bulk warm microphysics, J. Atmos. Sci., **65**, 792-811.

Nagel, D., Herber, A., Thomason, L.W., and U. Leiterer,1998: Vertical distribution of the spectral aerosol optical depth in the Arctic from 1993 to 1996. *J. Geophys. Res.*, **103**, 1857-1870.

Ntelekos, A., Smith, J.A., Donner, L., Fast, J.D., Gustavson, W., Chapman, E.G., and Krajewski, W.F., 2009: The effect of aerosols on convective precipitation in the Northeastern United States, *J. Royal Meteor. Soc.*, **135**, 1367-139.

Otero, L., Fochesatto, G.J., Ristori, P.R., Flamant, P.H., Piacentini, R.D., Holben, B., and Quel, E.J., 2003. Simple method to derive aerosol microphysical properties from AERONET multi-wavelength direct solar measurements, *Adv. Space Res.*, **34**, 10, 2232-2235.

Parry, M.L., Canziani, O. F., Palutikof, J. P., van der Linden, P. J., and Hanson, C. E., 2008: Contribution of working group II to the fourth assessment report of the Intergovernmental Panel on Climate Change, Cambridge University Press, Cambridge, UK.

Pielke, R. A., Cotton, W.R., Walko, R.L., Tremback, C.J., Lyons, W., Grasso, L.D., Nicholls, M.E., Moran, M.D., Wesley, D.A., and Lee, T.J., 1992: A comprehensive meteorological modeling system: RAMS, Meteor. Atmos. Phys., **49**, 69-91.

Przyborski, P and Ranson, J. (Accessed 4 Feb., 2009), "What are Aerosols?", NASA. http://earthobservatory.nasa.gov/Features/Aerosols/.

Ragovin, J. (Accessed 7 Nov., 2009), "Jeff's Weather Blog", http://www.jeffsweather.com.

Regional Atmospheric Modeling System, 1995: Technical description. Atmospheric, Meteorological, and Environmental Technologies. 50 pp.

Reid, J. S., Koppmann, R., Eck, T.F., and D. Eleuterio, 2005: A review of biomass burning emissions Part II: Intensive physical properties of biomass burning particles. *Atmos.Chem. Phys.*, **5**, 799–825.

Riley, M., 2007: Assessing the impact of interannual climate variability on New York City's reservoir system, Cornell University Graduate School for Atmospheric Science.

Rosenfeld, D., 2008: How do aerosols affect precipitation?, *Sci.*, **321**, 1309-1315.

Rosenfeld, D. and Woodley, W., 1993: Effects of Cloud Seeding in West Texas. *J. Appl. Meteor.*, **32**, 1848-1866.

Rotstayn, L . and Lohmann, U., 2002: Tropical rainfall trends and the indirect aerosol effect, *J. Clim.*, **15**, 2103-2116.

Saleeby, M. S., and Cotton, W. R., 2004: A large-droplet mode and prognostic number concentration of cloud droplets in the Colorado State University Regional Atmospheric Modeling System (RAMS) part I: Module descriptions and supercell test simulations. *J. Appl. Meteor.*, **43**, 182-195.

Shen, C., Wang, W.C., Hao, Z., and Gong W., 2007: Exceptional drought events over eastern China during the last five centuries. *Climatic Change*, **85**, 453-471.

Shepherd, H. Peirce, and Negri, A., 2002: Rainfall modification by major urban areas: observations from space bourne rain radar on the TRMM satellite, J. Appl. Meteor., **41**, 689–701.

Shepherd, J. M., and Burian, S. J., 2003: Detection of urban-induced rainfall anomalies in a major coastal city. *Earth Int.*, **7**, 1-17.

Shepherd, J. M., 2005: A review of current investigations of urban-induced rainfall and recommendations for the future. *Earth Int.*, **9**, 1-27.

Shepherd, J., 2006: Evidence of urban induced precipitation variability in arid climate regimes, *J. Ar. Env.*, **67**, 607-628.

Smith, S.E., (Accessed 4Oct. 2009), "What is LIDAR?" Conjecture Corporation http://www.wisegeek.com/what-is-lidar.htm

Solomon, S., D. Qin, M. Manning, Z. Chen, M. Marquis, K.B. Averyt, M.Tignor and H.L. Miller 2007: Intergovernmental Panel on Climate Change, Summary for policymakers. Climate Change - The Physical Science Basis. Contribution of Working Group I to the Fourth Assessment Report of the Intergovernmental Panel on Climate Change, Cambridge University Press, Cambridge, United Kingdom and New York, NY, USA.

Stallins, J. Bentley, M., and Rose, L., 2006: Cloud-to-ground flash patterns for Atlanta, Georgia (USA) from 1992 to 2003. *Clim. Res.*, **30**, 99-112.

Stegmann, P., 2004: Characterization of aerosols over the North Atlantic Ocean from SeaWiFS, *Deep Sea Res. II*, **51**, 913-925.

Stein, U., and Alpert, P., 1993: Factor separation in numerical simulations, *J. Atmos. Sci.*, **50**, 2107-2115.

Takeda, T., 1971: Numerical simulation of a precipitating convective cloud: The formation of a "long-lasting" cloud, *J. Atmos. Sci.*, **328**, 350-376.

Tripoli, G.J. and Cotton, W., 1982: The Colorado State University three-dimensional cloud/mesoscale model – 1982. Part I: general theoretical framework and sensitivity experiments, *J. de Rech. Atmos.*, **16**, 185-220.

van den Heever, S. and Cotton, W., 2007: Urban aerosol impacts on downwind convective storms, J. of Appl. Meteor. and Clim., **46**, 828-850.

van den Heever, S., Carrio, G., Cotton, W.R., Demott, P.J., and Prenni, A.J., 2006: Impacts of nucleating aerosol on Florida storms. Part I: Mesoscale simulations, *J. Atmos. Sci.*, **63**, 1752-1775.

Verlinde, J., Flatau, P.J., and Cotton, W.R., 1990: Analytical solutions to the collection growth equation: Comparison with approximate methods and application to cloud microphysics parameterization schemes, J. Atmos. Sci., **47**, 2871-2880.

Walko, R.L., Cotton, W.R., Meyers, M.P., and J.Y. Harrington, 1995: New RAMS cloud microphysics parameterization. Part I: The single-moment scheme. *J. Atmos. Res.*, **38**, 29-62.

Wang, L.P., Xue, Y., Oyala, O., and Grabowski, W., 2006: Effects of stochastic coalescence and air turbulence on the size distribution of cloud droplets, *Atmos. Res.*, **82**, 416-432.

Wang, S., Wang, Q., and Feingold, G., 2002: Turbulence, condensation, and liquid water transport in numerically simulated non-precipitating stratocumulus clouds, J. Atmos. Sci., **60**, 262-278.

Williams, M., 1995: Growth rates of liquid drops for large saturation ratios, *J. Aero. Sci.*, **26**, 477-487.

Wyllie, M.E., 2008: The August 8, 2007 Floods in New York City. IMPACTS: Weather 2007 Annual Meeting of *Amer. Meteor. Soc.*,- January 2008.

Yau, M.K., 1980: A two-cylinder model of cumulus cells and its application in computing cumulus transports. *J. Atmos. Sci.*, **37**, 2470-2485.

Yau, M.K. & Rogers, R.R., 1989: A short course in cloud physics, *Butterworth-Heinemann, United Kingdom*, 3rd edition.